Doctoral Dissertation

Effects of the Reaction Field on the Electrochemical CO_2 Reduction Catalyzed by Metal Porphyrin Complexes

Kento Kosugi

January 2022

Division of Applied Chemistry

Graduate School of Engineering

Osaka University

General Introduction

Background and challenges for CO_2 reduction

Currently, our society consumes fossil resources as chemical raw materials and energy sources and emits CO_2 into the atmosphere. As a result, we encounter serious problems such as energy shortage and global warming. As a solution to these problems, technology to efficiently convert carbon dioxide (CO_2) into chemical resources has attracted considerable attention in recent years because the technology can produce chemical resources in clean manner and reduce the amount of CO_2 emitted into the atmosphere.[1] If the technology to efficiently convert CO_2 into resources is established, it can potentially lead to the construction of the ideal carbon recycle system that uses CO_2 as a carbon source to produce energy and chemical raw materials (Scheme 1).

In this context, electrochemical CO_2 reduction is a fascinating reaction because the reaction can convert CO_2 into energy-rich and useful chemicals. As shown in Scheme 2, CO_2 can be reduced to various kind of chemical fuels such as carbon monoxide (CO), formic acid (HCOOH), formaldehyde, methanol, and methane by electrochemical reduction.[2-4] Among them, CO is greatly useful carbon source because it is utilized in the synthesis of saturated hydrocarbons by the Fischer-Tropsch process.[5-7] Therefore, the development of the catalytic system that can convert CO_2 into CO is an important research target.

However, there are two problems with electrochemical CO_2 reduction. The first problem is that CO_2 is chemically stable. One electron reduction of CO_2 to form $CO_2^{\cdot -}$ radical anion requires largely negative potential (Scheme 2, Eq. (1)). In this regard, the reactions involving multiproton coupled electron transfers to CO_2 (Scheme 2, Eq. (2) ~ (6)) are attractive because the standard redox potentials for these reactions are only about −0.3 V ~ −0.5 V vs. NHE at pH = 7.0 (Scheme 2).[2,3] However, the electrochemical reduction of CO_2 using metal electrodes is much more difficult than expected from the standard redox potential[4], and thus the development of catalysts that facilitates CO_2 reduction is strongly demanded. Another problem is the existence of the competing hydrogen evolution reaction. As the hydrogen evolution reaction is more thermodynamically favorable (the standard redox potential of the hydrogen evolution reaction is −0.41 V vs. NHE, Scheme 2, Eq. (7)), hydrogen evolution can proceed

simultaneously when a sufficient potential is applied for the CO_2 reduction system.[4] Therefore, the catalyst for CO_2 reduction should have higher selectivity for the targeted reaction rather than the competing hydrogen evolution reaction.

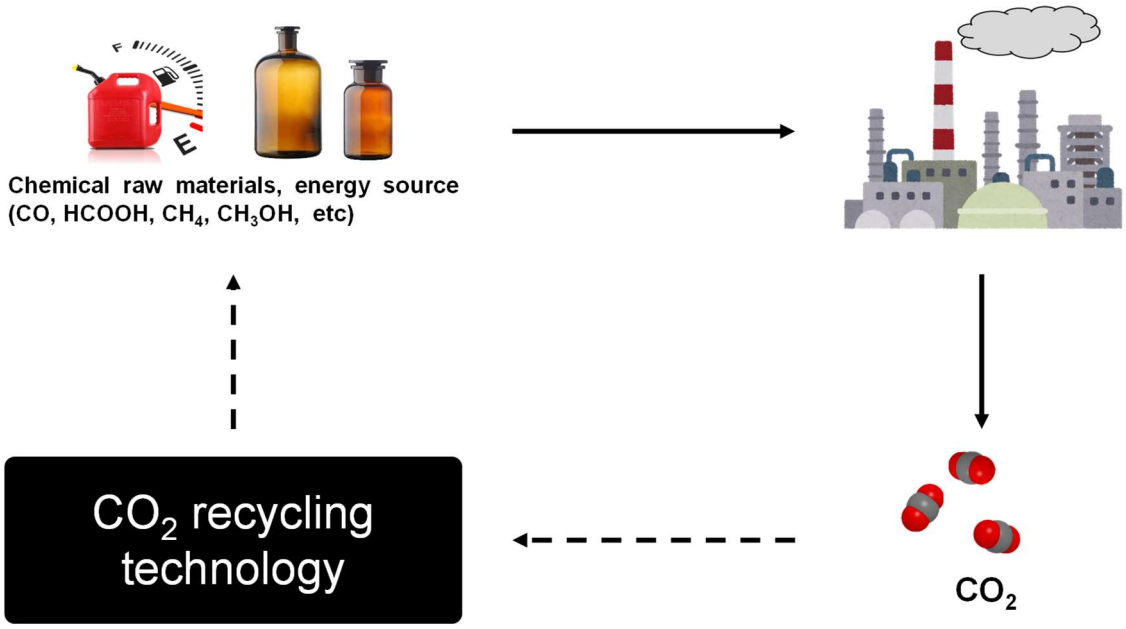

Scheme 1. Conceptual diagram of the carbon recycle system.

			(vs. NHE)	
$CO_2 + e^-$	⟶	$CO_2^{\cdot -}$	$E^0 = -1.90$ V	(1)
$CO_2 + 2\,H^+ + 2\,e^-$	⟶	$CO + H_2O$	$E^0 = -0.53$ V	(2)
$CO_2 + 2\,H^+ + 2\,e^-$	⟶	$HCOOH$	$E^0 = -0.61$ V	(3)
$CO_2 + 4\,H^+ + 4\,e^-$	⟶	$HCHO + H_2O$	$E^0 = -0.48$ V	(4)
$CO_2 + 6\,H^+ + 6\,e^-$	⟶	$CH_3OH + H_2O$	$E^0 = -0.38$ V	(5)
$CO_2 + 8\,H^+ + 8\,e^-$	⟶	$CH_4 + 2\,H_2O$	$E^0 = -0.24$ V	(6)
$2\,H^+ + 2\,e^-$	⟶	H_2	$E^0 = -0.41$ V	(7)

Scheme 2. Standard redox potentials for CO_2 reduction and H_2 evolution reaction in pH 7 in aqueous solution (vs. NHE).

Catalytic system for small molecule conversion in nature

There exist several catalysts that promote small molecule conversion in nature. Figures 1 and 2 illustrate the structures of representative examples of such catalysts.

First example is oxygen evolving complex (OEC, Figure 1) embedded in photosystem II, which catalyzes water oxidation reaction ($2H_2O \rightarrow O_2 + 4H^+ + 4e^-$).[8,9] X-ray crystallographic and spectroscopic studies revealed that OEC has a cubane-like Mn_4CaO_4 cluster (Figure 1).[10,11] In other words, the active center for water oxidation reaction consists of a *metal complex*. In addition, Mn_4CaO_4 cluster is surrounded by water and amino acid residues. They contribute to maintain the structure of Mn_4CaO_4 cluster. Furthermore, the electrons extracted by the water oxidation reaction are transferred to P680 via D1-Tyr 161 (Yz) and the protons are transferred to D1-His 190 (Figure 3a–3c) [10-12], and these transfer of electrons and protons play critical roles for achieving efficient catalysis. This fact clearly demonstrates the environment in the vicinity of active center (*reaction field*) plays important roles in water oxidation reaction.

Second example is carbon monoxide dehydrogenase (CODH, Figure 2), which is a biological system for CO_2 redox catalysis. CODH catalyzes the reversible interconversion of CO_2 and CO ($CO + H_2O \rightleftarrows CO_2 + 2H^+ + 2e^-$).[13,14] The active center of CODH is $NiFe_4S_4$ cluster (cluster C), where the nickel center, four iron atoms, and four sulfur atoms are assembled into a distorted cubane structure (Figure 2a and 2b).[13] In CODH, amino acid residues are precisely positioned around the $NiFe_4S_4$ cluster, which contribute to stabilize a CO_2 adduct intermediate and assist in C-O bond cleavage (Figure 4a and 4b).[14] Similar to OEC, the active center of CODH consists of *metal complex*, and the *reaction field* constructed by amino acid residues plays important roles in efficient catalysis.

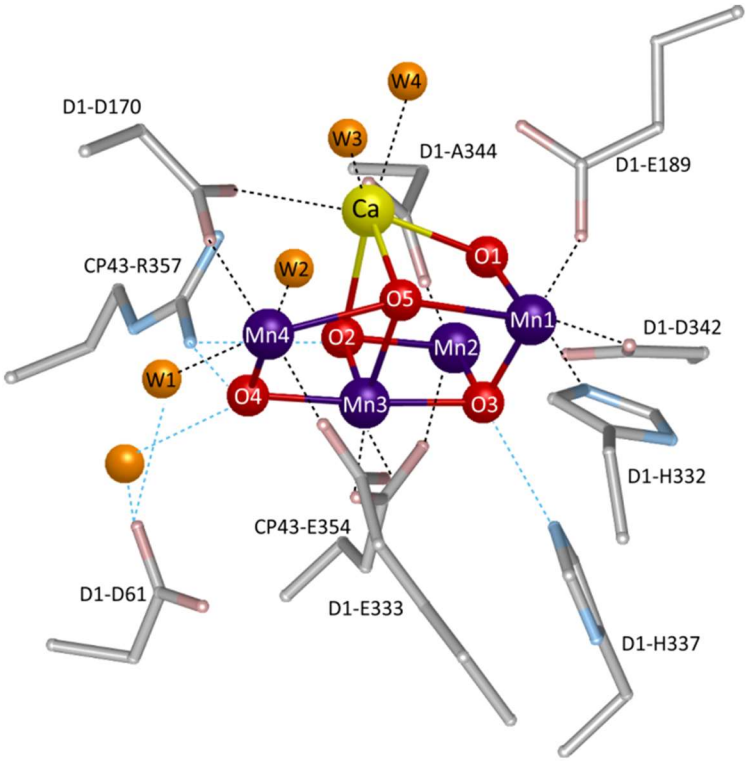

Figure 1. The structure of the Mn_4CaO_4 cluster and its ligand environment in the OEC. Mn = purple, Ca = yellow, O = red, oxygen atoms in water molecules = orange.

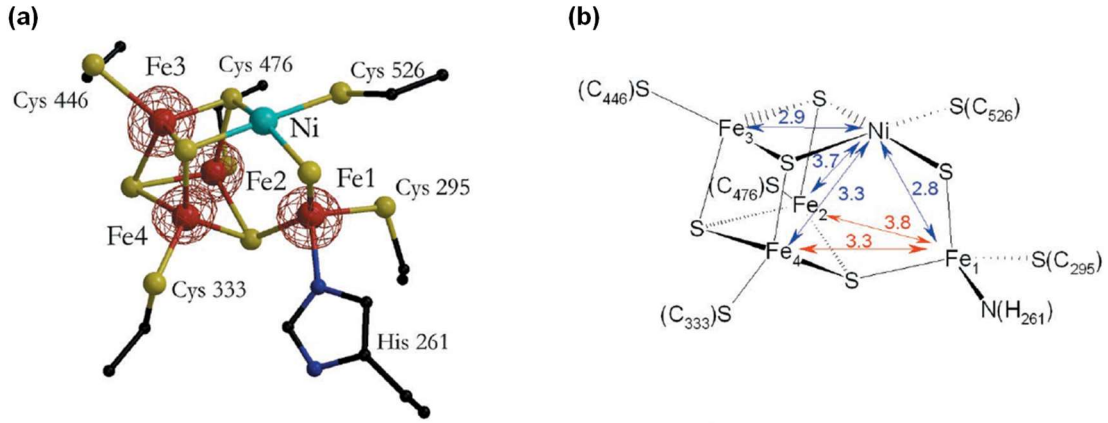

Figure 2. (a) The structure of the $NiFe_4S_4$ cluster and its ligand environment in the CODH. Fe = red, Ni = light blue, S = yellow. Copyright 2001 American Association for the Advancement of Science. (b) Schematic representation of $NiFe_4S_4$ cluster and its ligand environment in the CODH. Copyright 2001 American Association for the Advancement of Science.

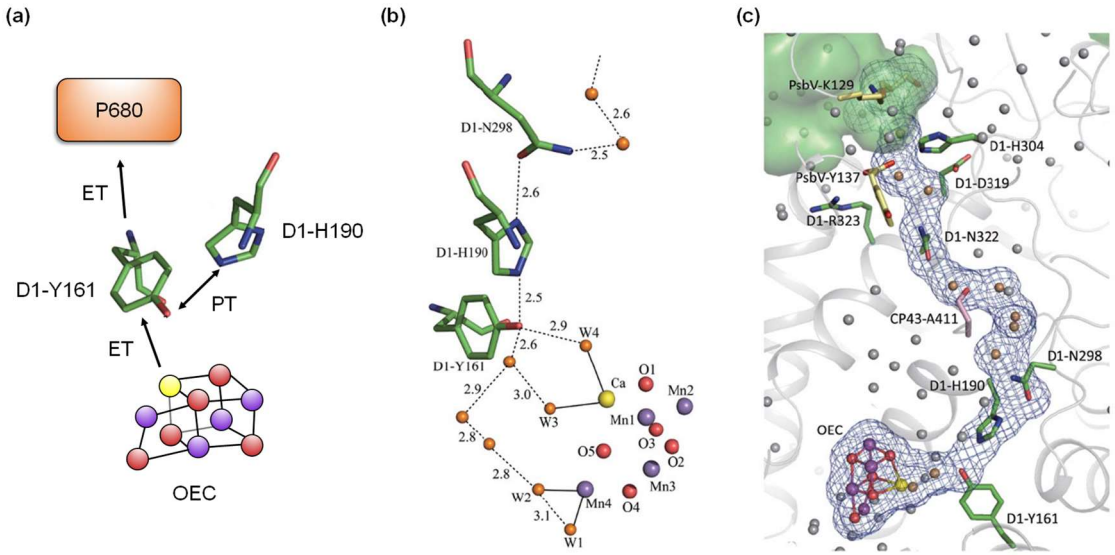

Figure 3. (a) A diagram of charge and proton transfer reactions in photosystem II. (b) Hydrogen bonds around Y_Z (D1-Tyr 161). The bonds between metal atoms and water ligands are depicted as solid lines, and the hydrogen bonds are depicted as dashed lines. Distances are expressed in angstroms. Copyright 2011 Springer Nature. (c) Hydrogen-bond network from the Mn_4CaO_5 cluster through Yz to the lumenal bulk phase. Water molecules participating in the hydrogen-bond network are depicted in orange, whereas those not participating are depicted in grey. The area in green in the upper left corner represents the lumenal bulk surface. Copyright 2011 Springer Nature.

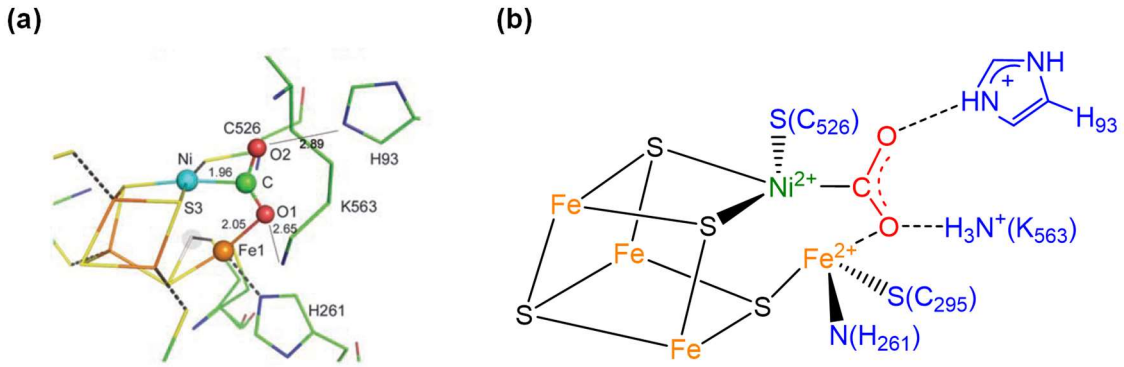

Figure 4. (a) The structure of CO_2 adduct of $NiFe_4S_4$ cluster and its ligand environment in the CODH. Fe = orange, Ni = light blue, C = green, O = red, S = yellow. Copyright 2007 American Association for the Advancement of Science. (b) Schematic representation of CO_2 adduct of $NiFe_4S_4$ cluster and its ligand environment in the CODH.

Approaches to develop artificial catalytic system for CO_2 reduction

As shown in the previous section, both OEC and CODH, which are catalytic systems for small molecule conversion in nature, satisfy the following two factors; (i) bearing a metal complex as the active center, and (ii) bearing active centers surrounded by precisely positioned water molecules and/or amino acid residues, which contribute for the creation of the reaction field. Inspired by these natural catalytic systems, I anticipated that these two factors, the used of a metal complex as a catalytic center and the creation of reaction field, should be important to construct efficient artificial catalysts for CO_2 reduction. In particular, I focus on the effect of the reaction field on the metal-complex-based molecular catalyst in this Ph.D. thesis. In the following, I describe my strategy to develop the efficient artificial catalytic system for CO_2 reduction.

Iron porphyrin complexes for electrochemical CO_2 reduction

To date, extensive efforts have been made to develop efficient metal-complex-based molecular catalysts for electrochemical CO_2 reduction.[2-4,15-37] Among them, iron porphyrin complexes have played crucial roles in the history of the development of catalysts for electrochemical CO_2 reduction. The advantages of iron porphyrin complexes are (i) high activity, (ii) high selectivity for CO_2 reduction, and (iii) robustness during catalysis (Scheme 3).[15-25,] The electrochemical CO_2 reduction by iron porphyrin complexes ($CO_2 + 2e^- + 2H^+ \rightarrow CO + H_2O$) was first discovered by Savéant *et al*. in 1988.[24] This work revealed that the multielectron transfer ability of iron porphyrin complexes is highly advantageous for electrochemical CO_2 reduction reactions. In 1994, Savéant *et al*. also demonstrated that the addition of trifluoroethanol as a proton source largely enhanced the electrochemical CO_2 reduction activity by iron porphyrin complexes.[25] This strategy is now being applied not only to iron porphyrin complexes but also to various metal-complex-based molecular catalysts for CO_2 reduction.[2,3] In addition, the structure, electronic state, and physical properties of porphyrins can be easily tuned by introducing various substituents at the meso positions (Scheme 3).[3,16-22] Therefore, iron porphyrin complexes are one of the best scaffolds to develop efficient metal-complex-based molecular catalysts for electrochemical CO_2 reduction.

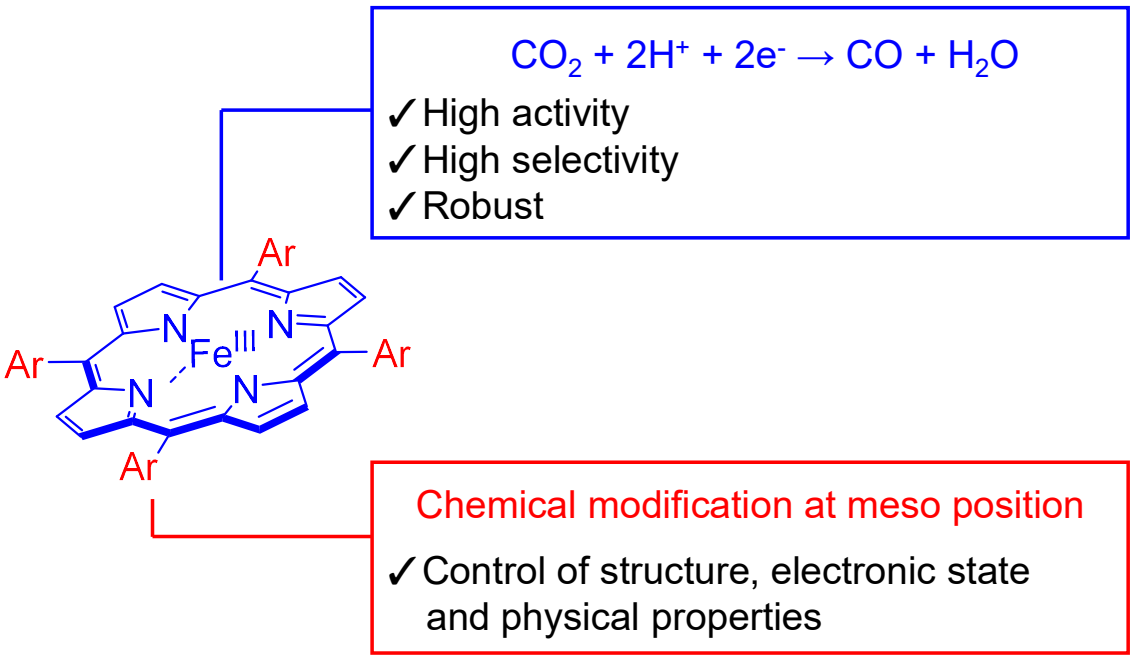

Scheme 3. Features of iron porphyrin complexes for electrochemical CO_2 reduction.

Modification of the secondary coordination sphere

Chemical modification of the secondary coordination sphere is one of the most powerful strategies to control the reaction field. Actually, in recent years, highly active CO_2 reduction catalysts based on iron porphyrin complexes have been achieved by controlling the environment in the vicinity of active center, iron ion.[16-19,21,22] In the following, I describe the representative examples of this class of compounds.

A major breakthrough in the development of CO_2 reduction catalysts based on the modification of the secondary coordination sphere was reported in 2012 by Savéant *et al*. They introduced local proton sources at the meso position of iron porphyrin complex, **Fe1** (Figure 5).[16,21] The local proton source introduced into the complex contributes to assist proton transfer in the CO_2 reduction reaction and stabilizes the CO_2 adduct through hydrogen bonding. The turnover frequency (TOF) of the complex was determined to be 6.3×10^3 s^{-1} at an overpotential of 0.56 V by cyclic voltammetry measurements, and this value of the TOF was the highest in the world at that time.

Fe2 is the iron porphyrin complex bearing positive charges (trimethylammonio groups) at the secondary coordination sphere (Figure 5).[18] The TOF value of **Fe2** was 1.0×10^6 s^{-1} at an overpotential of 0.22 V. Although the detailed mechanism has not been investigated, the positive charge in the secondary coordination sphere is considered to significantly stabilize the CO_2 adduct formed during the catalysis, leading to the decrease in overpotential and the enhancement of catalytic activity.

Fe3 is the iron porphyrin complex bearing amide at the secondary coordination sphere, which mimics the environment in CODH (Figure 5).[17] In the electrochemical CO_2 reduction, **Fe3** exhibited a very high TOF value, 5.5×10^6 s^{-1}.

These examples demonstrate that the modification of the secondary coordination sphere is a very useful strategy for improving the catalytic activity of iron porphyrin complexes.

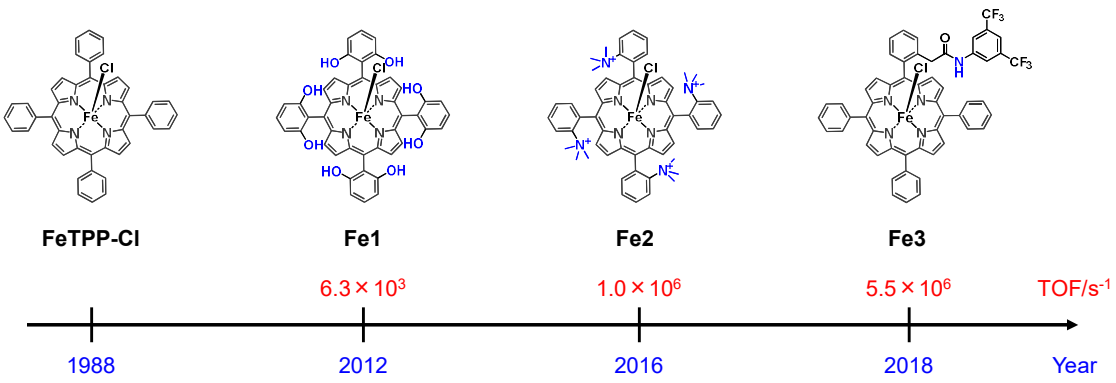

Figure 5. Chemical structures and turnover frequencies of iron porphyrin complexes.

Solvent effect

Solvent is one of the most important reaction fields that influences the selectivity and reactivity in solution.[40] In particular, solvation effect is prominent when charged intermediates are produced during the reaction. Menshutkin reaction ($NH_3 + CH_3Cl \rightarrow NH_3CH_3^+ + Cl^-$) is one of the representative reactions that is known to exhibit significantly enhanced rates in polar solvents due to strong electrostatic stabilization of the products. As shown in Figure 6, the activation barriers and the stability of the products largely depend on the solvent.[41] In the electrochemical CO_2 reduction, a negatively charged intermediate is produced, which should be influenced by the electrostatic field produced by solvent (Figure 7).[2,3]

Solubility of CO_2 depends on the solvent, which affects the CO_2 reduction ability. The solubility of CO_2 in various solvents at 298 K is summarized in Table 1.[25,42] CO_2 has higher solubility in organic solvents (0.136 – 0.282 M) than in aqueous medium (0.040 M).

In the electrochemistry, the dielectronic constants of the solvent is also an important factor that affects the reactivity. Based on the Coulomb's law, the dissociation of electrolyte is facilitated in the solvent with large dielectronic constant, which leads large electroconductivity. On the other hand, in the solvent with low dielectronic constant, the electroconductivity is low.

As described above, the effect of solvent is essential in chemical reactions in solution. However, there has been no example that investigates the effect of the solvent on the electrochemical CO_2 reduction reaction in detail.

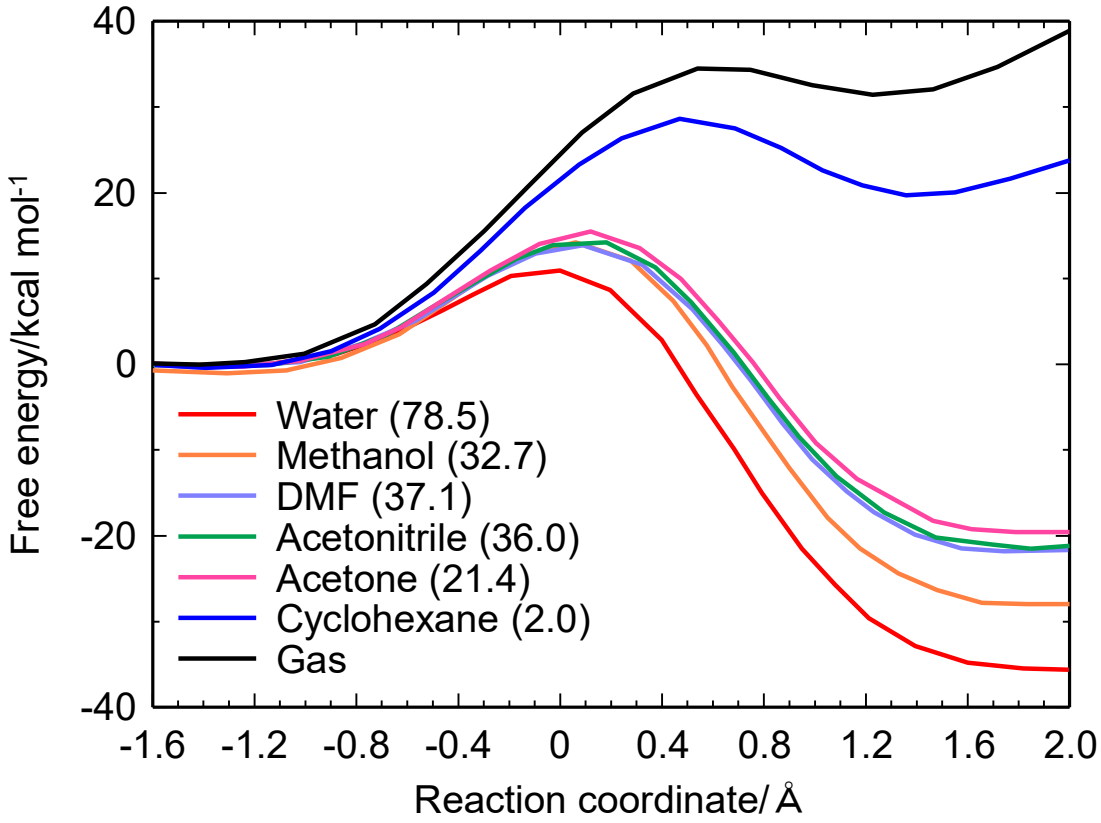

Figure 6. Free energy profile of the Menshutkin reaction ($NH_3 + CH_3Cl \rightarrow NH_3CH_3^+ + Cl^-$) in various solvents calculated with the mean-field QM/MM method. All the solvents are described with the polarizable charge response kernel model. The QM calculation is performed at the BHHLYP/6-31+G(*d*,*p*) level. The dielectric constants are shown in parentheses. Reaction coordinate is defined as $\xi = r(\mathrm{Cl} - \mathrm{C}) - r(\mathrm{N} - \mathrm{C})$. The results of mean-field QM/MM calculations are taken from ref. 41.

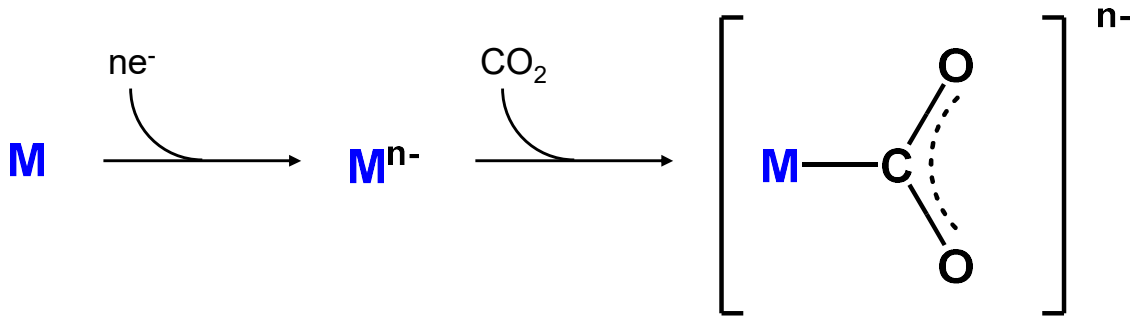

Figure 7. Reaction intermediates in electrochemical CO_2 reduction. M represents the metal center.

Table 1. Solubility of CO_2 in the various solvents.

Solvent	Solubility/mol L^{-1}	Reference
H_2O	0.040	25
1,4-Dioxane	0.255 ± 0.010	42
THF[a]	0.210 ± 0.010	42
MeCN[b]	0.282 ± 0.008	42
DMF[c]	0.196 ± 0.010	42
DMSO[d]	0.136 ± 0.006	42

[a] THF = tetrahydrofuran [b] MeCN = acetonitrile [c] DMF = *N*, *N*-dimethylformamide [d] DMSO = dimethyl sulfoxide

Aim and survey of this thesis

In this Ph.D. thesis, I aimed to develop highly active electrochemical CO_2 reduction systems catalyzed by metal porphyrin complexes based on a control of the reaction field. I focused on the effect of the reaction field on the catalytic activity, and the reaction field was controlled by a modification of the secondary coordination sphere and reaction medium (solvent). In particular, this thesis provides the first example that investigate effects of the reaction medium on the electrochemical CO_2 reduction activity in detail.

In chapter 1, I focused on a modification of the secondary coordination sphere to control the reaction field of the iron porphyrin complex (Figure 8a). An iron porphyrin complex bearing a hydroquinone moiety at the meso position was newly designed and synthesized. Electrochemical analysis revealed that it catalyzes CO_2 reduction at a lower overpotential compared with an iron complex without a hydroquinone moiety. Experimental and theoretical investigations suggested that a hydroquinone moiety at the meso position stabilizes the coordination bond between the metal center and CO_2 via a hydrogen bonding interaction with the latter in the secondary coordination sphere.

In chapter 2, I investigated effects of the reaction medium on the electrochemical CO_2 reduction activity catalyzed by an iron porphyrin complex (Figure 8b). A one-step counter anion exchange reaction increased the solubility of a commercially available catalyst, iron(III) tetraphenylporphyrin chloride, in a variety of solvents, allowing the investigation of its catalytic performance under various conditions. Surprisingly, the turnover frequency for CO evolution in MeCN reached 7,300,000 s^{-1}, which is the highest among those of current best-in-class molecular catalysts. It was also revealed that this excellent catalytic activity originates from the unique reaction between the generated Fe(I) species and CO_2 in MeCN during catalysis.

In chapter 3, I developed a highly active copper-based catalyst for electrochemical CO_2 reduction (Figure 8c). Based on the knowledge obtained in the former chapters, I chose a copper porphyrin complex bearing strong electron withdrawing substituents as a catalyst. Electrochemical analysis revealed that the TOF of the catalyst for CO_2 to CO conversion was 1,460,000 s^{-1} at an overpotential of 0.85 V. Surprisingly, this value is more than 1,000,000 times higher than those of the other reported copper-based molecular catalysts (TOF $\leq$ 1.15 s^{-1}).[37]

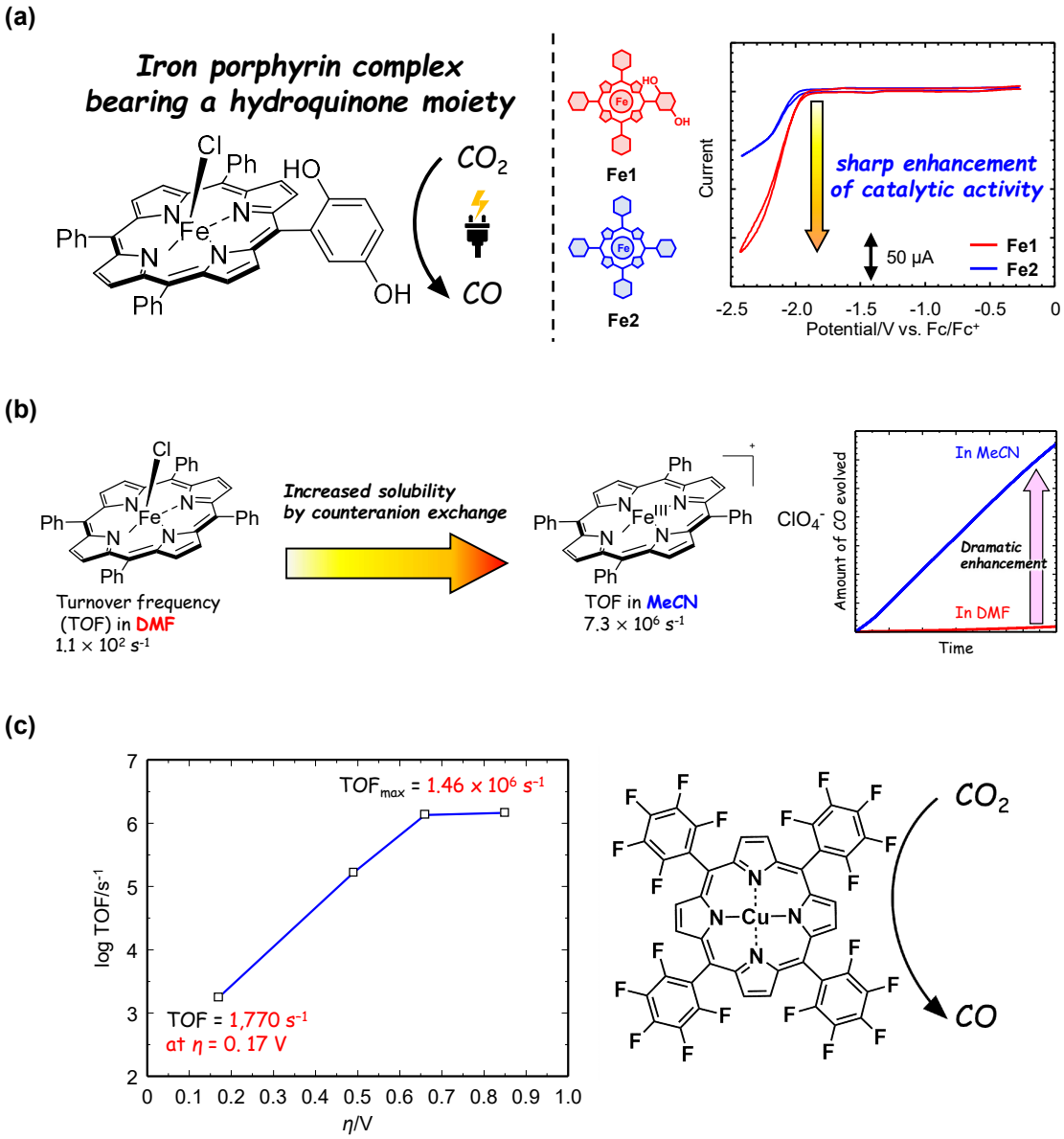

Figure 8. The schematic illustration of achievements in (a) chapter 1, (b) chapter 2, and (c) chapter 3.

References

[1] A. M. Appel, J. E. Bercaw, A. B. Bocarsly, H. Dobbek, D. L. DuBois, M. Dupuis, J. G. Ferry, E. Fujita, R. Hille, P. J. A. Kenis, C. A. Kerfeld, R. H. Morris, C. H. F. Peden, A. R. Portis, S. W. Ragsdale, T. B. Rauchfuss, J. N. H. Reek, L. C. Seefeldt, R. K. Thauer, G. L. Waldrop, *Chem*. *Rev*. **2013**, *113*, 6621.

[2] R. Francke, B. Schille, M. Roemelt, *Chem*. *Rev*. **2018**, *118*, 4631.

[3] E. Boutin, L. Merakeb, B. Ma, B. Boudy, M. Wang, J. Bonin, E. Anxolabéhère-Mallart, M. Robert, *Chem*. *Soc*. *Rev*. **2020**, *49*, 5772.

[4] Y. Hori, H. Wakebe, T. Tsukamoto, O. Koga, *Electrochim. Acta* **1994**, *39*, 1833.

[5] H. Shulz, *Appl. Catal. A-Gen*. **1999**, *186*, 3.

[6] A. Y. Khodakov, W. Chu, P. Fongarland, *Chem. Rev*. **2007**, *107*, 1692.

[7] E. van Steen, M. Claeys, *Chem. Eng. Technol*. **2008**, *31*, 655.

[8] K. N. Ferreira, T. M. Iverson, K. Maghlaoui, J. Barber, S. Iwata, *Science* **2004**, *303*, 1831.

[9] T. J. Meyer, M. H. V. Huynh, H. H. Throp, *Angew. Chem. Int. Ed*. **2007**, *46*, 5284.

[10] Y. Umena, K. Kawakami, J. Shen, N. Kamiya, *Nature* **2011**, *473*, 55.

[11] M. Saga, F. Akita, G. Ueno, H. Murasugi, Y. Nakajima, T. Shimazu, K. Yamashita, M. Yamamoto, H. Ago, J. Shen, *Nature* **2015**, *517*, 99.

[12] S. Y. Reece, D. G. Nocera, *Annu. Rev. Biochem*. **2009**, *78*, 673.

[13] H. Dobbek, V. Svetlitchnyl, L. Gremer, R. Huber, O. Meyer, *Science* **2001**, *293*, 1281.

[14] J. Jeoung, H. Dobbek, *Science* **2007**, *318*, 1461.

[15] C. Costentin, S. Drouet, G. Passard, M. Robert, J. M. Savéant, *J. Am*. *Chem*. *Soc*. **2013**, *135*, 9023.

[16] C. Costentin, G. Passard, M. Robert, J. M. Savéant, *J. Am. Chem. Soc*. **2014**, *136*, 11821.

[17] E. M. Nichols, J. S. Derrick, S. K. Nistanaki, P. T. Smith, C. J. Chang, *Chem. Sci*. **2018**, *9*, 2952.

[18] I. Azcarate, C. Costentin, M. Robert, J. M. Savéant, *J. Am. Chem. Soc*. **2016**, *138*, 16639.

[19] E. A. Mohamed, Z. N. Zahran, Y. Naruta, *Chem. Commun*. **2015**, *51*, 16900.

[20] Y. Okabe, S. K. Lee, M. Kondo, S. Masaoka, *J. Biol. Inorg. Chem*. **2017**, *22*, 713.

[21] C. Costentin, G. Passard, M. Robert, J. M. Savéant, *Proc. Natl. Acad. Sci. U. S. A*. **2014**, *111*, 14990.

[22] S. Sinha, J. J. Warren, *Inorg. Chem*. **2018**, *57*, 12650.

[23] K. Kosugi, M. Kondo, S. Masaoka, *Angew. Chem. Int. Ed*. **2021**, *60*, 22070.

[24] M. Hammouche, D. Lexa, J. M. Savéant, M. Momenteau, *J. Electronal. Chem. Interfacial Electrochem*. **1988**, *249*, 347.

[25] I. Bhugunm D. Lexa, J. M. Savéant, *J. Am. Chem. Soc*. **1994**, *116*, 5015.

[26] W. Nie, D. E. Tarnopol, C. C. L. McCrory, *J. Am. Chem. Soc*. **2021**, *143*, 3764.

[27] C. Cometto, L. Chen, P. K. Lo, Z. Guo, K. C. Lau, E. Anxolabéhère-Mallart, C. Fave, T. C. Lau, M. Robert, *ACS Catal*. **2018**, *8*, 3411.

[28] J. S. Derrick, M. Loipersberger, R. Chatterjee, D. A. Iovan, P. T. Smith, K. Chakarawet, J. Yano, J. R. Long, M. Head-Gordon, C. J. Chang, *J. Am. Chem. Soc*. **2020**, *142*, 20489.

[29] M. D. Sampson, C. P. Kubiak, *J. Am. Chem. Soc*. **2016**, *138*, 1386.

[30] L. M. Cao, H. H. Huang, J. W. Wang, D. C. Zhong, T. B. Lu, *Green Chem*. **2018**, *20*, 798.

[31] S. K. Lee, M. Kondo, G. Nakamura, M. Okamura, S. Masaoka, *Chem. Commun*. **2018**, *54*, 6915.

[32] K. Y. Wong, W. H. Chung, C. P. Lau, *J. Electroanal. Chem*. **1998**, *453*, 161.

[33] D. S. Laitar, P. Müller, J. P. Sadighi, *J. Am. Chem. Soc*. **2005**, *127*, 17196.

[34] R. J. Haines, R. E. Wittrig, C. P. Kubiak, *Inorg. Chem*. **1994**, *33*, 4723.

[35] R. Angamuthu, P. Byers, M. Lutz, A. L. Spek, E. Bouwman, *Science* **2010**, *327*, 313.

[36] Y. Zhou, Y. Xiao, J. Zhao, *New J. Chem*. **2020**, *44*, 16062.

[37] Z. Guo, F. Yu, Y. Yang, C. F. Leung, S. M. Ng, C. C. Ko, C. Cometto, T. C. Lau, M. Robert, *ChemSusChem* **2017**, *10*, 4009.

[38] W. J. Liu, H. H. Huang, T. Ouyang, L. Jiang, D. C. Zhong, W. Zhang, T. B. Lu, *Chem. Eur. J*. **2018**, *24*, 4503.

[39] X. Chai, H. H. Huang, H. Liu, Z. Ke, W. W. Yong, M. T. Zhang, Y. S. Cheng, X. W. Wei, L. Zhang, G. Yuan, *Chem. Commun*. **2020**, *56*, 3851.

[40] C. Reichardt, *Solvents and Solvent Effects in Organic Chemistry, 3rd ed*. Wiley-

VCH, Weinheim, Germany, 2003.

[41] H. Nakano, T. Yamamoto, *J. Chem. Phys*. **2012**, *136*, 134107.

[42] A. Gennaro, A. A. Isse, E. Vianello, *J. Electroanal. Chem*. **1990**, *289*, 203.

Chapter 1

Synthesis and Electrocatalytic CO_2 Reduction Activity of an Iron Porphyrin Complex Bearing a Hydroquinone Moiety

Introduction

The development of catalysts for CO_2 reduction is of great significance for constructing a sustainable energy cycle.[1] To date, there are numerous reports on metal-complex-based catalysts for CO_2 reduction.[2-16] Iron porphyrin complexes are an attractive class of catalysts for the reduction of CO_2 to CO that exhibit high activity, selectivity, and robustness.[3-9] Another important feature of these complexes is that their molecular structure can easily be modified by introducing substituent(s) at the meso position(s). Such chemical modification allows (i) fine-tuning of the electronic structure[5] and/or (ii) introduction of functional moieties at the secondary coordination sphere of the iron center,[5-8] leading to enhanced catalytic performance. In this context, hydroquinone is a fascinating module to be introduced into the iron porphyrin framework because it functions as both an electron and proton reservoir.[17] Its electron-transporting nature can affect the electronic structure of the porphyrin, and its proton-donating nature can influence the environment of the secondary coordination sphere. In other words, hydroquinone is expected to modify both the electronic structure and secondary coordination sphere of an iron porphyrin complex. Thus, the introduction of a hydroquinone group(s) to the iron porphyrin scaffold is an intriguing strategy for obtaining an efficient catalyst for CO_2 reduction. However, to the best of my knowledge, there are no reports on an iron porphyrin complex with a hydroquinone moiety directly connected at the meso position.

In this chapter, I report the synthesis, characterization, and electrocatalytic CO_2 reduction activity of a novel iron porphyrin complex bearing a hydroquinone moiety at the meso position. Electrochemical analysis revealed that the introduction of a hydroquinone moiety enhances the catalytic activity for CO_2 reduction and lowers the overpotential for the catalytic reaction. Furthermore, quantum chemical calculations

clarified the crucial effect of the hydroquinone moiety on CO_2 reduction.

Results and discussions

Synthesis of complex Fe1

Scheme 1 (left, bottom) illustrates the molecular structure of the novel iron porphyrin complex developed in this study, 5,10,15-triphenyl-20-(2,5-dihydroxyphenyl)porphyrinato iron(III) chloride (**Fe1**). **Fe1** has an iron porphyrin framework with a hydroquinone moiety at the meso position. **Fe1** was synthesized according to the procedure shown in Scheme 2. A free base porphyrin, 5,10,15-triphenyl-20-(2,5-dihydroxyphenyl)porphyrin (**1**) was prepared using a modification of the previously reported method.[18] Compound **1** was characterized by ^{1}H-NMR spectroscopy, elemental analysis, and single-crystal X-ray crystallography (Figure 1 and Table 1). Figure 1a shows the ORTEP drawing of the structure **1**. Although the ORTEP drawings of the structure **1** shows eight oxygen atoms due to the disorder, the total occupancy of oxygen atom is constrained to be two. The occupancy of oxygen atom is reasonable because ^{1}H-NMR of **1** shows two OH protons (Figure 1b). The crystallographic parameters of **1** are summarized in Table 1. Subsequently, metal insertion to the free base porphyrin was performed by heating **1** with iron(III) chloride (20 equiv) as the metal source in *N*, *N*-dimethylformamide at 200 ˚C for 10 min using a microwave reactor. After the reaction, water was added to the reaction mixture to form a precipitate. The precipitate was collected by filtration, and the target compound, **Fe1**, was obtained in 72% yield. **Fe1** was characterized by elemental analysis and UV-visible absorption spectroscopy. Here, UV-vis absorption spectra of **1** and **Fe1** were measured in γ-butyrolactone (GBL). In the spectrum of **1** (Figure 2a), a strong absorption band, the so-called Soret band, and four weaker bands, the so-called Q-bands, were observed at 417 nm and at 514, 549, 591, and 647 nm, respectively. These absorption bands in the visible region are characteristic of porphyrin derivatives.[19] As shown in Figure 2b, **Fe1** exhibited Soret band associated with the porphyrin moiety at 414 nm. The position of this band is similar to that of **1**. In contrast, **Fe1** exhibited a smaller number of Q-bands (λ_{max} = 509 and 573 nm) than **1**. This observation supports that an iron ion is inserted into the porphyrin ring of **Fe1**.

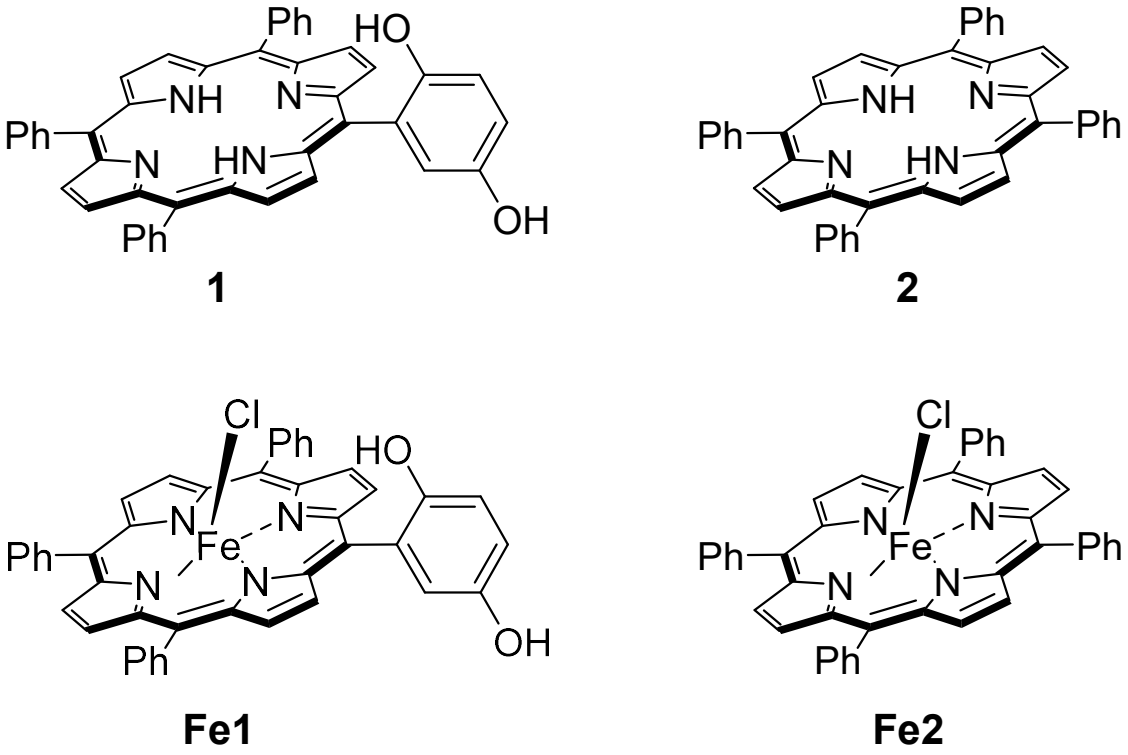

Scheme 1. Chemical structures of **1**, **2**, **Fe1** and **Fe2**.

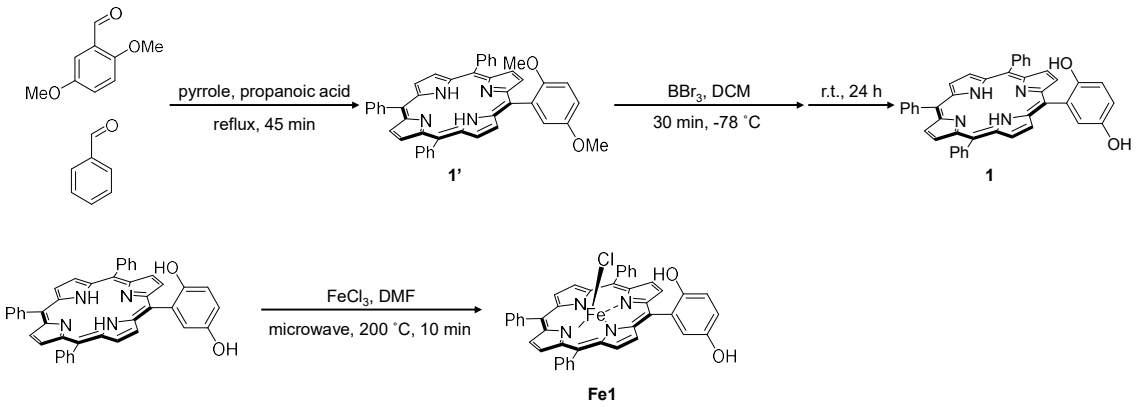

Scheme 2. Synthetic scheme for **Fe1**.

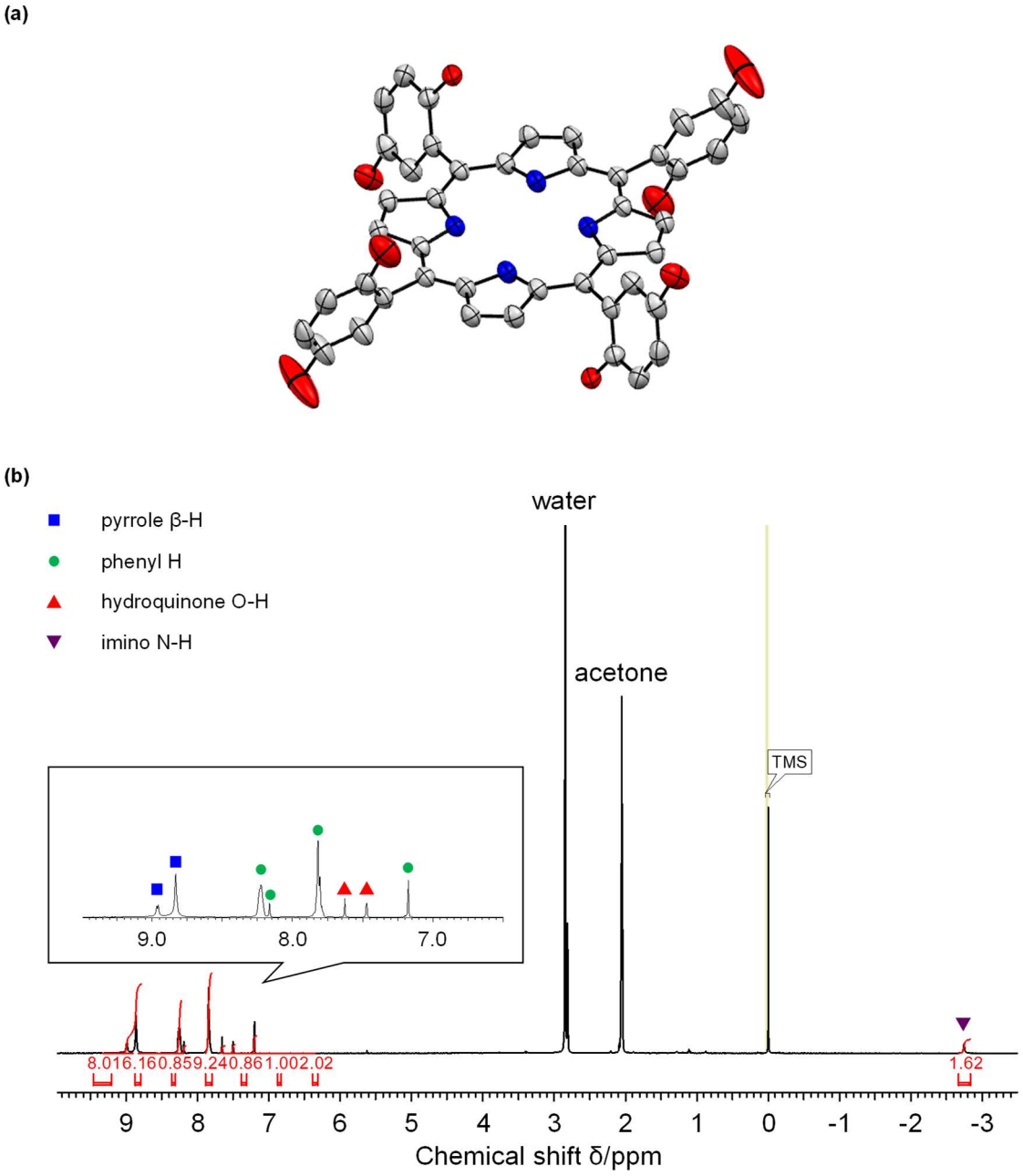

Figure 1. (a) ORTEP drawing of the structure of **1**. Non-coordinated solvent molecules and hydrogen atoms have been omitted for clarity. Thermal ellipsoids are shown at the 50% level. C = grey, N = blue and O = red. Note that the total number of occupancies of oxygen is constrained to be **2**. (b) ^{1}H-NMR spectrum of **1** (400 MHz, acetone-d_6).

Table 1. Summary of crystallographic data for **1**.

	1
Formula	$C_{44}H_{30}N_4O_2$
Fw	646.72
Crystal color, habit	Dark orange, plate
Crystal size / mm^3	0.021 × 0.064 × 0.149
Crystal system	Monoclinic
Space group	$P\,2_1/c$
a / Å	12.5640(5)
b / Å	11.6204(4)
c / Å	11.4629(5)
α / °	90
β / °	98.713(4)
γ / °	90
V / $Å^3$	1654.25
Z	2
F(000)	676.0
d_{calc} / g cm^{-3}	1.298
μ(MoKa) / mm^{-1}	0.081
T / K	123(2)
R_1	0.0491
wR_2	0.1211
GooF	1.030

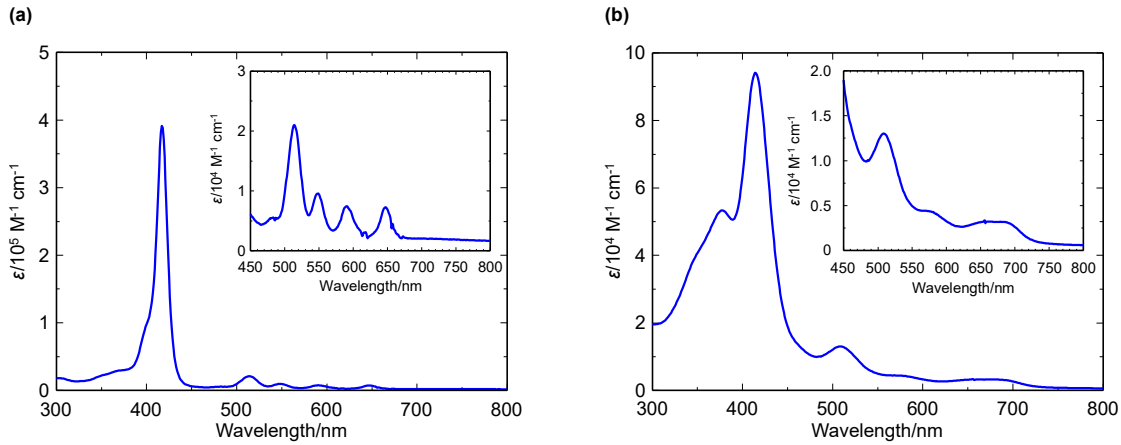

Figure 2. UV-vis absorption spectra of (a) **1** and (b) **Fe1** in GBL. The insets exhibit the enlarged UV-vis absorption spectra at Q-band region.

Cyclic voltammetry measurements

The cyclic voltammograms (CVs) and square wave voltammograms of the porphyrins were measured in a 0.1 M tetra-*n*-butylammonium perchlorate (TBAP)/GBL solution under Ar atmosphere. Compound **1** exhibited two reversible redox waves at –1.49 and –1.90 V [vs. ferrocene/ferrocenium (Fc/Fc^+)], as shown in Figure 3a and 3b (red line). These redox waves were assigned to the reduction processes of the porphyrin moiety because a free base porphyrin without a hydroquinone moiety, tetraphenylporphyrin (**2**), also exhibited two reversible waves at a similar potential region (–1.46 and –2.02 V), as shown in Figure 3a and 3b (blue line). In the CV of **Fe1**, two reversible redox waves were observed at –1.48 and –2.02 V (Figure 3c, red line). In addition, two irreversible reduction peaks were observed at –0.62 and –0.99 V. For comparison, the CV of an iron porphyrin complex without a hydroquinone moiety, 5,10,15,20-tetrakis(phenyl)porphyrinato iron(III) chloride (**Fe2**), was also measured (Figure 3c, blue line). In the CV of **Fe2**, three reversible redox peaks were observed at –0.68, –1.44, and –2.07 V. On the basis of comparison between the CVs of **Fe1** and **Fe2**, the reversible peaks at –1.48 and –2.02 V of **Fe1** were assigned to the reduction of the iron porphyrin scaffold. To investigate the origin of irreversible reduction peaks of **Fe1**, the CV of **Fe2** was then measured in the presence of hydroquinone. Two irreversible reduction peaks were observed at almost the same potentials (–0.66 and –0.94 V) as those of **Fe1** (Figure 3c, purple line), suggesting that these peaks are due to the interaction between the iron porphyrin complex and a hydroquinone moiety. Note that in the UV-visible absorption spectra of **Fe1** at various concentrations, the intensities of the peaks at 414 and 509 nm increased linearly upon increasing the concentration of **Fe1** (Figure 4a and 4b). This result indicates that **Fe1** satisfies Beers' law and does not form dimer in the range of the investigated concentrations. Therefore, the details of the interactions between the iron complex and a hydroquinone moiety are not clear at this stage. Subsequently, the CVs of the iron porphyrin complexes in a 0.1 M TBAP/GBL solution were measured under CO_2 in the presence of 2.0 M H_2O as the proton source. As shown in Figure 3d, both **Fe1** and **Fe2** exhibited an irreversible current, which indicates their electrocatalytic activity for CO_2 reduction. The intensity of the irreversible reduction wave of **Fe1** was more than twice as large as that of **Fe2**. The enhancement of the intensity of the irreversible catalytic current

was also observed in the CV of **Fe2** in the presence of 0.5 M hydroquinone (Figure 5a). Furthermore, in this experimental condition, the irreversible peak was also observed at −1.56 V(Figure 5b). This peak is assignable to the oxidative Fe-CO reassociation[20] ($Fe^{I}TPP^{-}$ + CO → $Fe^{II}TPP$-CO + e^{-}), and thus indicating that **Fe2** can promote the reduction of CO_2 to CO in the presence of hydroquinone. These results indicate that interaction between an iron porphyrin and hydroquinone is essential to efficiently catalyze CO_2 reduction. These results also suggest that the introduction of a hydroquinone moiety enhances the catalytic activity of **Fe1**. Notably, this also lowers the overpotential of the catalytic wave; the onset potential of **Fe1** was –1.89 V, which is 0.06 V higher than that of **Fe2** (–1.95 V, Figure 3d inset).

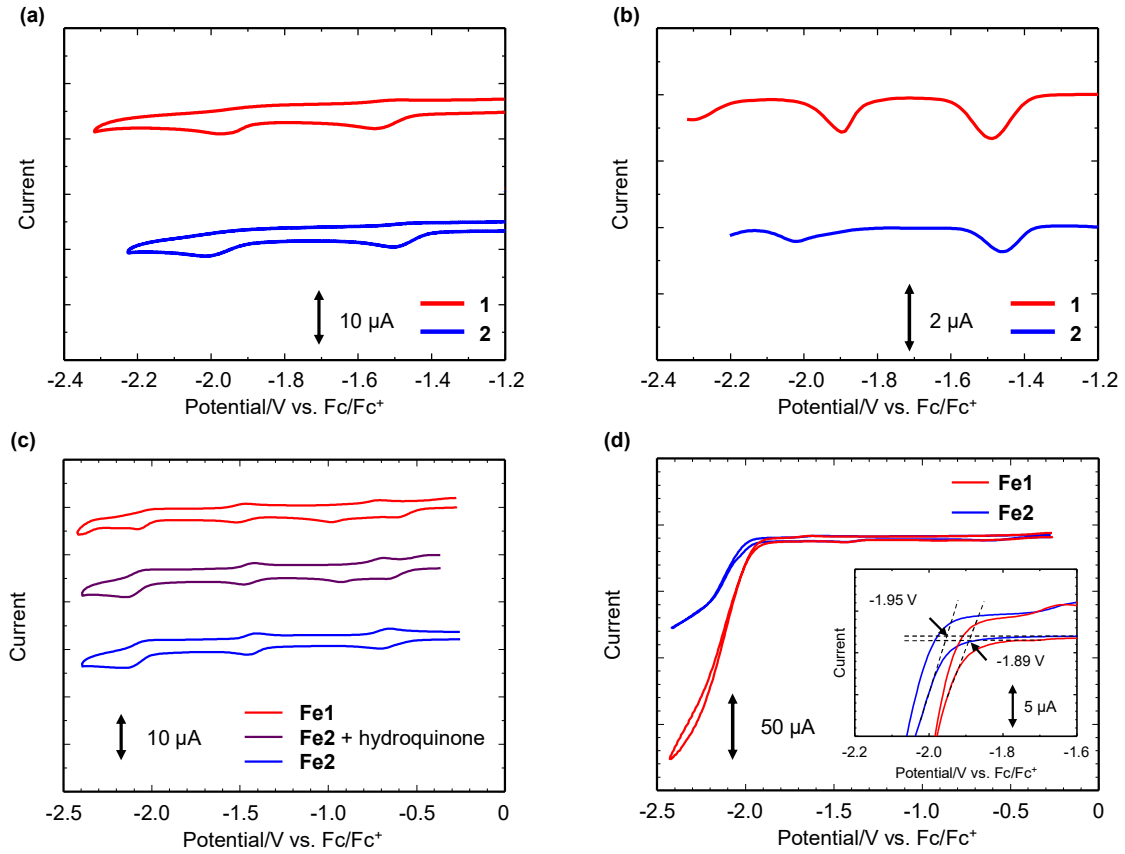

Figure 3. (a) Cyclic voltammograms of **1** (0.20 mM) and **2** in γ-butyrolactone (GBL) with tetra-*n*-butylammonium perchlorate (TBAP, 0.1 M) under Ar (scan rate: 100 mV s^{-1}). (b) Square wave voltammograms of **1** (0.20 mM) and **2** in GBL with TBAP (0.1 M) under Ar. Note that the measurement of **2** was performed using a saturated solution (less than 0.2 mM) due to its low solubility in the electrolyte solution. (c) Cyclic voltammograms of **Fe1** (0.20 mM), **Fe2** (0.20 mM) with hydroquinone (1.0 mM), and **Fe2** (0.20 mM) in GBL with TBAP (0.1 M) under Ar (scan rate: 100 mV s^{-1}). (d) Cyclic voltammograms of **Fe1** (0.20 mM) and **Fe2** (0.20 mM) in GBL with TBAP (0.1 M) in the presence of H_2O (2.0 M) under CO_2 (scan rate: 100 mV s^{-1}). The inset shows enlarged cyclic voltammograms focusing on the catalytic wave.

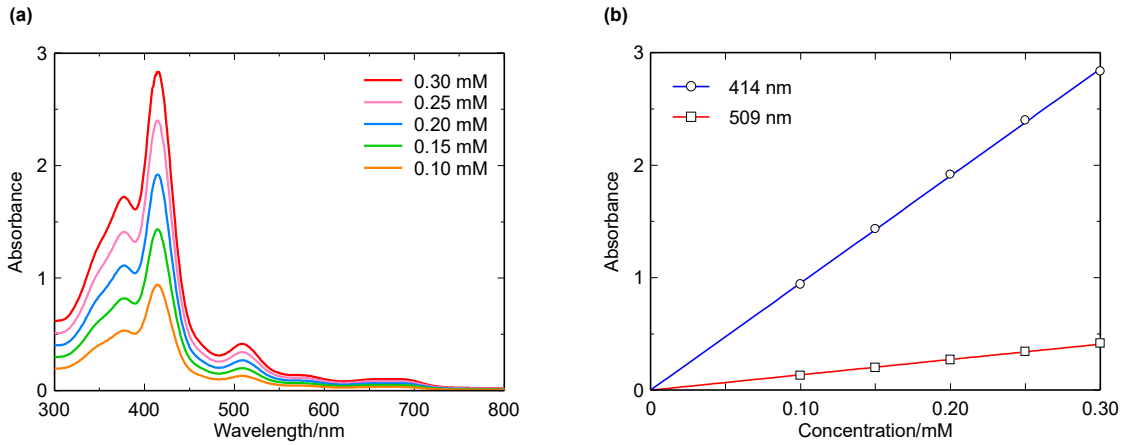

Figure 4. (a) UV-vis absorption spectra of **Fe1** (0.10, 0.15, 0.20, 0.25 and 0.30 mM) in GBL. Cell length is 1 mm. (d) Lambert-Beer plot for **Fe1** focusing on 414 nm and 509 nm in GBL.

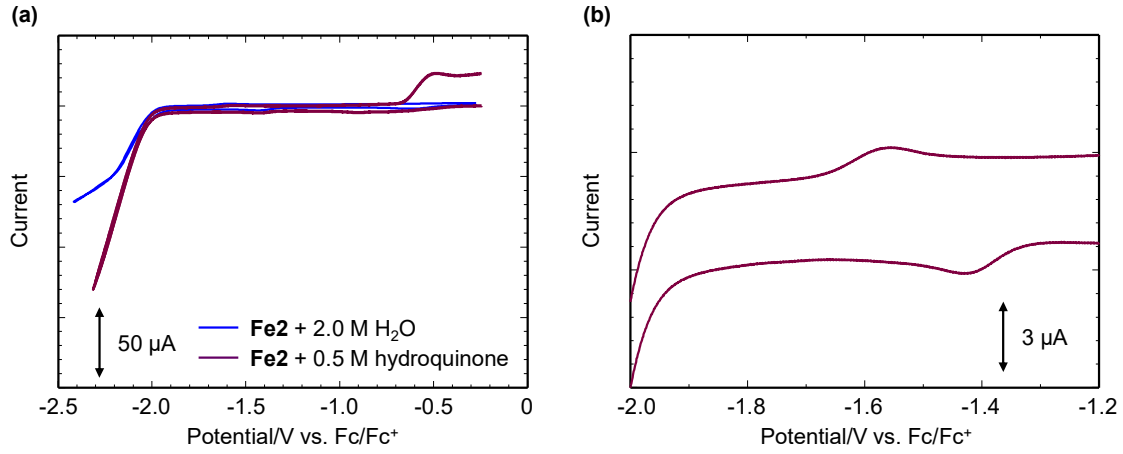

Figure 5. (a) Cyclic voltammograms of **Fe2** (0.20 mM) in a GBL solution with TBAP (0.1 M) in the presence of hydroquinone (0.5 M) under CO_2 (scan rate: 100 mV s^{-1}). (b) Enlarged cyclic voltammogram focusing on the oxidation peak at −1.56 V.

Controlled potential electrolysis experiments

To gain further insight into the catalytic activity of **Fe1**, controlled potential electrolysis (CPE) experiments were subsequently performed. CPE was conducted in a 0.1 M TBAP/acetonitrile (MeCN) solution containing 20 μM of the catalyst in the presence of 0.5 M phenol under CO_2 at –1.80 V vs. Fc/Fc^+ (Figure 6). MeCN was employed as the solvent for these experiments because, as shown in chapter 2 in details, it is one of the best solvents for efficient electrochemical CO_2 reduction by an iron porphyrin complex.[9] Phenol was used as a proton source because phenol is known to lower the overpotential in the electrochemical CO_2 reduction system catalyzed by iron porphyrin complexes.[21] In the CPE of **Fe1**, the total amount of charge was 5.0 C, and the formation of CO (Faradaic efficiency (FE): 53.2%) and H_2 (FE: 16.2%) was detected by gas chromatography (Figure 7 and Table 2, entry 1). Note that high-performance liquid chromatography analysis of the liquid phase did not detect the formation of HCOOH. For comparison, the CPE of the iron complex without a hydroquinone moiety was also performed. A perchlorate salt of **Fe2**, **Fe3**,[22] was used in the CPE experiment because **Fe2** does not dissolve in MeCN. In the CPE of **Fe3**, the total amount of charge passed over a period of 60 min was 1.8 C (Figure 7a and Table 1, entry 2), and the formation of H_2 with a FE of 7.1% was confirmed. However, CO and HCOOH were not detected, indicating that **Fe3** cannot catalyze CO_2 reduction under the employed experimental condition. These results clearly demonstrate that **Fe1** can catalyze CO_2 reduction to form CO at a lower overpotential compared with **Fe3**. In other words, the catalytic performance of the iron porphyrin complex can be improved by introducing a hydroquinone moiety. Note that CO_2 reduction products were not detected in the absence of catalyst (Figure 7a and Table 2, entry 3). I also performed CPE experiments of **Fe1** and **Fe3** at −2.00 V. In the CPE of **Fe1**, the total amount of charge passed during 1 h electrolysis was 7.1 C and the formation of CO was observed with a FE of 92% (Figure 7b and Table 2, entry 4). In the CPE of **Fe3**, the total amount of charge passed was 7.1 C and the FE of CO was 72.0% (Figure 7b and Table 2, entry 5). Although the total amounts of charge passed during the CPE experiments are almost identical between **Fe1** and **Fe3**, the selectivity for CO production is higher in **Fe1** than that in **Fe3**.

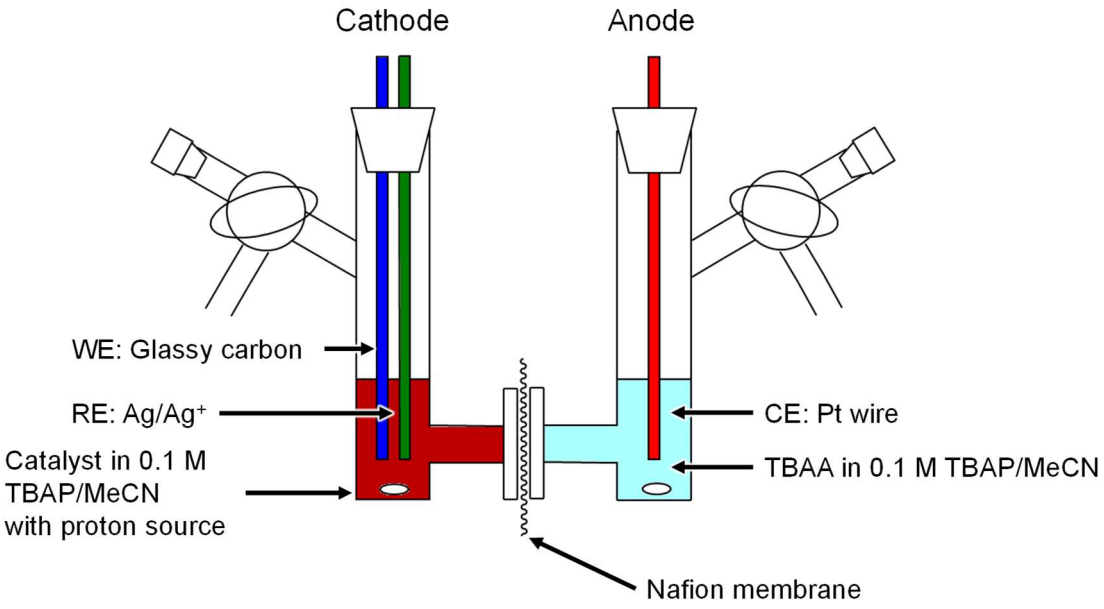

Figure 6. Schematic representation of the custom-designed two compartment cell used in the controlled potential electrolysis experiments.

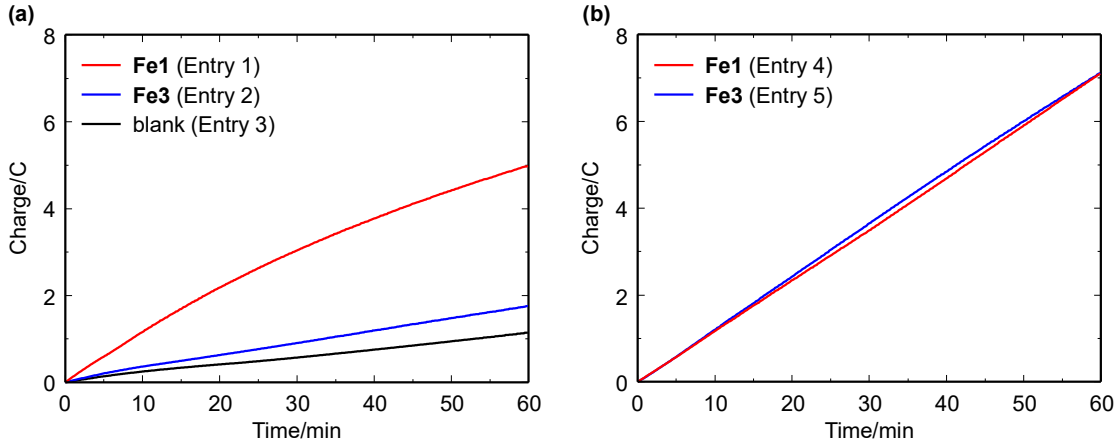

Figure 7. The results of CPE experiments of **Fe1** (20 μM) and **Fe3** (20 μM) at –1.80 V (vs. Fc/Fc^+) for 1 h. Details of the experimental condition and products are summarized in Table 2. Working electrode: glassy carbon (1.2 cm^2), counter electrode: Pt wire, reference electrode: Ag/Ag^+.

Table 2. Summary of the CPE experiments.

Entry	Catalyst	Solvent	[cat]/μM	Potential /V vs. Fc/Fc^+	Charge/C	Faradaic efficiency/%			
						CO	H_2	HCOOH	Total
1	**Fe1**	0.1 M TBAP/MeCN, 0.5 M PhOH	20	−1.80	5.0	53.2	16.2	n.d.	69.4
2	**Fe3**	0.1 M TBAP/MeCN, 0.5 M PhOH	20	−1.80	1.8	n.d.	7.1	n.d.	7.1
3	blank	0.1 M TBAP/MeCN, 0.5 M PhOH	-	−1.80	1.2	n.d.	11.0	n.d.	11.0
4	**Fe1**	0.1 M TBAP/MeCN, 0.5 M PhOH	20	−2.00	7.1	92.0	7.4	n.d.	99.4
5	**Fe3**	0.1 M TBAP/MeCN, 0.5 M PhOH	20	−2.00	7.1	71.9	17.0	5.6	94.5

The effect of a hydroquinone moiety

Finally, I investigated the effect of a hydroquinone moiety on catalysis. First, cyclic voltammetry measurements of **Fe1** and **Fe2** were performed under both Ar and CO_2 in the absence of a proton source. As Figure 8a shows, the third reduction wave of **Fe2** under Ar and CO_2 appeared exactly at the same potential (–2.01 V). On the contrary, the reduction wave of **Fe1** under CO_2 shifted to a more positive potential (–1.92 V) compared with that under Ar (–1.98 V, Figure 8b). These results suggest that the interaction between the iron porphyrin complex and CO_2 is strengthened by introducing a hydroquinone moiety. To clarify the origin of this phenomenon, I also performed quantum chemical calculations on the CO_2 adducts of the three electron reduced species of **Fe1** and **Fe2**. B3LYP-D3[23-25] were used as a functional. Here, LANL2DZ (with core potential) basis set was used on iron, and 6-31G(*d*) basis set was used on the rest of the atoms (C, H, N and O). Solvation effects were included implicitly by the Continuum Polarized Conductor Model (CPCM), with a dielectric constant mimicking MeCN.[26] All calculations were performed with the Gaussian 16 program package.[27] The optimized structure of the CO_2 adduct of **Fe1** indicates that the CO_2 coordinated to the iron center is hydrogen bonded to a hydroxy group of the hydroquinone moiety, while that in the CO_2 adduct of **Fe2** does not interact with the phenyl group of **Fe2** (Figure 9). In other words, hydroquinone stabilizes the CO_2-coordinated state of the iron porphyrin complex via hydrogen bond interaction, which would contribute to the lowering of the overpotential for CO_2 reduction. It should also be noted that this behavior is consistent with previous reports on iron porphyrin complexes bearing a local proton source.[5,6,8]

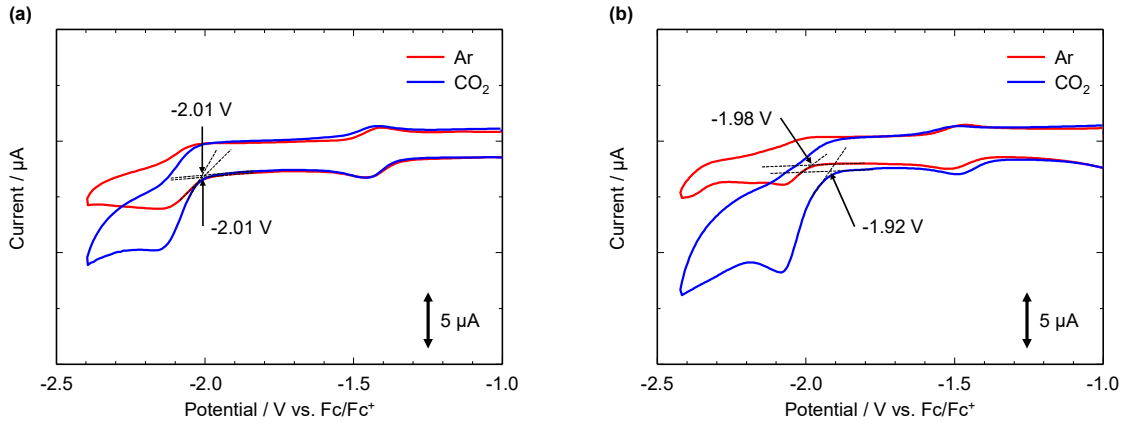

Figure 8. (a) Enlarged cyclic voltammograms of **Fe2** (0.20 mM) in GBL with TBAP (0.1 M) under Ar and CO_2 (scan rate: 100 mV s^{-1}). (b) Enlarged cyclic voltammograms of **Fe1** (0.20 mM) in GBL with TBAP (0.1 M) under Ar and CO_2 (scan rate: 100 mV s^{-1}).

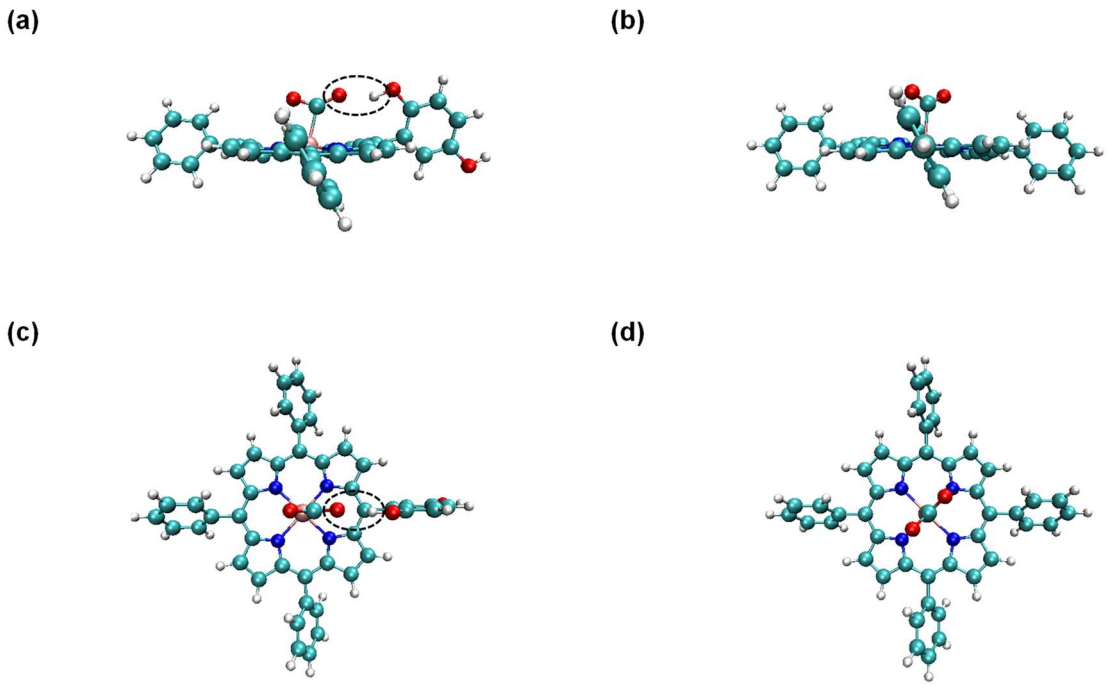

Figure 9. Optimized structures of CO_2 adduct of the three electron reduced species of **Fe1** and **Fe2**. (a) Side view of **Fe1**. (b) Side view of **Fe2**. (c) Top view of **Fe1**. (d) Top view of **Fe2**. C = green, H = white, N = blue and O = red, Fe = brown.

Conclusion

In conclusion, I have successfully synthesized and characterized a new iron porphyrin complex, **Fe1**, which bears a hydroquinone moiety at the meso position. Electrochemical analysis of the iron porphyrin complex, as well as the relevant complexes (**Fe2** and **Fe3**) under CO_2, indicated that the catalytic activity is improved by introducing a hydroquinone moiety. I also performed quantum chemical calculations on the CO_2 adducts of the iron porphyrin complexes and revealed that the affinity for CO_2 is increased by hydroquinone. This study clarifies that modification of the secondary coordination sphere with hydroquinone is an effective strategy for improving the catalytic activity of an iron porphyrin complex for CO_2 reduction.

Experimental section

General procedures

Pyrrole was purchased from Sigma-Aldrich Co., LLC. Benzaldehyde and ferrocene were purchased from Wako Pure Chemical Industries, Ltd. Propanoic acid was purchased from Kishida Chemical Co., LLC. Methanol, chloroform ($CHCl_3$), *N*, *N*-dimethylformamide (DMF), hexane, acetonitrile (MeCN), γ-butyrolactone (GBL), dichloromethane (DCM), ethyl acetate, methanol, ethanol, phenol, and iron(III) chloride were purchased from Kanto Chemical Co., Inc. Tetra-*n*-butylammonium perchlorate (TBAP), tetra-*n*-butylammonium acetate (TBAA), and 2,5-dimethoxybenzaldehyde were purchased from Tokyo Chemical Industry Co., Ltd. Acetone-d_6 and dichloromethane-d_2 were purchased from Cambridge Isotopes, Inc. Boron tribromide (BBr_3) was purchased from Sigma-Aldrich Co., LLC. All solvents and reagents are of the highest quality available and used as received except for TBAP. TBAP was recrystallized from absolute ethanol. ^{1}H-NMR spectra were collected at room temperature on a JEOL JNM-ECS400 spectrometer. Elemental analysis was performed on a J-SCIENCE LAB MICRO CORDER JM10 elemental analyzer. UV-visible absorption spectra were recorded on a UV-Vis Agilent Cary8454 spectrophotometer. MALDI-MS data were collected using a Bruker Autoflex III instrument.

Synthesis

Synthesis of 5,10,15-triphenyl-20-(2,5-dimethoxyphenyl)porphyrin (1')

1' was prepared by the modification of the previous report.[18] Pyrrole (0.65 mL, 9.18 mmol), 2,5-dimethoxybenzaldehyde (500.4 mg, 3.01 mmol) and benzaldehyde (0.62 mL, 6.08 mmol) were dissolved in propanoic acid (25 mL), then refluxed for 45 minutes and cooled to room temperature. Propanoic acid was then removed under reduced pressure. The resulting mixture was purified by silica gel column chromatography ($CHCl_3$) to afford a dark purple solution. Here, the second purple band includes **1'**. Recrystallization from DCM/ethanol gave a purple solid (83.2 mg, yield 6%). ^{1}H-NMR (400 MHz, dichloromethane-d_2): δ = 8.85 (s, 8H), 8.19-8.27 (m, 6H), 7.74-7.83 (m, 9H), 7.28-7.61 (d, d, s, 3H), 3.90 (s, 3H), 3.56 (s, 3H), –2.83 (s, 2H) ppm.

Synthesis of 5,10,15-triphenyl-20-(2,5-dihydroxyphenyl)porphyrin (1)

1' (20.0 mg, 0.03 mmol) was dissolved in DCM (5 mL), then BBr_3 (0.03 mL) was dropped slowly at –78 ˚C. The solution was maintained at –78 ˚C for 30 minutes. This mixture was then allowed to attain room temperature and was stirred for another 24 hours. At the end of this 24 hours period, water (10 mL) was added to quench the reaction and stirred for 30 minutes. After evaporating DCM, the resulting mixture was extracted with ethyl acetate. The extract was dried over anhydrous Na_2SO_4, and concentrated under reduced pressure. The resulting mixture was purified by silica gel column chromatography (ethyl acetate:hexane = 1:1) to afford the desired product. Recrystallization from DCM/hexane gave a purple solid (18.0 mg, yield 94%). MALDI-MS: m/z (**1**$^+$): 646.22. ^{1}H-NMR (400 MHz, acetone-d_6): δ = 8.82-9.01 (m, 8H), 8.26 (m, 6H), 8.19 (s, 1H), 7.80-7.89 (m, 9H), 7.66 (s, 1H), 7.50 (s, 1H), 7.20 (d, 2H), –2.75 (s, 2H) ppm. Elemental analysis Calcd. for $C_{44}H_{32}N_4O_3$ (**1**·1.0 H_2O): C, 79.50%; H, 4.85%; N, 8.43%. Found: C, 79.49%; H, 4.78%; N, 8.16%.

Synthesis of 5,10,15-triphenyl-20-(2,5-dihydroxyphenyl)porphyrinato iron(III) chloride (Fe1)

1 (40.0 mg, 0.03 mmol) and $FeCl_3$ (209 mg, 0.65 mmol) was dissolved in DMF (10 mL) at room temperature. The mixture was heated at 200 ˚C for 10 minutes by a microwave reactor. Diluted HCl (1 M, 50 mL) was added to the resulting solution. Precipitate was collected by filtration and washed with 1 M HCl. The precipitate was purified by silica gel chromatography (ethyl acetate:methanol = 1:1) to afford a desired product (34.6 mg, yield 72%). MALDI-MS: m/z (**Fe1**$^+$): 733.12. Elemental analysis Calcd. for $C_{44}H_{29}ClFeN_4O_{2.5}$ (**Fe1**·0.5 H_2O): C, 70.93%; H, 3.92%; N, 7.52%. Found: C, 70.86%; H, 4.17%; N, 7.71%. m/z is two smaller than that of calculated, suggesting the oxidation of a hydroquinone moiety to produce a benzoquinone moiety during the MALDI-MS measurement. Note that the elemental analysis of **Fe1** is consistent with the desired product.

Synthesis of tetraphenylporphyrin (2)

2 was prepared as previously described.[28] Pyrrole (1.7 mL, 25 mmol) and benzaldehyde (2.6 mL, 25 mmol) were dissolved in propanoic acid (50 mL), then refluxed for 45 minutes and cooled to room temperature. The resulting mixture was filtered and washed with methanol. Recrystallization from $CHCl_3$/methanol gave a purple solid (785 mg, yield 20%). MALDI-MS: m/z (**2**$^+$): 614.24. ^{1}H-NMR (400 MHz, $CDCl_3$): δ = 8.82 (s, 8H), 8.19-8.21 (m, 8H), 7.71-7.78 (m, 12H), –2.80 (s, 2H) ppm. Elemental analysis Calcd. for

$C_{44}H_{30.5}N_4O_{0.25}$ (**2**·0.25 H_2O): C, 85.34%; H, 4.96%; N, 9.05%. Found: C, 85.24%; H, 4.68%; N, 9.08%.

Synthesis of 5,10,15,20-tetrakis(phenyl)porphyrinato iron(III) chloride (Fe2)

Fe2 was prepared by the modification of a previous report.[29] To a solution of **2** (200 mg, 0.32 mmol) in DMF (10 mL), a DMF 10 mL solution of $FeCl_3$ (519 mg, 3.2 mmol) was added at room temperature. The mixture was heated at 200 ˚C for 1 hour by a microwave reactor. Diluted HCl (1 M, 50 mL) was added to the resulting solution. Precipitate was collected by filtration and washed with 1 M HCl. Recrystallization from $CHCl_3$/hexane gave a purple solid (191 mg, yield 85%). MALDI-MS: m/z (**Fe2**$^+$): 703.15. Elemental analysis Calcd. for $C_{44}H_{28}ClFeN_4$ (**Fe2**): C, 75.06%; H, 4.01%; N, 7.96%. Found: C, 74.98%; H, 4.08%; N, 8.01%.

Synthesis of 5,10,15,20-tetrakis(phenyl)porphyrinato iron(III) perchlorate (Fe3)

To a solution of **Fe2** (50 mg, 0.071 mmol) in tetrahydrofuran THF (14 mL), an MeCN (1 mL) solution of $AgClO_4$·H_2O (14.7 mg, 0.071 mmol) was added at room temperature. The mixture was stirred at room temperature for 1 hour. Precipitate (AgCl) was removed and the residual THF solution was collected. Recrystallization from THF/heptane gave a purple solid (42 mg, yield 77%). Elemental analysis Calcd. for $C_{49}H_{38}ClFeN_4O_{5.25}$ (**Fe3**·1.25 THF): C, 68.58%; H, 4.46%; N, 6.53%. Found: C, 68.30%; H, 4.63%; N, 6.72%.

Electrochemistry

Electrochemical experiments were performed at room temperature on a BAS ALS Model 650DKMP electrochemical analyzer or a Bio-Logic-Science Instruments potentiostat. Cyclic voltammetry (CV) measurements were performed by using a one-compartment cell with a three-electrode configuration, which consisted of a glassy carbon disk (diameter 3 mm, BAS Inc.), platinum wire, and Ag/Ag^+ electrode (Ag/0.01 M $AgNO_3$) as the working, auxiliary, and reference electrodes, respectively. The glassy carbon disc working electrode was polished using 0.05 μm alumina paste (BAS Inc.) and washing with purified H_2O prior to each measurement. Ferrocene was used as an internal standard and all potentials are referenced to the ferrocenium/ferrocene (Fc/Fc^+) couple at 0 V.

Controlled potential electrolysis (CPE)

CPE was performed in a gas-tight two-compartment electrochemical cell, where the first compartment held the carbon plate working electrode (1.2 cm^2 surface area) and Ag/Ag^+ reference electrode (Ag/0.01 M $AgNO_3$) in 5 ml of 0.1 M TBAP/MeCN with catalyst and proton source, while the second compartment held the Pt auxiliary electrode in 5 ml of 0.1 M TBAP/MeCN containing TBAA (40 mM) as sacrificial oxidant. The two compartments were separated by a Nafion® membrane. The solution was purged vigorously with CO_2 for 30 mins prior to electrolysis. The electrolysis experiment was performed for 1 h under constant stirring. The amount of CO and H_2 produced was quantified from an analysis of the headspace with a Shimadzu GC-8A with TCD detector equipped with a capillary column with Molecular Sieve 13X-S 60/80. Calibration curves were made by sampling known amounts of H_2 and CO.

X-ray crystallography

Single crystal X-ray diffraction data were collected on a Synergy Custom system CCD Plate equipped with confocal monochromated Mo-Kα radiation (λ = 0.71069 Å) coated with Paratone-N (Hampton Research Corp., Aliso Viejo, CA, USA). Data was processed using CrysAlisPro system software.[30] The structure was solved by dual-space algorithm using SHELXT program[31] through the Olex2 interface.[32] All non-hydrogen atoms were refined anisotropically using a least-squares method, and hydrogen atoms were fixed at calculated positions and refined using a riding model. SHELXL−2014/7 was used for structure refinement.[33] Full-matrix least-squares refinements on F^2 based on unique reflections with unweighted and weighted agreement factors of $R = \Sigma||F_o| - |F_c||/\Sigma|F_o|$ ($I > 2.00\ \sigma(I)$) and $wR = [\Sigma w(F_o^2 - F_c^2)^2/\Sigma w(F_o^2)^2]^{1/2}$ were performed. Mercury 4.0.0 was used for visualization and analysis of the structure. Crystallographic data have been deposited with Cambridge Crystallographic Data Centre: Deposition numbers CCDC 2121769 for **1**. Copies of the data can be obtained free of charge via www.ccdc.cam.ac.uk/data_request/cif.

References

[1] A. M. Appel, J. E. Bercaw, A. B. Bocarsly, H. Dobbek, D. L. DuBois, M. Dupuis, J. G. Ferry, E. Fujita, R. Hille, P. J. A. Kenis, C. A. Kerfeld, R. H. Morris, C. H. F. Peden, A. R. Portis, S. W. Ragsdale, T. B. Rauchfuss, J. N. H. Reek, L. C. Seefeldt, R. K. Thauer, G. L. Waldrop, Chem. Rev. **2013**, *113*, 6621.

[2] R. Francke, B. Schille, M. Roemelt, *Chem. Rev*. **2018**, *118*, 4631.

[3] E. Boutin, L. Merakeb, B. Ma, B. Boudy, M. Wang, J. Bonin, E. Anxolabéhère-Mallart, M. Robert, *Chem. Soc. Rev*. **2020**, *49*, 5772.

[4] C. Costentin, S. Drouet, G. Passard, M. Robert, J.-M. Savéant, *J. Am. Chem. Soc.* **2013**, *135*, 9023.

[5] C. Costentin, G. Passard, M. Robert, J.-M. Savéant, *J. Am. Chem. Soc*. **2014**, *136*, 11821.

[6] E. M. Nichols, J. S. Derrick, S. K. Nistanaki, P. T. Smith, C. J. Chang, *Chem. Sci*. **2018**, *9*, 2952.

[7] I. Azcarate, C. Costentin, M. Robert, J.-M. Savéant, *J. Am. Chem. Soc*. **2016**, *138*, 16639.

[8] S. Sinha, J. J. Warren, *Inorg. Chem*. **2018**, *57*, 12650.

[9] K. Kosugi, M. Kondo, S. Masaoka, *Angew. Chem., Int. Ed*. **2021**, *60*, 22070.

[10] W. Nie, D. E. Tarnopol, C. C. L. McCrory, *J. Am. Chem. Soc*. **2021**, *143*, 3764.

[11] C. Cometto, L. Chen, P.-K. Lo, Z. Guo, K.-C. Lau, E. Anxolabéhère-Mallart, C. Fave, T.-C. Lau, M. Robert, *ACS Catal*. **2018**, *8*, 3411.

[12] J. S. Derrick, M. Loipersberger, R. Chatterjee, D. A. Iovan, P. T. Smith, K. Chakarawet, J. Yano, J. R. Long, M. Head-Gordon, C. J. Chang, *J. Am. Chem. Soc*. **2020**, *142*, 20489.

[13] M. D. Sampson, C. P. Kubiak, *J. Am. Chem. Soc*. **2016**, *138*, 1386.

[14] L.-M. Cao, H.-H. Huang, J.-W. Wang, D.-C. Zhong, T.-B. Lu, *Green Chem*. **2018**, *20*, 798.

[15] S. K. Lee, M. Kondo, G. Nakamura, M. Okamura, S. Masaoka, *Chem. Commun*. **2018**, *54*, 6915.

[16] K.-Y. Wong, W.-H. Chung, C.-P. Lau, *J. Electroanal. Chem*. **1998**, *453*, 161.

[17] J. J. Warren, T. A. Tronic, J. M. Mayer, *Chem. Rev*. **2010**, *110*, 6961.

[18] F. D'Souza, *J. Am. Chem. Soc*. **1996**, *118*, 923.

[19] M. Gouterman, *J. Chem. Phys*. **1959**, *30*, 1139.

[20] C. Costentin, S. Drouet, G. Passard, M. Robert, J. M. Saveant, *J. Am. Chem. Soc*. **2013**, *135*, 9023.

[21] C. Costentin, S. Drouet, M. Robert, S. Savéant, *Science* **2012**, *338*, 90.

[22] The electrochemical properties of **Fe3** were investigated in detail in ref. 9.

[23] A. D. Becke, *J. Chem. Phys*. **1993**, *98*, 5648.

[24] C. Lee, W. Yang, R. G. Parr, *Phys. Rev. B*. **1988**, *37*, 785.

[25] S. Grimme, *J. Chem. Phys*. **2006**, *124*, 034108.

[26] J. Tomasi, B. Mennucci, R. Cammi, *Chem. Rev*. **2005**, *105*, 2999.

[27] *Gaussian 16*, Revision C.01, M. J. Frisch, G. W. Trucks, H. B. Schlegel, G. E. Scuseria, M. A. Robb, J. R. Cheeseman, G. Scalmani, V. Barone, G. A. Petersson, H. Nakatsuji, X. Li, M. Caricato, A. V. Marenich, J. Bloino, B. G. Janesko, R. Gomperts, B. Mennucci, H. P. Hratchian, J. V. Ortiz, A. F. Izmaylov, J. L. Sonnenberg, D. Williams-Young, F. Ding, F. Lipparini, F. Egidi, J. Goings, B. Peng, A. Petrone, T. Henderson, D. Ranasinghe, V. G. Zakrzewski, J. Gao, N. Rega, G. Zheng, W. Liang, M. Hada, M. Ehara, K. Toyota, R. Fukuda, J. Hasegawa, M. Ishida, T. Nakajima, Y. Honda, O. Kitao, H. Nakai, T. Vreven, K. Throssell, J. A. Montgomery, Jr., J. E. Peralta, F. Ogliaro, M. J. Bearpark, J. J. Heyd, E. N. Brothers, K. N. Kudin, V. N. Staroverov, T. A. Keith, R. Kobayashi, J. Normand, K. Raghavachari, A. P. Rendell, J. C. Burant, S. S. Iyengar, J. Tomasi, M. Cossi, J. M. Millam, M. Klene, C. Adamo, R. Cammi, J. W. Ochterski, R. L. Martin, K. Morokuma, O. Farkas, J. B. Foresman, and D. J. Fox, Gaussian, Inc., Wallingford CT, 2016.

[28] A. D. Alder, F. R. Long, W. Shergalis, *J. Am. Chem. Soc*. **1964**, *86*, 3145.

[29] S. L. Rebelo, A. M. N. Silva, C. J. Medforth, C. Freire, *Molecules* **2016**, *21*, 481.

[30] CrysAlisPro, Oxford Diffraction Ltd., Version 1.171.39.46.

[31] G. M. Sheldrick, *Acta Cryst*. **2015**, A71, 3.

[32] O. V. Dolomanov, L. J. Bourhis, R. J. Gildea, J. A. K. Howard, H. Puschmann, *J. Appl. Crystallogr*. **2009**, *42*, 339.

[33] G. M. Sheldrick, *Acta Cryst*. **2015**, A71, 3.

Chapter 2

Quick and Easy Method to Dramatically Improve the Electrochemical CO_2 Reduction Activity of an Iron Porphyrin Complex

Introduction

The catalytic reduction of CO_2 into fuels or useful chemicals has attracted much attention because this technology can potentially solve both energy and environmental problems.[1] Therefore, in the past few decades, extensive efforts have been made to develop efficient molecular catalysts for the reduction of CO_2.[2–16] In general, the catalytic activity of this class of compounds can be improved by chemical modifications in the vicinity of the catalytic center. Among these compounds, iron(III) porphyrin complexes are one of the best catalytic centers because of their (i) high turnover frequency (TOF), (ii) high selectivity for CO_2 to CO conversion, and (iii) robustness (Figure 1a). Their catalytic activity can be further improved by introducing various substituents, such as acid/base groups, electron-donating/withdrawing moieties, and a pendant amide at meso positions, that accelerate the CO_2 binding step (Figure 1b).[7,8,10,12] However, the introduction of functional substituents often requires complicated synthetic procedures and is expensive. Therefore, a more facile and low-cost method for improving the catalytic activity of iron(III) porphyrin complexes is required.

In this chapter, I report a "quick and easy" method for the dramatic enhancement of the electrochemical CO_2 reduction activity of iron porphyrin complexes. The simple one-pot counter anion exchange reaction of a commercially available catalyst, iron(III) tetraphenylporphyrin chloride (**FeTPP-Cl**), afforded a complex with improved solubility, iron (III) tetraphenylporphyrin (**FeTPP**). **FeTPP** exhibited the highest TOF for CO_2 reduction among the best-in-class molecular catalysts in appropriate reaction medium (Figure 1c). I have also clarified the effect of changing the reaction medium on the reaction mechanism.

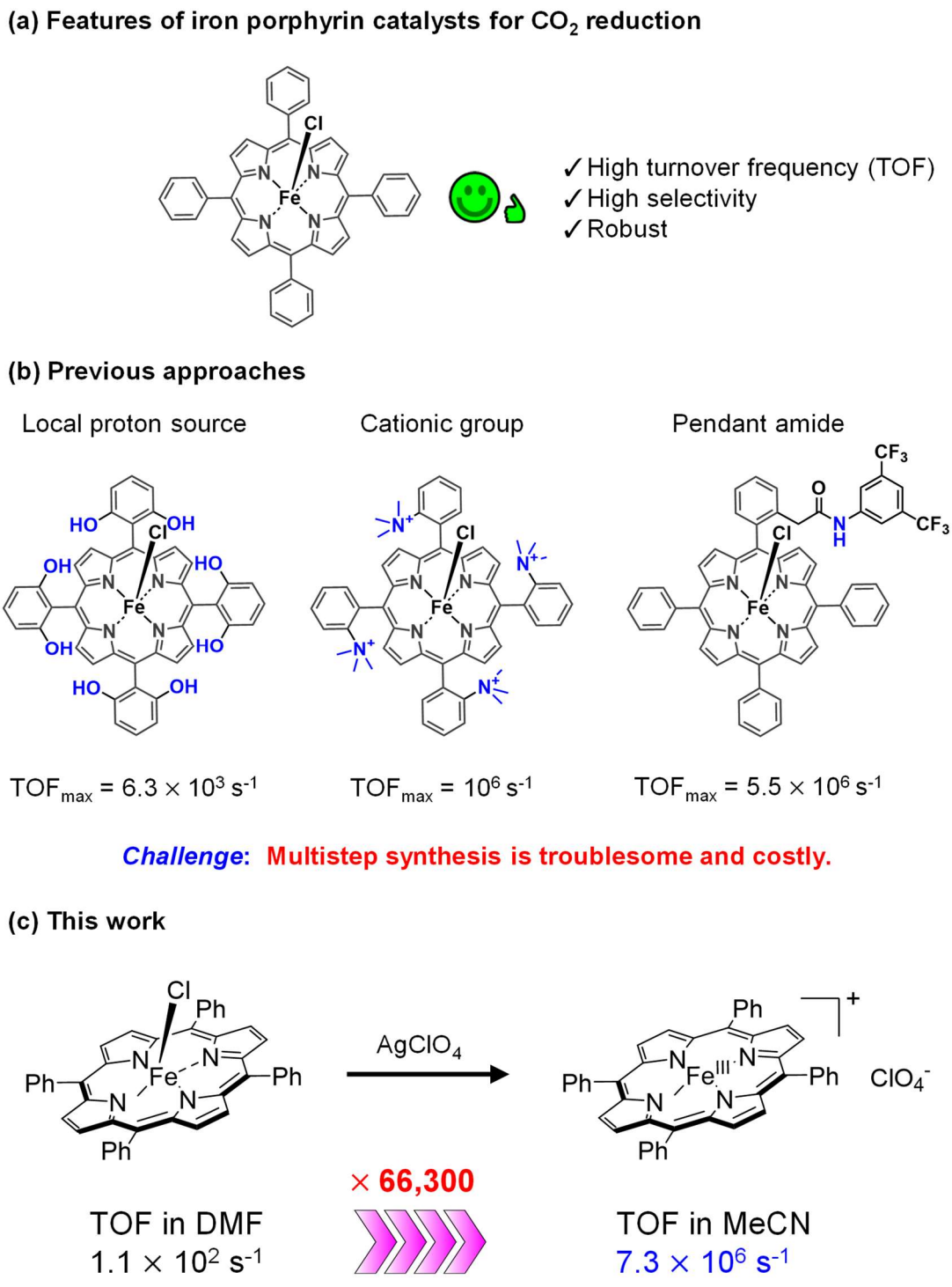

Figure 1. (a) Features of iron porphyrin catalysts for CO_2 reduction. (b) Previous approaches for improving catalytic activity. (c) Summary of this work.

Results and discussions

Cyclic voltammetry measurements

I began by reinvestigating CO_2 reduction by **FeTPP-Cl** in DMF, a common solvent for iron porphyrin systems, as DMF can dissolve both the complex and CO_2 at high concentration.[4–11] The cyclic voltammogram of **FeTPP-Cl** was measured in a 0.1 M tetra-*n*-butyl ammonium perchlorate (TBAP)/DMF solution in the presence of 0.5 M trifluoroethanol (TFE) as a proton source. **FeTPP-Cl** indeed exhibited a large irreversible current approximately at –2.06 V [vs. ferrocene/ferrocenium (Fc/Fc^+)] under CO_2, corresponding to the electrocatalytic reduction of CO_2 (Figure 2a, red line). Unexpectedly, the intensity of the irreversible current increased when acetonitrile (MeCN) was added (Figure 2a, dashed lines). This observation prompted us to explore the influence of MeCN on catalysis. However, **FeTPP-Cl** does not dissolve in pure MeCN, which would hamper further investigation.

As a solution to this problem, I performed the counteranion exchange reaction of **FeTPP-Cl**[17] and prepared the perchlorate salt of **FeTPP** (**FeTPP-ClO_4**). **FeTPP-ClO_4** was characterized by elemental and single-crystal X-ray structural analyses (Figure 3 and Table 1). **FeTPP-ClO_4** was well soluble in various solvents, which enabled us to perform electrochemical measurements of the complex in MeCN.

Initially, the cyclic voltammogram of **FeTPP-ClO_4** was measured in a 0.1 M TBAP/MeCN solution. Under Ar, **FeTPP-ClO_4** in MeCN exhibited three redox waves. The potential of the first redox wave (–0.26 V, Figure 2b and Table 2), which is attributed to the Fe(III)/Fe(II) redox couple,[4–6] was shifted to more positive potential compared with that of **FeTPP-Cl** (–0.63 V). Note that the first reduction of **FeTPP-Cl** involves the dissociation of the coordinated chloride ligand;[18] thus, the observed difference between the first redox potentials of **FeTPP-ClO_4** in MeCN and **FeTPP-Cl** in DMF can be attributed to the difference in anion. The second [Fe(II)/Fe(I) redox couple] and third [Fe(I)/Fe(0) redox couple] redox waves were reversible for both **FeTPP-ClO_4** in MeCN and **FeTPP-Cl** in DMF (Figure 4). Moreover, the two catalysts have similar potentials for these redox waves. A CV of **FeTPP-ClO_4** in a 0.1 M TBAP/DMF solution under Ar also exhibited three reversible redox waves (Figure 2b, purple line, and Table 2), which is similar to **FeTPP-Cl** in DMF except for the first reduction wave. These results indicate

that electronic structure of the porphyrin scaffold is not affected by counter anions.

The diffusion constants of the complexes were also evaluated by the slope of Figure 4 and Randles-Sevcik equation

$$I_{\mathrm{P}} = 0.4463nFAC_{\mathrm{cat}}^{*}\sqrt{\frac{nFv}{RT}}\sqrt{D_{\mathrm{cat}}}, \quad (1)$$

where n is the number of electrons (n = 1), F is the Faradaic constant (96485 C mol^{-1}), A is the electrode surface area (0.071 cm^2), C_{cat}^{*} is the concentration of the catalyst (mol cm^{-3}), R is the gas constant (8.31 J K^{-1} mol^{-1}), v is the scan rate (V s^{-1}), D_{cat} is the diffusion coefficient of the catalyst (cm^2 s^{-1}) and T is the temperature (298.15 K). Resemble results were obtained in DMF and MeCN, and they are summarized in Table 3.

On the other hand, under CO_2 with 0.5 M TFE, there was a significant difference between the cyclic voltammograms in MeCN and DMF. The intensity of the irreversible reduction wave increased dramatically, and the onset potential shifted to more positive potential (ca. –1.91 V) in MeCN compared with that in DMF (Figure 2a, blue line). These results suggest that the catalytic activity is enhanced in MeCN.

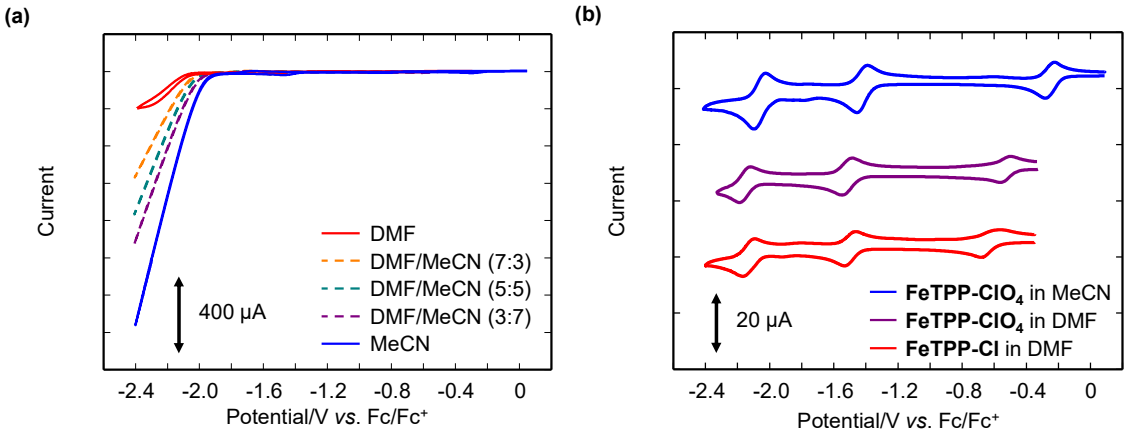

Figure 2. (a) Cyclic voltammograms of **FeTPP-Cl** (0.50 mM) in DMF/MeCN (10:0, 7:3, 5:5, and 3:7) and **FeTPP-ClO$_4$** (0.50 mM) in MeCN with TBAP (0.1 M) in the presence of TFE (0.5 M) under CO_2 (scan rate: 100 mV s^{-1}). (b) Cyclic voltammograms of **FeTPP-ClO$_4$** (0.50 mM) in MeCN (blue line) and DMF (purple line) and **FeTPP-Cl** (0.50 mM) in DMF (red line) with TBAP (0.1 M) under Ar (scan rate: 100 mV s^{-1}).

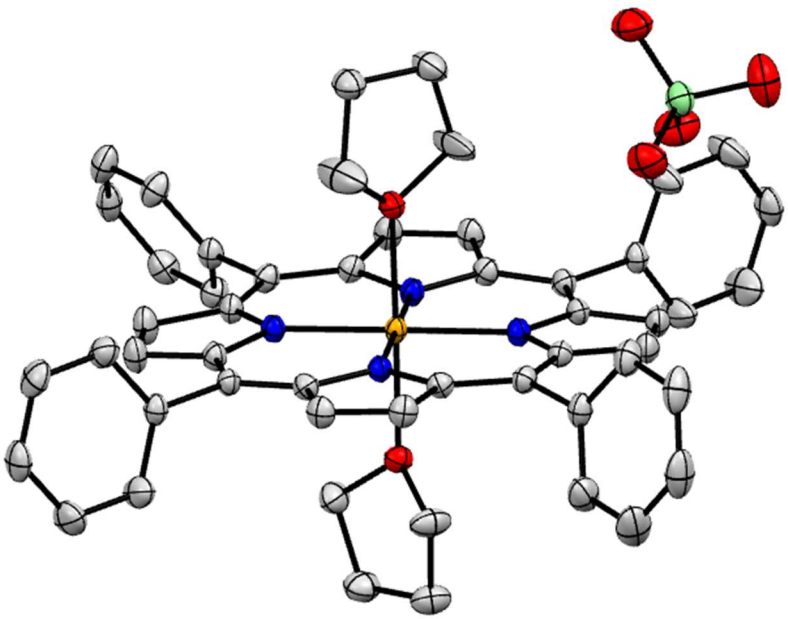

Figure 3. ORTEP drawing of the structure of **FeTPP-ClO$_4$**. Non-coordinated solvent molecules and hydrogen atoms have been omitted for clarity. Thermal ellipsoids are shown at the 50% level. O = red, C = grey, N = blue, Cl = green and Fe = orange.

Table 1. Summary of crystallographic data for **FeTPP-ClO$_4$**.

	FeTPP-ClO$_4$
Formula	$C_{52}H_{44}N_4O_2Fe{\cdot}2.0\ C_4H_8O$
Fw	1056.42
Crystal color, habit	Clear dark brown, plate
Crystal size / nm^3	0.177 × 0.486 × 0.535
Crystal system	Triclinic
Space group	$P\bar{1}$
a / Å	10.6138(2)
b / Å	13.3714(2)
c / Å	18.5626(3)
α / °	78.5360(10)
β / °	86.6710(10)
γ / °	83.2290(10)
V / Å^3	2562.24
Z	2
F(000)	1110
d_{calc} / g cm^{-3}	1.369
μ(MoKα) / mm^{-1}	0.409
T / K	123(2)
R_1	0.0593
wR_2	0.1731
GooF	1.088

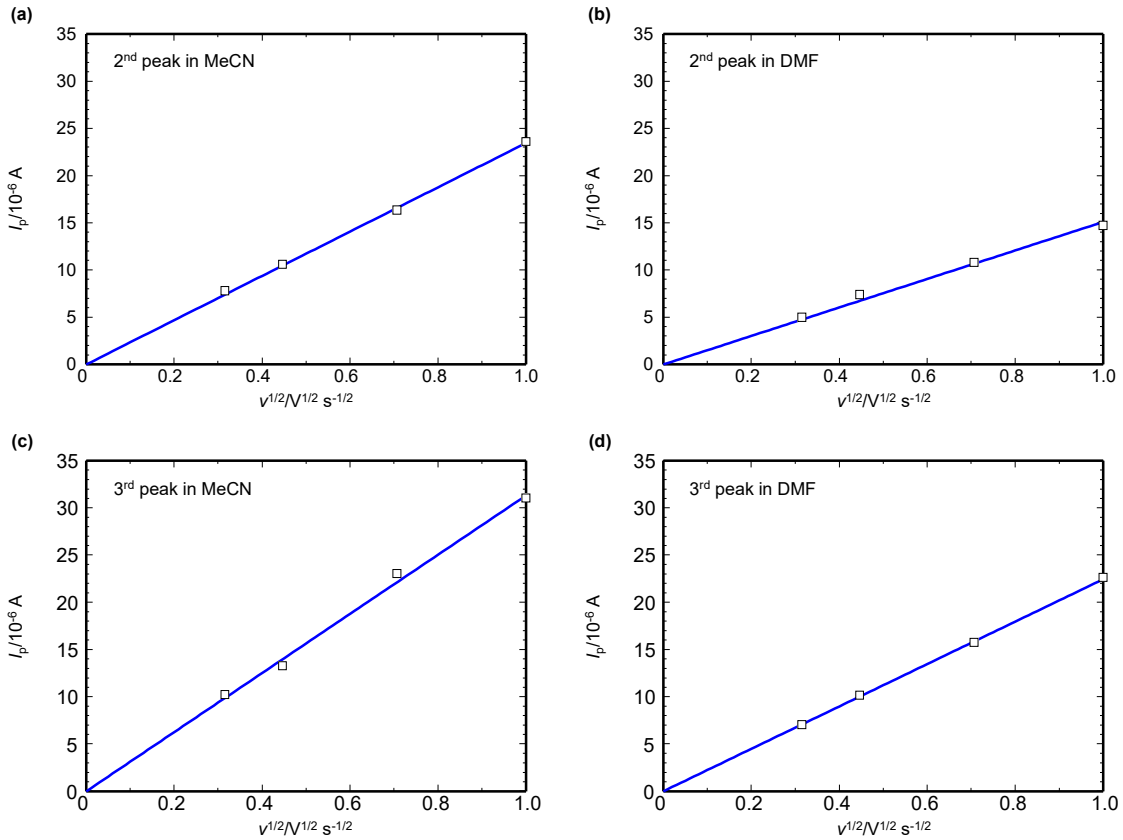

Figure 4. Variation of peak current of (a) **FeTPP-ClO$_4$** (0.5 mM) in 0.1 M TBAP/MeCN at the second redox wave (b) **FeTPP-Cl** (0.5 mM) in 0.1 M TBAP/DMF at the second redox wave (c) **FeTPP-ClO$_4$** (0.5 mM) in 0.1 M TBAP/MeCN at the third redox wave, and (d) **FeTPP-Cl** (0.5 mM) in 0.1 M TBAP/DMF at the third redox wave versus square root of scan rate.

Table 2. Redox potentials ($E_{1/2}$/V vs. Fc/Fc$^+$) of **FeTPP-Cl** (0.5 mM) in 0.1 M TBAP/DMF, **FeTPP-ClO$_4$** (0.5 mM) in 0.1 M TBAP/DMF and **FeTPP-ClO$_4$** (0.5 mM) in 0.1 M TBAP/MeCN under Ar.

Catalyst	Solvent	$E_{1/2}(1)$	$E_{1/2}(2)$	$E_{1/2}(3)$
FeTPP-Cl	DMF	–0.63	–1.51	–2.14
FeTPP-ClO$_4$	DMF	–0.53	–1.51	–2.15
FeTPP-ClO$_4$	MeCN	–0.26	–1.43	–2.06

Table 3. Summary of the diffusion constant.

Catalyst	Solvent	D/cm^2 s^{-1} (2nd peak)	D/cm^2 s^{-1} (3rd peak)
FeTPP-ClO$_4$	0.1 M TBAP/MeCN	6.11×10^{-6}	1.07×10^{-5}
FeTPP-Cl	0.1 M TBAP/DMF	2.52×10^{-6}	5.60×10^{-6}

Controlled potential electrolysis experiments

To quantify the catalytic product, controlled potential electrolysis (CPE) experiments were then performed both in DMF and MeCN with 1.0 M TFE and 0.1 M TBAP under CO_2 at –2.35 V vs. Fc/Fc^+. In CPE experiments, tetra-*n*-butylammonium acetate (TBAA) was added in the anodic chamber (Figure 5) to scavenge holes generated on the Pt counter electrode. TBAA reacts at anode to consume the holes and to produce CO_2 and ethane via Kolbe reaction.[19] In the CPE of **FeTPP-Cl** in DMF, the total amount of charge passed over a period of 60 min was 3.9 C when 0.01 mM of catalyst was used (Figure 6, red line), and CO (4.5 μmol) was formed with a Faradaic efficiency (FE) of 23%. The similar catalytic performance was also obtained in the CPE of **FeTPP-ClO$_4$** in DMF; 2.6 C of charge has passed, and the formation of CO (FE: 21.9%), H_2 (FE: 17.4%) was detected, indicating that catalytic performance is not affected by counter anions. Upon increasing the catalyst concentration to 0.50 mM, CO (27.0 μmol) was formed with a total charge and FE of 5.7 C and 92%, respectively. On the other hand, in the CPE of **FeTPP-ClO$_4$** in MeCN, the total amount of charge was 33.3 C and the FE was 98% (170.0 μmol), even at a low catalyst concentration (0.01 mM). These results clearly demonstrate that the electrocatalytic activity of **FeTPP** for CO_2 reduction is significantly enhanced in MeCN.

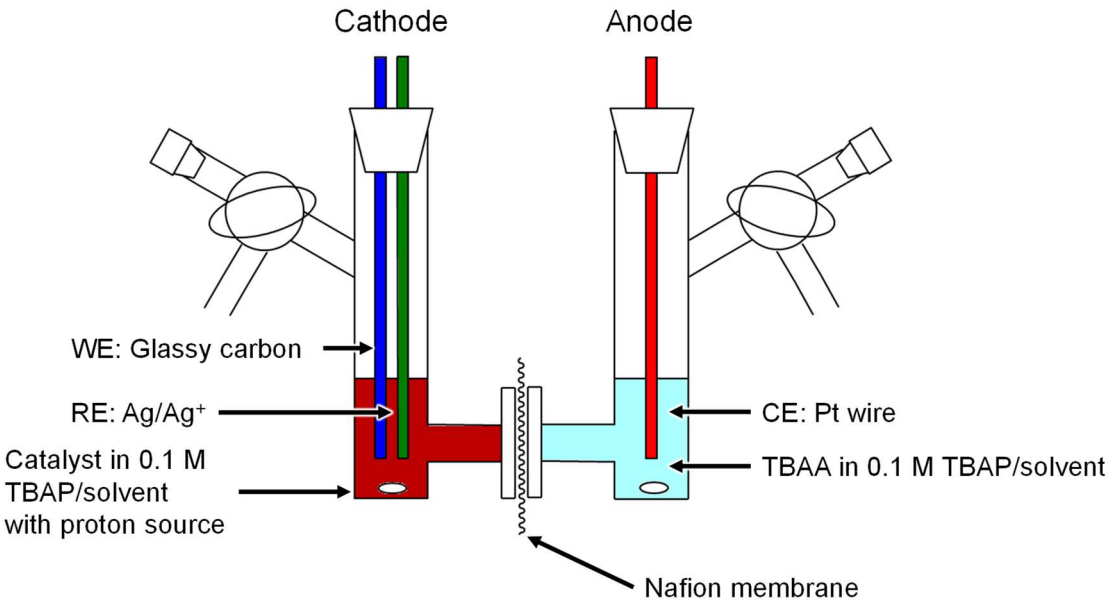

Figure 5. Schematic representation of the custom-designed two compartment cell used in the controlled potential electrolysis experiments.

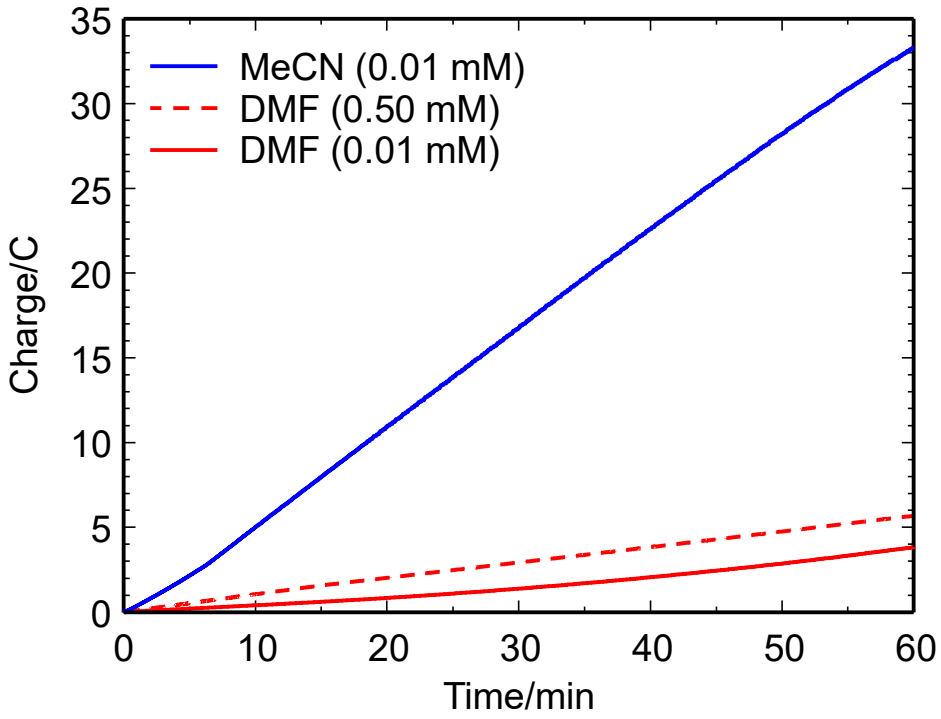

Figure 6. Electrolysis data of **FeTPP-ClO$_4$** (0.01 mM) in MeCN and **FeTPP-Cl** (0.50 and 0.01 mM) in DMF with TBAP (0.1 M) in the presence of 1.0 M TFE under CO_2 at a potential of –2.35 V vs. Fc/Fc^+.

Reaction mechanism

To further verify the effect of MeCN, the reaction mechanism of CO_2 reduction was investigated. Initially, the cyclic voltammograms of **FeTPP-Cl** in DMF and **FeTPP-ClO$_4$** in MeCN were measured in the absence of a proton source under both Ar and CO_2. As shown in Figure 7a, the cyclic voltammograms of **FeTPP-Cl** in DMF displayed almost identical redox peaks at −1.51 V for the Fe(II)/Fe(I) redox couple, indicating the lack of reaction between the Fe(I) species and CO_2 in DMF. In contrast, the cyclic voltammograms of **FeTPP-ClO$_4$** in MeCN exhibited distinct features when measured under different conditions: under Ar, there was a reversible redox wave at −1.43 V attributed to the Fe(II)/Fe(I) redox couple (Figure 7b, red line), while under CO_2, there was an increase in the cathodic current (Figure 7b, blue line). The same phenomenon was also observed in the cyclic voltammograms measured in the MeCN-DMF mixed solvent system (Figure 7c). These results suggest that **FeTPP** reacts with CO_2 as Fe(I) in MeCN. As reported previously,[4–6] in DMF, **FeTPP** undergoes one-electron reduction thrice to form the three-electron-reduced species, **Fe(0)TPP**, which reacts with CO_2 (Scheme 1a, EEEC mechanism). In contrast, my results indicate that the two-electron-reduced species, **Fe(I)TPP**, reacts with CO_2 in MeCN (Scheme 1b, EEC mechanism). The binding constant of CO_2 to **Fe(I)TPP** in MeCN (K_{CO2}) was calculated from the redox potential[20] attributed to Fe(II)/Fe(I) using

$$K_{\mathrm{CO_2}} = \frac{e^{f\Delta E} - 1}{[\mathrm{CO_2}]}, \qquad (2)$$

where $f = F/RT$, $\Delta E = E_{1/2}(CO_2) - E_{1/2}(Ar) = 0.014$ V and $[CO_2] = 0.28$ M, and the K_{CO2} value was determined to be 2.58 M^{-1}.

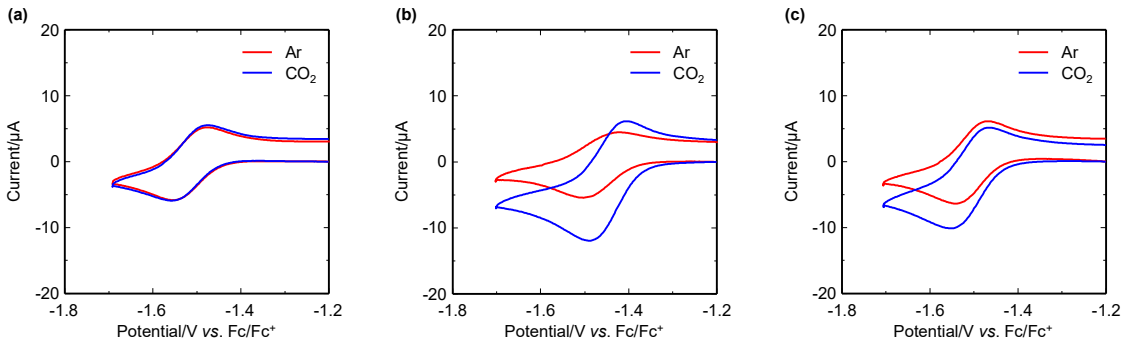

Figure 7. Cyclic voltammograms of (a) **FeTPP-Cl** (0.50 mM) in DMF (b) **FeTPP-ClO$_4$** (0.50 mM) in MeCN (c) **FeTPP-Cl** (0.50 mM) in MeCN/DMF (7:3) with TBAP (0.1 M) under Ar and CO_2 (working electrode: glassy carbon, counter electrode: Pt wire, reference electrode Ag/Ag^+, scan rate 100 mV s^{-1}).

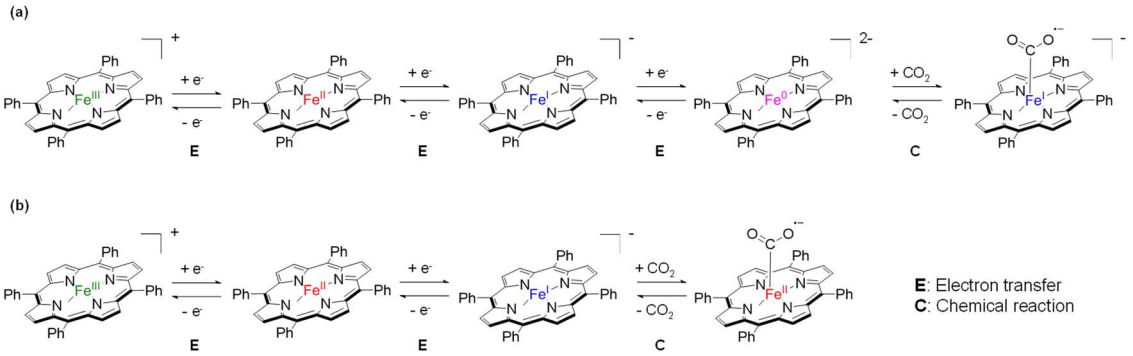

Scheme 1. Proposed mechanism for the formation of the metallocarboxylate intermediate of FeTPP (a) in DMF via the EEEC mechanism (b) in MeCN via the EEC mechanism.

Subsequently, UV-visible absorption spectroelectrochemistry (SEC) measurements were performed to further clarify the reaction of **Fe(I)TPP** with CO_2 in the presence of MeCN. Figure 8a shows the UV-visible absorption spectra of the **Fe(II)TPP** species generated in DMF by applying a potential at E = –1.20 V. The spectra measured under Ar and CO_2 were almost identical, and two Q-bands were observed at 569 and 609 nm. A scan to the negative potential region showed changes in the UV-visible absorption spectra with the occurrence of isosbestic points, and three Q-bands (538, 569, and 609 nm) were observed when E = –1.70 V. Notably, the features of the reduction-induced spectral change measured under Ar and CO_2 were identical (Figures 9a and 9b). These results indicate that **Fe(I)TPP** does not react with CO_2 in DMF, which is consistent with the result of CV. Similarly, **Fe(II)TPP** was also generated by applying a potential at E = –1.20 V in the presence of MeCN,[21] and UV-visible absorption spectra with two Q-bands (569 and 609 nm) were obtained under both Ar and CO_2 (Figure 8b). However, the changes in the UV-visible spectra under Ar and CO_2 upon scanning the potential to the negative potential region were quite different (Figures 8c, 8d, 9c and 9d). While two Q-bands (569 and 609 nm) were observed at E = –1.70 V under Ar, only one Q-band (538 nm) was observed under CO_2. These results strongly indicate that in the presence of MeCN, **Fe(I)TPP** rapidly reacts with CO_2 to form **Fe(II)TPP-$CO_2^{\bullet-}$**. It should be also noted that the comparison of the CVs of **FeTPP-ClO_4** in MeCN and **FeTPP-Cl** in DMF also indicate the interaction of **Fe(I)TPP** with CO_2 in MeCN. Under Ar, the difference in redox potentials attributed to Fe(I)/Fe(0) process is 0.08 V (Figure 10a). On the other hand, under CO_2 in the presence of TFE, the difference in the onset potentials for catalytic current is 0.15 V (Figure 10b), which is significantly larger than that observed under Ar. These results support my proposed catalytic cycle that the reduction of **Fe(II)TPP-$CO_2^{\bullet-}$** triggers the catalysis in MeCN whereas the reduction of **Fe(I)TPP** triggers the catalysis in DMF.

Based on the aforementioned results, a plausible catalytic cycle in MeCN was proposed, as shown in Scheme 2. First, two successive electron transfer from electrode to **FeTPP**, affording **Fe(I)TPP**. Next, CO_2 interacts with **Fe(I)TPP**, which is supported by CV and UV-vis absorption SEC measurements. Then, one electron reduction of the carboxylate intermediate occurs and the reduced carboxylate intermediate takes two

protons.[6] The existence of the resulting iron carbonyl complex is apparent in the backward trace of the catalytic current.[6] Finally, CO is released and the cycle is closed. These processes can be reduced to CECE mechanism.

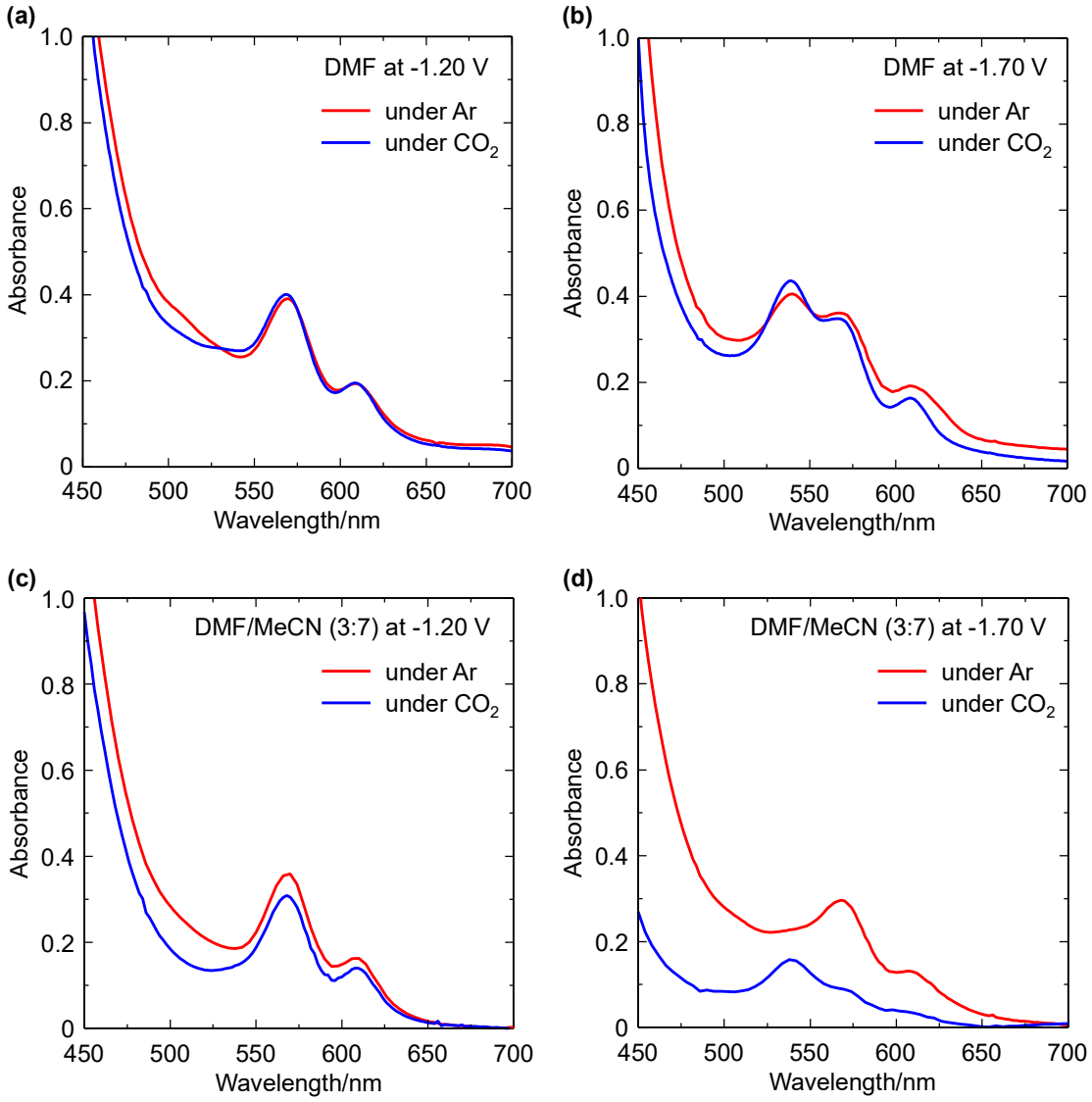

Figure 8. The results of UV-visible absorption SEC measurements of **FeTPP-Cl** (0.50 mM) in DMF with TBAP (0.1 M) under Ar and CO_2 at a potential of (a) –1.20 V and (b) –1.70 V and in DMF/MeCN (3:7) with TBAP (0.1 M) under Ar and CO_2 at a potential of (c) –1.20 V and (d) –1.70 V (working electrode: Pt mesh, counter electrode: Pt wire, reference electrode: Ag/Ag^+. Potential is corrected by Fc/Fc^+).

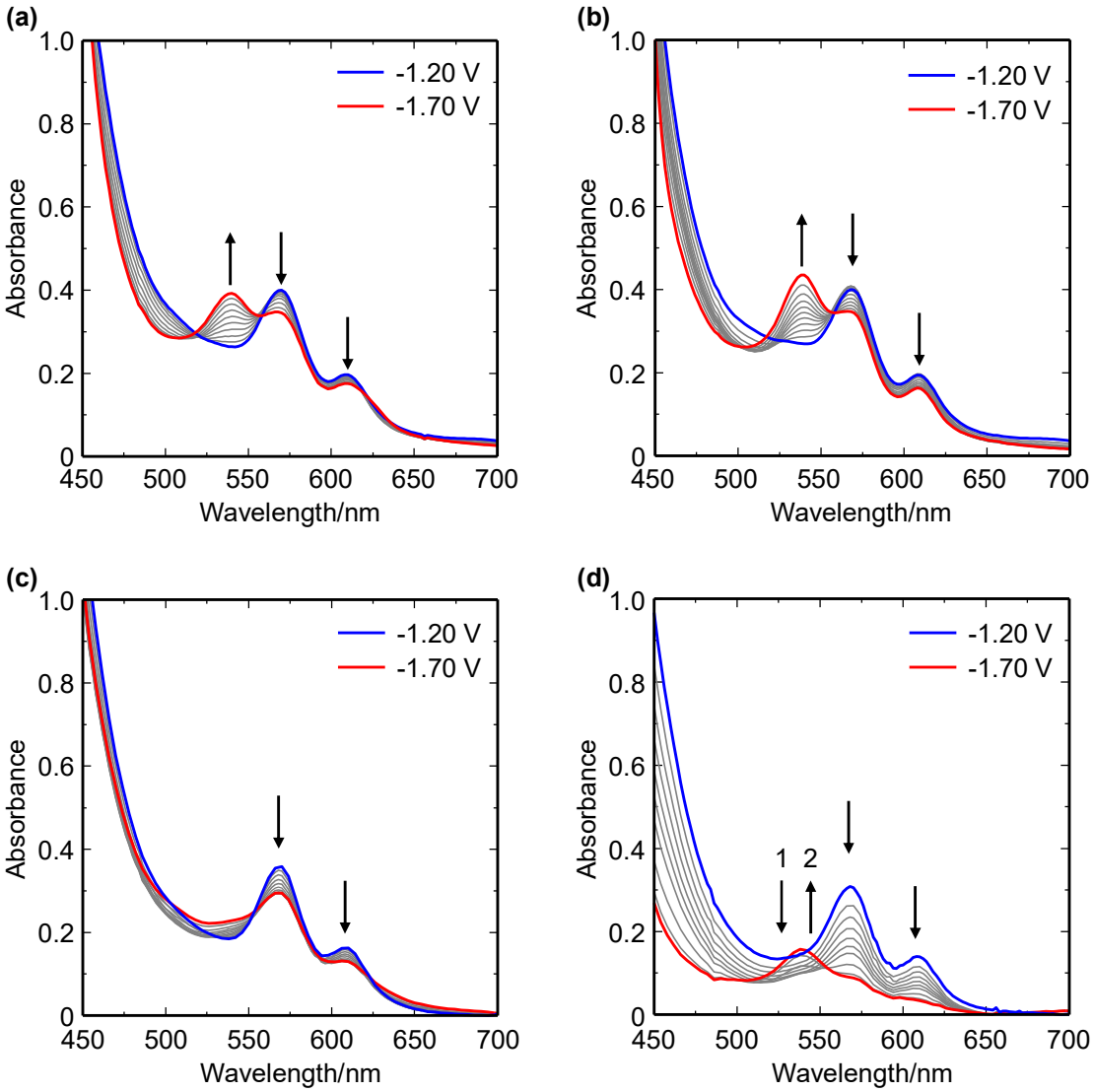

Figure 9. UV-visible absorption SEC measurements of **FeTPP-Cl** (0.50 mM) in DMF with TBAP (0.1 M) under (a) Ar and (b) CO_2 and in DMF/MeCN (3:7) with TBAP (0.1 M) under (c) Ar and (d) CO_2. Working electrode: Pt mesh, counter electrode: Pt wire, reference electrode: Ag/Ag^+. Potential is corrected by Fc/Fc^+.

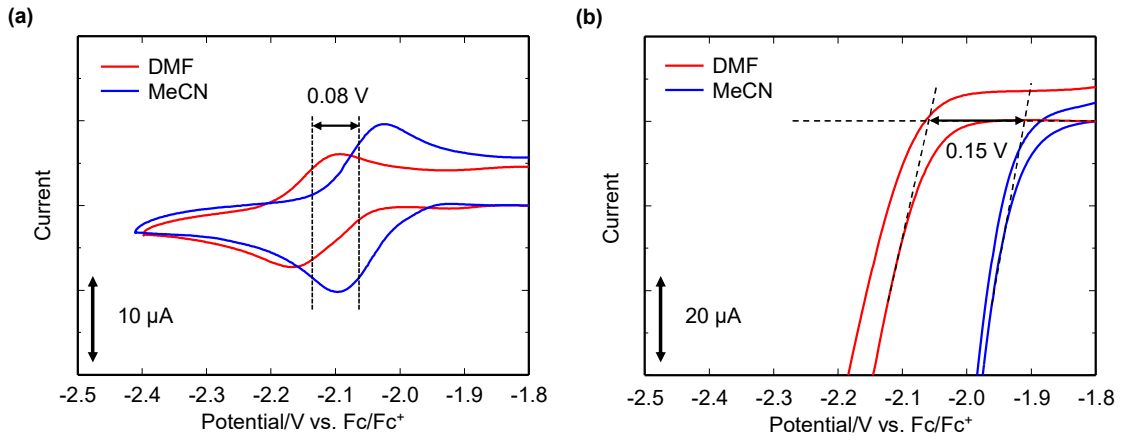

Figure 10. (a) Enlarged cyclic voltammograms focusing on Fe(I)/Fe(0) redox wave of **FeTPP-Cl** (0.50 mM) in DMF and **FeTPP-ClO$_4$** (0.50 mM) in MeCN with TBAP (0.1 M) under Ar (scan rate: 100 mV s^{-1}). (b) Enlarged cyclic voltammograms focusing on the catalytic wave of **FeTPP-Cl** (0.50 mM) in DMF and **FeTPP-ClO$_4$** (0.50 mM) in MeCN with TBAP (0.1 M) in the presence of TFE (0.5 M) under CO_2 (scan rate: 100 mV s^{-1}).

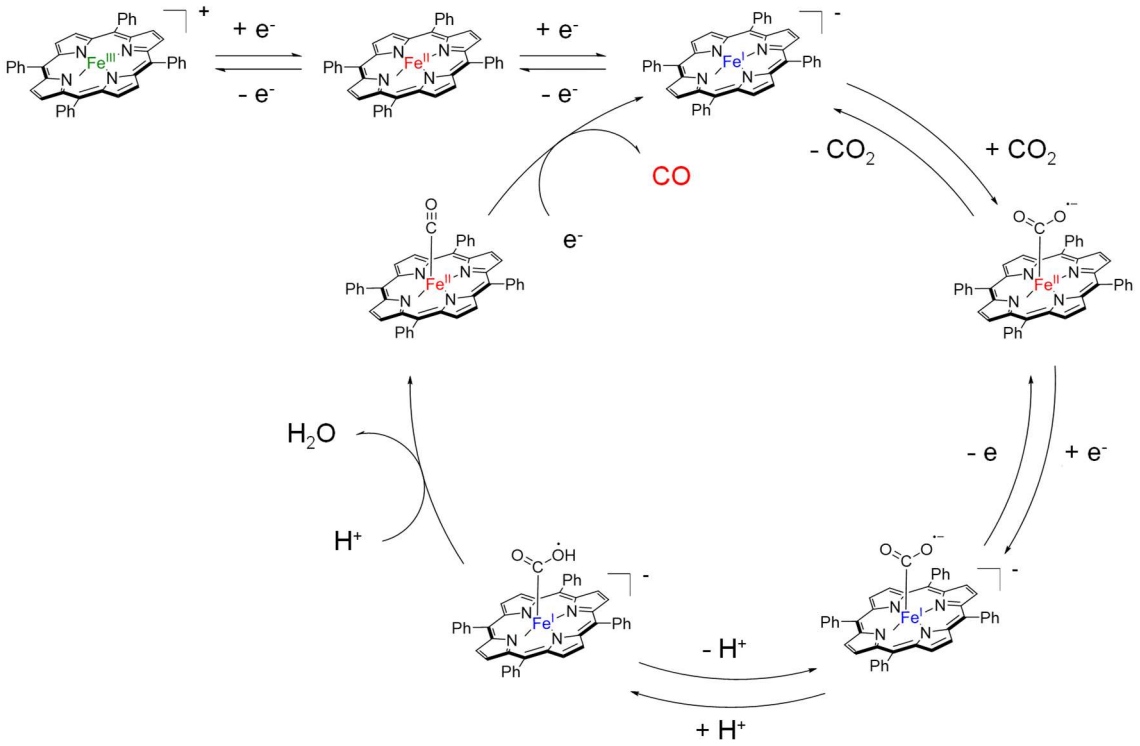

Scheme 2. Proposed catalytic mechanism for electrochemical CO_2 reduction by **FeTPP** in MeCN. In this mechanism, the first step of the catalysis involves the reaction of **Fe(I)TPP**, which is formed by the two-electron reduction of **FeTPP-ClO₄**, with CO_2 to form **Fe(II)TPP-CO₂**$^{\cdot-}$ (C process). **Fe(II)TPP-CO₂**$^{\cdot-}$ is subsequently reduced to **Fe(I)TPP-CO₂**$^{\cdot-}$ (E process). The formed **Fe(I)TPP-CO₂**$^{\cdot-}$ species is then protonated to **Fe(I)TPP-CO₂H**$^{\cdot}$, and further reaction with proton forms **Fe(II)TPP-CO** (C process). Finally, the reduction of **Fe(II)TPP-CO** generates CO and recover the resting **Fe(I)TPP** (E process). Therefore, I have described this catalysis proceeds as CECE mechanism. However, this process can also be described as ECEC mechanism when the reduction of **Fe(II)TPP-CO₂**$^{\cdot-}$ is regarded as the first step of the catalysis.

Turnover frequency calculation

Finally, the kinetic parameters of the catalysts were evaluated to determine the effect of MeCN on the catalytic performance of **FeTPP**. In this study, the TOF values were extracted from the results of both the CV and CPE experiments. Both methods of TOF calculation were established by Savéant *et al*.[22,23] and are frequently used to evaluate the catalytic performance of molecular electrocatalysts for CO_2 reduction.[6–16] Note that I modified the previously reported methods[22,23] (see Appendix A) because the reaction mechanism of my system is distinct from that of conventional catalytic systems (vide supra). The TOF_{max} of **FeTPP-ClO$_4$** in MeCN, calculated from the CV data shown in Appendix A, was 650,000 s^{-1}. This value is significantly higher than that of **FeTPP-Cl** in DMF (3,200 s^{-1}), demonstrating the positive effect of the MeCN medium on catalytic activity. Then, TOF was extracted directly from the results of my CPE experiments, where the products (CO and H_2) were detected and quantified by gas chromatography. The results and conditions are presented in Table 4. For **FeTPP-Cl** in DMF in the presence of 1.0 M TFE, the estimated TOF was 112 s^{-1} at –2.35 V (Table 4, No. 1). On the other hand, for **FeTPP-ClO$_4$** in MeCN in the presence of 1.0 M TFE, the estimated TOF was 1,400,000 s^{-1} (Table 4, No. 2). Furthermore, under the optimized conditions (Table 4, No. 3, and details are described in Appendix B), the TOF reached 7,300,000 s^{-1}, which is approximately 66,300 times higher than that in DMF. The performance of **FeTPP-ClO$_4$** in MeCN is superior to those of current best-in-class molecular catalysts for electrochemical CO_2 reduction[6–16] (Figure 11 and Table 5). The catalytic Tafel plot (Figure 12) also indicates the enhancement of catalytic perforemance in MeCN. It is also worth noting that in most previous works,[6–8,10–15] the TOF_{max} values predicted from CV data were very high (10^3–10^6 s^{-1}), while the actual TOF determined from CPE data was relatively low (~10^2 s^{-1}). In this work, the TOF_{max} predicted from the CV data is consistent with the TOF determined from the CPE data (Table 4), which reflects the excellent performance of my system.

Table 4. Calculated turnover frequencies (TOFs) of iron porphyrin catalysts.

No.	Catalyst	Medium	[cat]/mM	TOF_{max} (CV)/s-1[a]	TOF_{max} (CPE)/s-1[b]
1	**FeTPP-Cl**	0.1 M TBAP/DMF, 1.0 M TFE	0.50	3,200	112
2	**FeTPP-ClO_4**	0.1 M TBAP/MeCN, 1.0 M TFE	0.01	6,50,00	1,400,000[c]
3	**FeTPP-ClO_4**	0.1 M TBAP/MeCN, 1.0 M TFE	0.01		7,300,000[d]

[a] calculated from CV data. [b] calculated from CPE data. [c] using 0.04 M tetra-n-butylammonium acetate (TBAA) in the second compartment. [d] using 0.40 M TBAA in the second compartment.

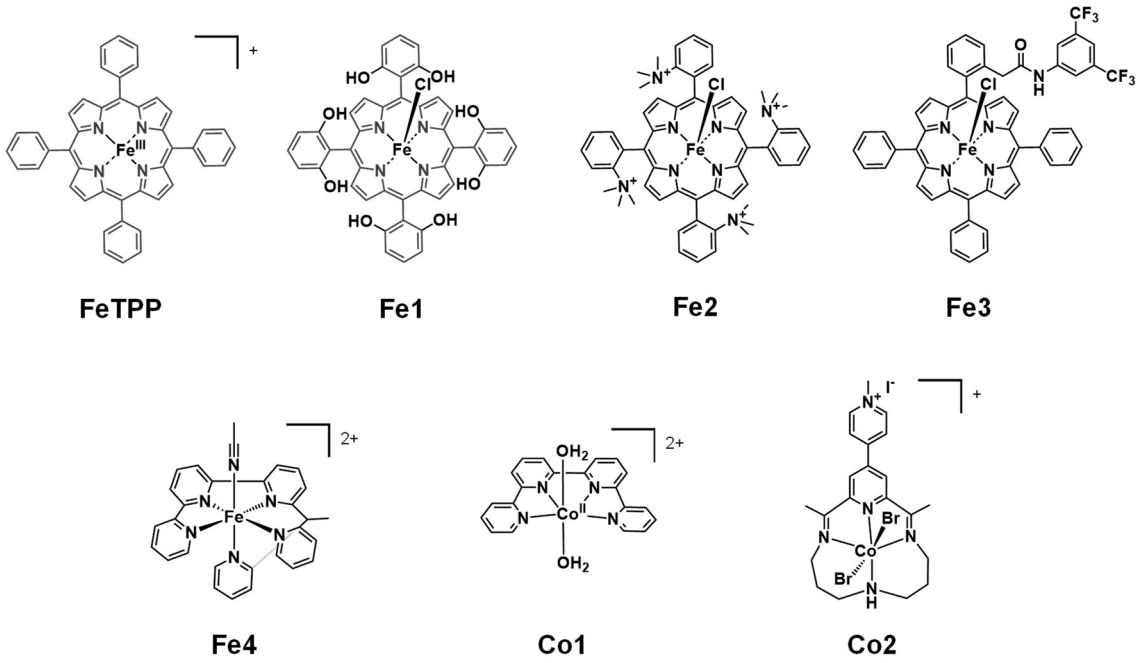

Figure 11. Structures of the catalyst in Table 5.

Table 5. TOF of the recent efficient molecular catalyst for electrochemical CO_2 reduction.

No.	Catalyst	Solvent	[cat]/mM	TOF_{max} (CV)/s^{-1} [a]	TOF (CPE)/s^{-1} [b]	Ref.
1	**FeTPP-Cl**	0.1 M TBAP/DMF, 1.0 M TFE	0.50	3,200	112[c], [e] (–2.35 V *vs*. Fc/Fc^+)	This work
2	**FeTPP-ClO_4**	0.1 M TBAP/MeCN, 1.0 M TFE	0.01	650,000	1,400,000[c], [f] 7,300,000[d], [g] (–2.35 V *vs*. Fc/Fc^+)	This work
3	**Fe1**	0.1 M $TBAPF_6$/DMF, 3.0 M PhOH	1.00	6,300	170 (–1.16 V *vs*. NHE)	7
4	**Fe2**	0.1 M $TBAPF_6$/DMF, 0.1 M H_2O + 3.0 M PhOH	0.50	1,000,000	-	10
5	**Fe3**	0.1 M $TBAPF_6$/DMF, 0.5 M PhOH	0.50	5,500,000	-	8
6	**Fe4**	0.1 M $TBAPF_6$/MeCN, 3.5 M PhOH	1.00	-	900,000 (–1.98 V *vs*. Fc/Fc^+)	16
7	**Co1**	0.1 M $TBAPF_6$/MeCN, 3.0 M PhOH	0.50	33,000	533 (–1.25 V *vs*. SCE)	15
8	**Co2**	0.1 M $TBAPF_6$/MeCN, 11.0 M H_2O	0.30	41,000	160 (–1.95 V *vs*. Fc/Fc^+)	14

[a] calcurated from CV data. [b] calculated from CPE data. [c] using 0.04 M TBAA in the second compartment. [d] using 0.40 M TBAA in the second compartment. [e] TON (TOF × time, 1h) = 4.03×10^5, TON (mol(CO)/mol(catalyst) , 1h) = 11. [f] TON (TOF × time, 1h) = 5.04×10^9, TON (mol(CO)/mol(catalyst) , 1h) = 3,396. [g] TON (TOF × time, 1h) = 2.63×10^{10}, TON (mol(CO)/mol(catalyst) , 1h) = 7,866.

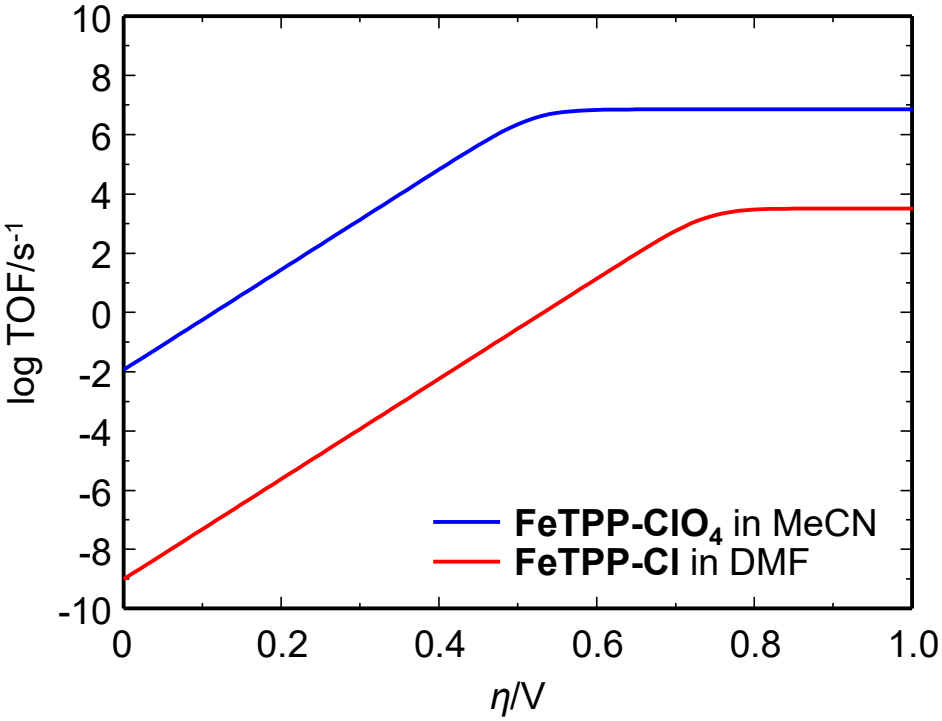

Figure 12. Catalytic Tafel plots for **FeTPP-ClO$_4$** in MeCN (blue) and **FeTPP-Cl** in DMF (red) under CO_2 in the presence of 1.0 M TFE. Overpotential $\eta = E - E_{CO2/CO}$. $E_{CO2/CO}$ = –1.54 V vs. Fc/Fc^+ for MeCN and –1.40 V vs. Fc/Fc^+ for DMF.[12,24]

Conclusion

In conclusion, I have shown a dramatic improvement in the electrochemical CO_2 reduction activity of **FeTPP** simply by changing the reaction medium. The simple counteranion exchange reaction of **FeTPP-Cl** successfully provided a well-soluble complex, **FeTPP-ClO$_4$**. Importantly, the use of MeCN as the solvent significantly enhanced the catalytic activity. The results of the CV and UV-visible absorption SEC measurements suggested that this reaction medium changes the reaction mechanism: in MeCN, CO_2 and FeTPP react at the redox potential of Fe(I)/Fe(II), while in DMF, they react at the redox potential of Fe(0)/Fe(I). It should be noted that although there are a few reports on the high CO_2 reduction activity of several specific iron porphyrin complexes in MeCN,[12,13] the influence of this solvent on the reaction mechanism has not been clarified. Thus, the present study is the first to disclose the origin of the positive effect of MeCN on the catalytic activity of iron porphyrin complexes. Furthermore, under the optimized conditions, **FeTPP-ClO$_4$** in MeCN exhibited the highest TOF (7,300,000 s^{-1}) among the current best-in-class molecular catalysts. The “quick and easy” method presented in this chapter is a new approach for improving the electrochemical CO_2 reduction activity of iron porphyrin complexes.

Experimental section

General procedures

Pyrrole was purchased from Sigma-Aldrich Co., LLC. Benzaldehyde, hydrochloric acid, silver perchlorate monohydrate ($AgClO_4 \cdot H_2O$), and ferrocene were purchased from Wako Pure Chemical Industries, Ltd. Propanoic acid and iron(III) chloride were purchased from Kishida Chemical Co., LLC. Methanol, chloroform ($CHCl_3$), *N*, *N*-dimethylformamide (DMF), hexane, tetrahydrofuran (THF), and acetonitrile (MeCN) were purchased from Kanto Chemical Co., Inc. Tetra-*n*-butylammonium perchlorate (TBAP), tetra-*n*-butylammonium acetate (TBAA), and 2,2,2-trifluoroethanol were purchased from Tokyo Chemical Industry Co., Ltd. Chloroform-d_1 was purchased from Cambridge Isotopes, Inc. All solvents and reagents are of the highest quality available and used as received except for TBAP. TBAP was recrystallized from absolute ethanol. ^{1}H-NMR spectra were collected at room temperature on a JEOL JNM-ECS400 spectrometer. Elemental analysis was performed on a J-SCIENCE LAB MICRO CORDER JM10 elemental analyzer. UV-visible absorption spectra were recorded on a UV-Vis Agilent Cary8454 spectrophotometer.

Synthesis

Synthesis of meso-tetraphenylporphyrin (H_2TPP)

H_2TPP was prepared as previously described.[25] Pyrrole (1.7 mL, 25 mmol) and benzaldehyde (2.6 mL, 25 mmol) were dissolved in propanoic acid (50 mL), then refluxed for 45 minutes and cooled to room temperature. The resulting mixture was filtered and washed with methanol. Recrystallization from $CHCl_3$/methanol gave a purple solid (785 mg, yield 20%). ^{1}H-NMR (400 MHz, $CDCl_3$): d = 8.82 (s, 8H), 8.19-8.21 (m, 8H), 7.71-7.78 (m, 12H), −2.80 (s, 2H) ppm. Elemental analysis Calcd. for $C_{44}H_{30.5}N_4O_{0.25}$ (H_2TPP· 0.25 H_2O): C, 85.34%; H, 4.96%; N, 9.05%. Found: C, 85.24%, H, 4.68%; N, 9.08%.

Synthesis of meso-tetraphenylporphyrin iron(III) chloride (FeTPP-Cl)

FeTPP-Cl was prepared by the modification of a previous report.[26] To a solution of **H_2TPP** (200 mg, 0.32 mmol) in DMF (10 mL), a 10 mL DMF solution of $FeCl_3$ (519 mg, 3.2 mmol) was added at room temperature. The mixture was heated at 200 ˚C for 1 hour by a microwave reactor. Diluted HCl (1 M, 50 mL) was added to the resulting solution. Precipitate was collected by filtration and washed with 1 M HCl. Recrystallization from

$CHCl_3$/hexane gave a purple solid (191 mg, yield 85%). Elemental analysis Calcd. for $C_{44}H_{28}ClFeN_4$ (**FeTPP-Cl**): C, 75.06%; H, 4.01%; N, 7.96%. Found: C, 74.98%; H, 4.08%; N, 8.01%.

Synthesis of meso-tetraphenylporphyrin iron(III) perchlorate (FeTPP-ClO_4)

FeTPP-ClO_4 was prepared by the modification of a previous report.[17] To a solution of **FeTPP-Cl** (50 mg, 0.071 mmol) in tetrahydrofuran THF (14 mL), an MeCN (1 mL) solution of $AgClO_4 \cdot H_2O$ (14.7 mg, 0.071 mmol) was added at room temperature. The mixture was stirred at room temperature for 1 hour. Precipitate (AgCl) was removed and the residual THF solution was collected. Recrystallization from THF/heptane gave a purple solid (42 mg, yield 77%). Elemental analysis Calcd. for $C_{49}H_{38}ClFeN_4O_{5.25}$ (**FeTPP-ClO_4**·1.25 THF): C, 68.58%; H, 4.46%; N, 6.53%. Found: C, 68.30%; H, 4.63%; N, 6.72%.

Electrochemistry

Electrochemical experiments were performed at room temperature on a BAS ALS Model 650DKMP electrochemical analyzer or a Bio-Logic-Science Instruments potentiostat. Cyclic voltammetry (CV) measurements were performed by using a one-compartment cell with a three-electrode configuration, which consisted of a glassy carbon disk (diameter 3 mm, BAS Inc.), platinum wire, and Ag/Ag^+ electrode (Ag/0.01 M $AgNO_3$) as the working, auxiliary, and reference electrodes, respectively. The glassy carbon disc working electrode was polished using 0.05 μm alumina paste (BAS Inc.) and washing with purified H_2O prior to each measurement. Ferrocene was used as an internal standard and all potentials are referenced to the ferrocenium/ferrocene (Fc/Fc^+) couple at 0 V.

UV-visible spectroelectrochemistry (UV-SEC)

Spectroelectrolysis was performed using a BAS Inc. spectroelectrochemical quartz glass cell (light path length 1 mm). A piece of 80 mesh platinum gauze, platinum wire, and Ag/Ag^+ electrode (Ag/0.01 M $AgNO_3$) were used as the working, auxiliary, and reference electrodes respectively. All solution were purged with Ar or saturated with CO_2 before UV spectra were taken. The temperature during the measurement is controlled at 25 ˚C. Ferrocene was used as an internal standard and all potentials are referenced to the Fc/Fc^+ couple at 0 V.

Controlled potential electrolysis (CPE)

CPE was performed in a gas-tight two-compartment electrochemical cell, where the first compartment held the carbon plate working electrode (1.2 cm^2 surface area) and Ag/Ag^+ reference electrode (Ag/0.01 M $AgNO_3$) in 5 ml of 0.1 M TBAP/MeCN with catalyst and proton source, while the second compartment held the Pt auxiliary electrode in 5 ml of 0.1 M TBAP/MeCN containing TBAA (0.2 M) as sacrificial oxidant. The two compartments were separated by a Nafion® membrane. The solution was purged vigorously with CO_2 for 30 mins prior to electrolysis. The electrolysis experiment was performed for 1 h under constant stirring. The amount of CO and H_2 produced was quantified from an analysis of the headspace with a Shimadzu GC-8A with TCD detector equipped with a capillary column with Molecular Sieve 13X-S 60/80. Calibration curves were made by sampling known amounts of H_2 and CO.

X-ray crystallography

Single crystal X-ray diffraction data were collected on a Synergy Custom system CCD Plate equipped with confocal monochromated Mo-Kα radiation (λ = 0.71069 Å) coated with Paratone-N (Hampton Research Corp., Aliso Viejo, CA, USA). Data was processed using CrysAlisPro system software.[27] The structure was solved by dual-space algorithm using SHELXT program[28] through the Olex2 interface.[29] All non-hydrogen atoms were refined anisotropically using a least-squares method, and hydrogen atoms were fixed at calculated positions and refined using a riding model. SHELXL−2014/7 was used for structure refinement.[30] Full-matrix least-squares refinements on F^2 based on unique reflections with unweighted and weighted agreement factors of $R = \Sigma||F_o| - |F_c||/\Sigma|F_o|$ ($I > 2.00\ \sigma(I)$) and $wR = [\Sigma w(F_o^2 - F_c^2)^2/\Sigma w(F_o^2)^2]^{1/2}$ were performed. Mercury 4.0.0 was used for visualization and analysis of the structure. Crystallographic data have been deposited with Cambridge Crystallographic Data Centre: Deposition numbers CCDC 2110898 for **CuTPFP**. Copies of the data can be obtained free of charge via www.ccdc.cam.ac.uk/data_request/cif.

Appendix A: TOF calculation

The TOF values of my catalyst were evaluated based on following Eq.(5) and Eq.(17) for CV measurement, and Eq.(18) and Eq.(20) for CPE experiments, respectively. This is because in electrochemical condition, only small quantity of the catalyst close to the surface of the working electrode is catalytically active. These types of equations are often used for the evaluation of TOF values for molecule-based catalysts for CO_2 reduction, which reflects the inherent activity of the catalysts. In the following, definition and derivation of the equations for TOF calculation are described.

A1. TOF_{max} calculation by CV measuremensts

In general, TOF_{max} value of the electrochemical CO_2 reduction is predicted by CV measurements using

$$\frac{I_{\mathrm{PL}}}{I_{\mathrm{P}}} = 2.24n'\sqrt{\frac{k_{\mathrm{obs}}}{fv}} \tag{3}$$

or

$$\frac{I_{\mathrm{cat}}}{I_{\mathrm{P}}} = \frac{2.24}{1+\exp[f(E-E^0_{\mathrm{cat}})]}\sqrt{\frac{k_{\mathrm{obs}}}{fv}}, \tag{4}$$

and

$$\mathrm{TOF}_{\mathrm{max}} = k_{\mathrm{obs}} \tag{5}$$

where I_{PL} is the limiting catalytic current, I_P (A) is the peak current at $E = E_{cat}^0$ in the absence of substrate (see Eq.(1) in the maintext), k_{obs} (s^{-1}) is the observed rate constant, n' is the number of electrons transferred per CO_2 per catalyst ($n' = 2$), $f = F/RT$ (V^{-1}), v ($V\ s^{-1}$) is the scan rate, I_{cat} (A) is the catalytic current in the Nernstian behavior at E (V), and E_{cat}^0 (V) is the redox potential of the catalyst in the absence of substrate. In particular, prediction of TOF_{max} by Eq.(4) is known as foot of the wave analysis (FOWA).[6,22] Although these equations are very useful, they are applicable only when the catalytic cycle is EC mechanism or reasonable approximations are satisfied.[23] As shown in Scheme 2, the catalytic cycle for electrochemical CO_2 reduction by **FeTPP** in MeCN is reduced to CECE mechanism. Therefore, neither Eq.(3) nor Eq.(4) can be applied to my system.

Here, I derived an analytical representation of the catalytic current I_{cat} for CECE mechanism and predicted TOF_{max} using FOWA for CECE mechanism with some reasonable approximations. The reaction mechanism shown in Scheme 1 is simplified as

$$\mathrm{I} + \mathrm{S} \rightarrow \mathrm{J},\ k_1, \tag{6}$$

$$\mathrm{J} + \mathrm{e}^- \rightleftharpoons \mathrm{K}, E^0_{\mathrm{J/K}}, k_{\mathrm{ET1}}, k_{\mathrm{ET2}}, \tag{7}$$

$$\mathrm{K} + \mathrm{Z} \rightarrow \mathrm{L} + \mathrm{P},\ k_2, \tag{8}$$

$$\mathrm{L} + \mathrm{e}^- \rightleftharpoons \mathrm{I} + \mathrm{Q}, E^0_{\mathrm{L/I}}, k_{\mathrm{ET3}}, k_{\mathrm{ET4}}, \tag{9}$$

where I = **Fe(I)TPP**, J = **Fe(II)TPP**-CO_2, K = **Fe(I)TPP**-CO_2, L = **Fe(II)TPP**-CO, S = CO_2, Z = $2H^+$, P = H_2O and Q = CO, respectively. k_1 and k_2 are rate constants for chemical reaction and k_{ET1}, k_{ET2}, k_{ET3} and k_{ET4} are rate constants for redox reaction and they are represented by Butler-Volmer equation. $E_{J/K}{}^0$ and $E_{L/I}{}^0$ are formal potentials. In Nernstian behavior, all terms containing k_{ETi} ($i = 1 \sim 4$) vanish and I_{cat} for CECE mechanism is given by

$$I_{\mathrm{cat}} = \frac{2FAC^*_{\mathrm{cat}}\sqrt{D_{\mathrm{cat}}}}{\frac{1}{\sqrt{k_1 C^*_{\mathrm{S}}}}\{1+\exp[f(E-E^0_{\mathrm{J/K}})]\} + \frac{1}{\sqrt{k_2 C^*_{\mathrm{Z}}}}\{1+\exp[f(E-E^0_{\mathrm{L/I}})]\}}, \tag{10}$$

where $C_S{}^*$ and $C_Z{}^*$ are the bulk concentration of CO_2 and proton source, respectively, and they are constant.

When $E \ll E_{J/K}{}^0$ and $E \ll E_{L/I}{}^0$, the limiting current I_{PL} is represented as

$$I_{\mathrm{PL}} \simeq \frac{2FAC^*_{\mathrm{cat}}\sqrt{D_{\mathrm{cat}}}}{\frac{1}{\sqrt{k_1 C^*_{\mathrm{S}}}} + \frac{1}{\sqrt{k_2 C^*_{\mathrm{Z}}}}}. \tag{11}$$

According to the literature, the second electron transfer is easier than the first.[23] Therefore, $E_{J/K}{}^0 \ll E_{L/I}{}^0$ is satisfied and at sufficient negative potential, $\exp[f(E-E^0_{L/I})] \simeq 0$, which leads to

$$I_{\mathrm{cat}} \simeq \frac{I_{\mathrm{PL}}}{1+\exp[f(E-E^0_{1/2})]}, \tag{12}$$

where

$$E_{1/2} = E^0_{\mathrm{J/K}} + \frac{1}{f}\ln\left(1+\sqrt{\frac{k_1 C^*_{\mathrm{S}}}{k_2 C^*_{\mathrm{Z}}}}\right). \tag{13}$$

Although Eq.(12) is derived for CECE mechanism, it is the same form as I_{cat} for ECEC

mechanism.[23]

I can further introduce reasonable approximation to Eq.(13). When CO_2 binding is the rate determining step ($k_1C_S^* \ll k_2C_Z^*$), Eq.(12) is simplified as

$$I_{\mathrm{cat}} = \frac{2FAC_{\mathrm{cat}}^* \sqrt{k_1 C_{\mathrm{S}}^* D_{\mathrm{cat}}}}{1 + \exp[f(E - E_{\mathrm{J/K}}^0)]}. \tag{14}$$

On the other hand, when proton transfer is the rate determining step ($k_2C_Z^* \ll k_1C_S^*$), Eq.(12) is simplified as

$$I_{\mathrm{cat}} = 2FAC_{\mathrm{cat}}^* \sqrt{k_2 C_{\mathrm{Z}}^* D_{\mathrm{cat}}}. \tag{15}$$

Here, I performed CV measurements of **FeTPP-ClO4** in 0.1 M TBAP/MeCN under CO_2 in the presence of 1.0 M TFE or 1.0 M TFE-d_3 and determined whether proton transfer involves the rate determining step or not. As shown in Figure A1, the voltammogram in the presence of TFE-d_3 is almost the same as that in the presence of TFE. These results suggest that the reaction does not influenced by H/D isotopic effect and proton transfer is not the rate determining step. Therefore, I chose Eq.(14) as I_{cat} for my system. Combination of Eq.(1) and Eq.(14) leads to

$$\frac{I_{\mathrm{cat}}}{I_{\mathrm{P}}} = \frac{4.48}{1 + \exp[f(E - E_{\mathrm{J/K}}^0)]} \sqrt{\frac{k_1 C_{\mathrm{S}}^*}{fv}}, \tag{16}$$

and

$$\mathrm{TOF}_{\mathrm{max}} = k_1 C_{\mathrm{S}}^*. \tag{17}$$

FOWA of **FeTPP** in MeCN using Eq.(16) is shown in Figure A2a. Here, in order to obtain an accurate redox potential of J/K (**Fe(II)TPP**-CO_2/**Fe(I)TPP**-CO_2) and avoid an over estimation of TOF_{max}, $E_{J/K}{}^0$ is determined by square wave voltammetry measurement (–2.032 V) under CO_2 (Figure A3, vertical dashed line), which is higher than that determined under Ar (–2.062 V). FOWA of **FeTPP** in DMF using Eq.(4) is also shown in Figure A2b.

Although TOF_{max} was rigorously defined and appropriate approximations were applied, FOWA in Figure A2a underestimates TOF_{max}. In Figure A2a, the linear region of the FOW is small (I_{cat}/I_p is less than 1), which makes difficult to determine the accurate TOF_{max} by this method. Therefore, I show the TOF_{max} of **FeTPP-ClO4** in MeCN as a

reference value (Table 5). In order to determine TOF more accurately, I directly extracted kinetic data from CPE experiments (see the next section).

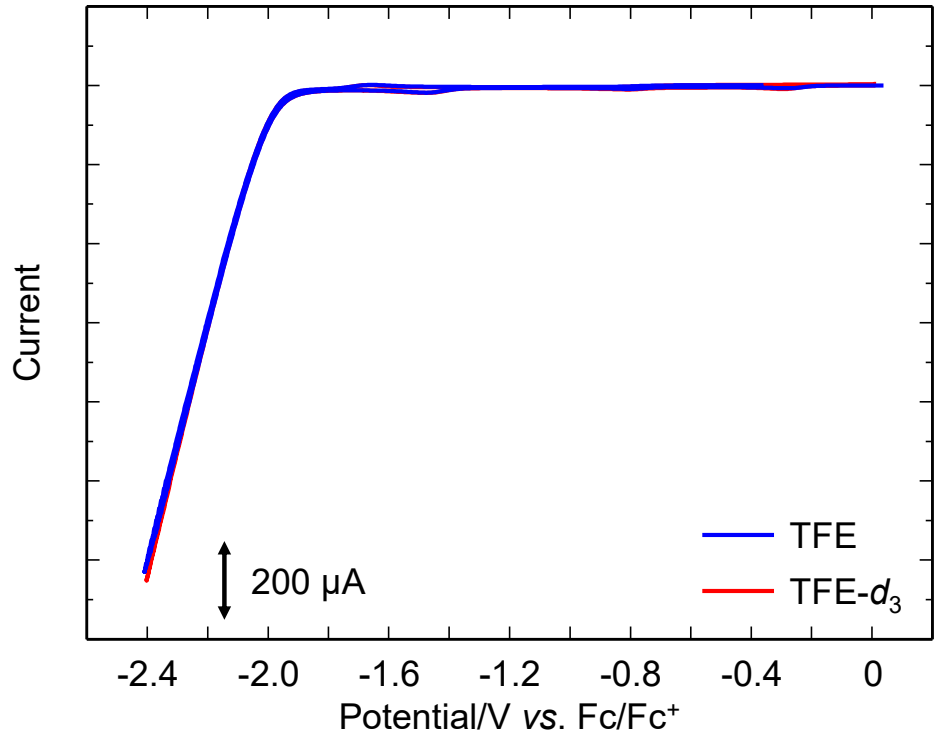

Figure A1. Cyclic voltammograms of **FeTPP-ClO$_4$**. Measurements were performed in MeCN solution of **FeTPP-ClO$_4$** (0.50 mM) with TBAP (0.1 M) as a supporting electrolyte under CO_2 atmosphere in the presence of 1.0 M TFE (blue) and 1.0 M TFE-d_3 (red). Electrodes: working, GC; auxiliary, Pt; reference, Ag/Ag$^+$. Scan rate: 100 mV/s.

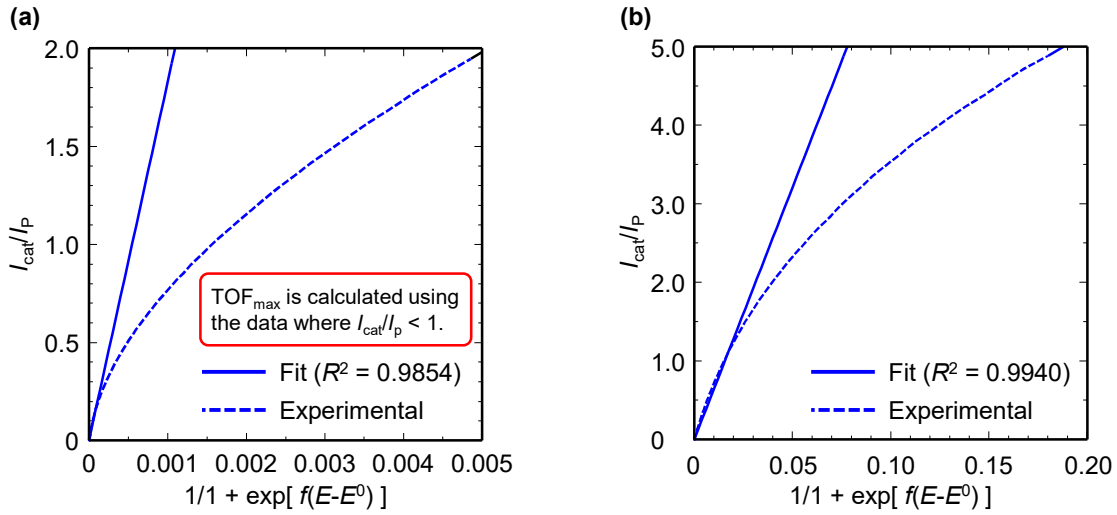

Figure A2. A plot of the ratio of I_{cat} to I_P as a function of the inverse of potential. Measurements were performed in (a) MeCN solution of **FeTPP-ClO$_4$** (0.50 mM) and (b) DMF solution of **FeTPP-Cl** (0.50 mM) with TBAP (0.1 M) as the supporting electrolyte under Ar atmosphere (for I_P) or under CO_2 atmosphere in the presence of 1.0 M TFE (for I_{cat}) (working electrodes: glassy carbon, counter electrode: Pt wire, reference electrode: Ag/Ag^+, scan rate: 100 mV s^{-1}).

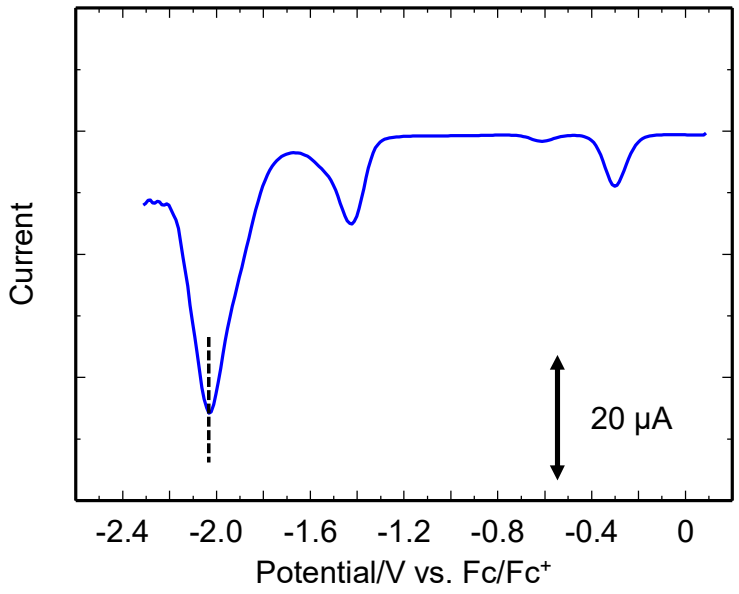

Figure A3. Square wave voltammograms of **FeTPP-ClO$_4$** (0.50 mM) in MeCN with TBAP (0.1 M) as a supporting electrolyte under CO_2 atmosphere. Electrodes: working, GC; auxiliary, Pt; reference, Ag/Ag^+.

A2. TOF calculation by CPE experiments

TOF value of the electrochemical CO_2 reduction by **FeTPP** in MeCN is determined by CPE experiment using

$$\mathrm{TOF} = \frac{k_1 C_{\mathrm{S}}^*}{1 + \exp[f(E - E_{\mathrm{J/K}}^0)]}. \tag{18}$$

Eq.(18) is derived by introducing reasonable approximations described in Appendix A1. $k_1 C_S^*$ is evaluated by Eq.(14), where I_{cat} is the average catalytic current during electrolysis and it is estimated from the charge-time profile shown in Figure B1 in the Appendix B. Here, A = 1.2 cm^2, D_{cat} = 1.07×10^{-5} cm^2 s^{-1} and $E_{J/K}^0$ = –2.032 V.

TOF value of the electrochemical CO_2 reduction by **FeTPP** in DMF is also determined by CPE experiment using

$$I_{\mathrm{cat}} = \frac{FAC_{\mathrm{cat}}^* \sqrt{k_{\mathrm{obs}} D_{\mathrm{cat}}}}{1 + \exp[f(E - E_{\mathrm{cat}}^0)]}, \tag{19}$$

and

$$\mathrm{TOF} = \frac{k_{\mathrm{obs}}}{1 + \exp[f(E - E_{\mathrm{J/K}}^0)]}, \tag{20}$$

where A = 1.2 cm^2, D_{cat} = 5.60×10^{-6} cm^2 s^{-1} and E_{cat}^0 = –2.140 V.

Appendix B: CPE experiments in various conditions

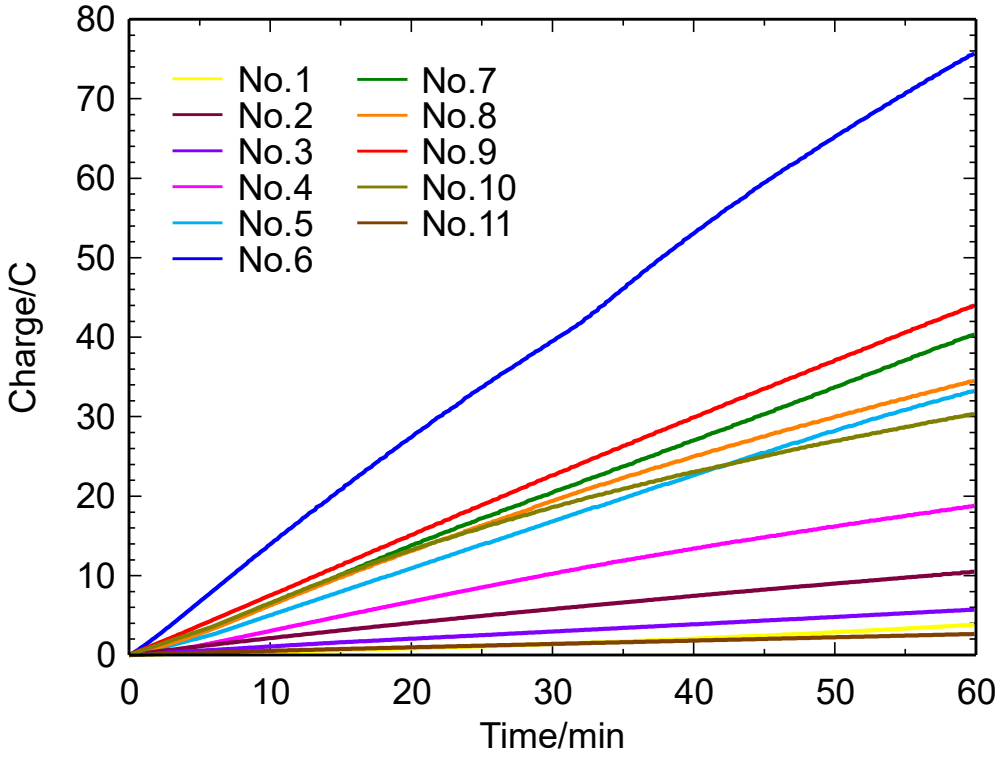

Figure B1. The results of CPE experiments of **FeTPP-ClO$_4$** and **FeTPP-Cl** at –2.35 V (*vs*. Fc/Fc$^+$) for 1 h. Details of the experimental condition are summarized in Table S4. Working electrode, glassy carbon (1.2 cm^2); counter electrode, Pt wire; reference electrode, Ag/Ag$^+$.

Table B1. Summary of the CPE experiments.

No.	Catalyst	Solvent	[cat]/mM	Total charge/C	Faradaic efficiency/%		
					CO	H_2	Total
1	**FeTPP-Cl**	0.1 M TBAP/DMF, 1.0 M TFE[a]	0.01	3.9	22.6	2.5	25.1
2	**FeTPP-Cl**	0.1 M TBAP/DMF, 0.5 M TFE[a]	0.50	10.5	96.1	trace	96.1
3	**FeTPP-Cl**	0.1 M TBAP/DMF, 1.0 M TFE[a]	0.50	5.7	91.5	trace	91.5
4	**FeTPP-ClO_4**	0.1 M TBAP/MeCN, 0.5 M TFE[a]	0.01	18.8	97.0	1.0	98.0
5	**FeTPP-ClO_4**	0.1 M TBAP/MeCN, 1.0 M TFE[a]	0.01	33.3	98.4	1.5	99.9
6	**FeTPP-ClO_4**	0.1 M TBAP/MeCN, 1.0 M TFE[b]	0.01	75.9	97.3	1.7	99.0
7	**FeTPP-ClO_4**	0.1 M TBAP/MeCN, 2.0 M TFE[a]	0.01	40.4	83.7	13.6	97.3
8	**FeTPP-ClO_4**	0.1 M TBAP/MeCN, 0.5 M PhOH[a]	0.01	34.6	86.7	8.8	95.5
9	**FeTPP-ClO_4**	0.1 M TBAP/MeCN, 3.0 M PhOH[a]	0.01	44.1	3.9	50.5	54.4
10	**FeTPP-ClO_4**	0.1 M TBAP/MeCN, 0.5 M TFE[a]	0.50	30.4	98.7	0.1	98.8
11	**FeTPP-ClO_4**	0.1 M TBAP/DMF, 1.0 M TFE[a]	0.01	2.6	21.9	17.4	39.3

[a] using 0.04 M TBAA in the second compartment. [b] using 0.40 M TBAA in the second compartment.

References

[1] A. M. Appel, J. E. Bercaw, A. B. Bocarsly, H. Dobbek, D. L. DuBois, M. Dupuis, J. G. Ferry, E. Fujita, R. Hille, P. J. A. Kenis, C. A. Kerfeld, R. H. Morris, C. H. F. Peden, A. R. Portis, S. W. Ragsdale, T. B. Rauchfuss, J. N. H. Reek, L. C. Seefeldt, R. K. Thauer, G. L. Waldrop, *Chem*. *Rev*. **2013**, *113*, 6621.

[2] R. Francke, B. Schille, M. Roemelt, *Chem*. *Rev*. **2018**, *118*, 4631.

[3] Ē. Boutin, L. Merakeb, B. Ma, B. Boudy, M. Wang, J. Bonin, E. Anxolabéhère-Mallart, M. Robert, *Chem*. *Soc*. *Rev*. **2020**, *49*, 5772.

[4] I. Bhugun, D. Lexa, J. M. Savéant, *J*. *Phys*. *Chem*. **1996**, *100*, 19981.

[5] I. Bhugun, D. Lexa, J. M. Savéant, *J*. *Am*. *Chem*. *Soc*. **1996**, *118*, 1769.

[6] C. Costentin, S. Drouet, G. Passard, M. Robert, J. M. Savéant, *J*. *Am*. *Chem*. *Soc*. **2013**, *135*, 9023.

[7] C. Costentin, G. Passard, M. Robert, J. M. Savéant, *J*. *Am*. *Chem*. *Soc*. **2014**, *136*, 11821.

[8] E. M. Nichols, J. S. Derrick, S. K. Nistanaki, P. T. Smith, C. J. Chang, *Chem*. *Sci*. **2018**, *9*, 2952.

[9] Y. Okabe, S. K. Lee, M. Kondo, S. Masaoka, *J*. *Biol*. *Inorg*. *Chem*. **2017**, *22*, 713.

[10] I. Azcarate, C. Costentin, M. Robert, J. M. Savéant, *J*. *Am*. *Chem*. *Soc*. **2016**, *138*, 16639.

[11] E. A. Mohamed, Z. N. Zahran, Y. Naruta, *Chem*. *Commun*. **2015**, *51*, 16900.

[12] S. Sinha, J. J. Warren, *Inorg*. *Chem*. **2018**, *57*, 12650.

[13] B. Zhao, H. Lei, N. Wang, G. Xu, W. Zhang, *Chem*. *Eur*. *J*. **2020**, *26*, 4007.

[14] W. Nie, D. E. Tarnopol, C. C. L. McCrory, *J*. *Am*. *Chem*. *Soc*. **2021**, *143*, 3764.

[15] C. Cometto, L. Chen, P. K. Lo, Z. Guo, K. C. Lau, E. Anxolabéhère-Mallart, C. Fave, T. C. Lau, M. Robert, *ACS Catal*. **2018**, *8*, 3411.

[16] J. S. Derrick, M. Loipersberger, R. Chatterjee, D. A. Iovan, P. T. Smith, K. Chalarawet, J. Yano, J. R. Long, M. Head-Gordon, C. J. Chang, *J*. *Am*. *Chem*. *Soc*. **2020**, *142*, 20489.

[17] C. A. Reed, T. Mashiko, S. P. Bentley, M. E. Kastner, W. R. Scheidt, K. Spartalian, G. Lang, *J*. *Am*. *Chem*. *Soc*. **1979**, *101*, 2948.

[18] L. A. Bottomley, K. M. Kadish, *Inorg*. *Chem*. **1981**, *20*, 1348. *Phys.* **2014**, *16* (5),

1883–1893.

[19] C. Costentin, G. Passard, M. Robert, J.-M. Savéant, *Proc. Natl. Acad. Sci. USA*, **2014**, *111*, 14990.

[20] R. R. Gagné, J. L. Allison, D. M. Ingle, *Inorg. Chem*. **1979**, *18*, 2767.

[21] The measurements of **FeTPP-ClO$_4$** were omitted because the difference in the counter anion affects the UV–vis absorption spectrum, which makes comparison difficult.

[22] C. Costentin, S. Drouet, M. Robert, J. M. Savéant, *J. Am. Chem. Soc*. **2012**, *134*, 11235.

[23] C. Costentin, J. M. Savéant, *ChemElectroChem* **2014**, *1*, 1226.

[24] M. L. Pegis, J. A. S. Roberts, D. J. Wasylenko, E. A. Mader, A. M. Appel, J. M. Mayer, *Inorg. Chem*. **2015**, *54*, 11883.

[25] A. D. Alder, F. R. Long, W. Shergalis, *J. Am. Chem. Soc*. **1964**, *86*, 3145.

[26] S. L. Rebelo, A. M. N. Silva, C. J. Medforth, C. Freire, *Molecules* **2016**, *21*, 481.

[27] CrysAlisPro, Oxford Diffraction Ltd., Version 1.171.39.46.

[28] G. M. Sheldrick, *Acta Cryst*. **2015**, A71, 3.

[29] O. V. Dolomanov, L. J. Bourhis, R. J. Gildea, J. A. K. Howard, H. Puschmann, *J. Appl. Crystallogr*. **2009**, *42*, 339.

[30] G. M. Sheldrick, *Acta Cryst*. **2015**, A71, 3.

Chapter 3

Highly Active Copper-based Molecular Catalyst for Electrochemical CO_2 Reduction

Introduction

The catalytic reduction of CO_2 in fuels or commodity chemicals is one of the most important technologies for constructing a renewable energy system.[1] For this purpose, extensive efforts have been made to develop catalytic systems for the reduction of CO_2.[2-27] Among them, homogeneous molecular catalysts have an advantage in catalyst design at the molecular level based on the detailed mechanistic study. To date, many examples of metal-complex-based homogeneous catalysts have been reported.[2-26] In particular, earth-abundant first-row transition metals have attracted attention as a constituent element of the catalyst.[4-17,20-26]

In this context, copper has attracted significant attention because it is earth-abundant, inexpensive and non-toxic. In addition, it facilitates CO_2 capture and activation.[27-29] Actually, it has been reported that highly pure copper electrodes can efficiently catalyze electrochemical CO_2 reduction in aqueous media, and afford highly reduced species such as methane, ethane, and ethanol.[27] Inspired by this pioneering work, heterogeneous copper-based catalysts have intensively been studied in recent years.[30] However, reports on copper-based homogeneous molecular catalyst for CO_2 reduction have been limited.[20-26] Moreover, the catalytic activities of copper complexes for CO_2 reduction are much lower (turnover frequency (TOF) $\leq$ 1.15 s^{-1})[24] than those of the reported molecular catalysts based on manganese (5,011 s^{-1}),[16] iron (7,300,000 s^{-1}),[12] cobalt (33,000 s^{-1}),[14] and nickel (190 s^{-1}).[17] These limitations associated with the copper-based CO_2 reduction catalysts have prompted us to explore a new copper-based molecular catalyst with high performance.

In this chapter, I report a copper-based molecular catalyst that exhibits highly active electrochemical CO_2 reduction. Electrochemical analysis revealed that the TOF value for CO_2 to CO conversion was the highest among the copper-based molecular

catalysts. The catalytic Tafel plot[31,32] also indicated that the TOF value was high even at a very low overpotential, which is superior to that of most molecular catalysts reported so far.

Results and discussions

I assumed that the following three factors are crucial for constructing an efficient catalytic system for electrochemical CO_2 reduction. First, the copper porphyrin complex is used as a scaffold; metal porphyrin complexes are considered as efficient scaffolds for catalysis owing to their flexible redox properties and robustness during the catalysis.[3-12] Second, a strong electron-withdrawing substituent is introduced at the meso positions of the porphyrin framework; generally, strong electron-withdrawing groups are preferred in the electrochemical reduction reaction to lower the overpotential.[33] Finally, acetonitrile (MeCN) was used as the reaction medium; as described in chapter II, the catalytic activity of the iron(III) porphyrin complex is improved dramatically in MeCN than those in other solvents, and thus, I used MeCN herein.

As a candidate that satisfies all the aforementioned factors, I employed copper(II) tetrakis(pentafluorophenyl)porphyrin (**CuTPFP**) shown in Scheme 1. **CuTPFP** contains a copper porphyrin framework with pentafluorophenyl groups at the meso positions. Pentafluorophenyl groups act as strong electron-withdrawing substituents. In addition, **CuTPFP** is well soluble in MeCN because of these groups. The synthesis of **CuTPFP** was performed by modifying a previously reported method.[34] **CuTPFP** was characterized by elemental and single-crystal X-ray structural analysis (Figure 1 and Table 1).

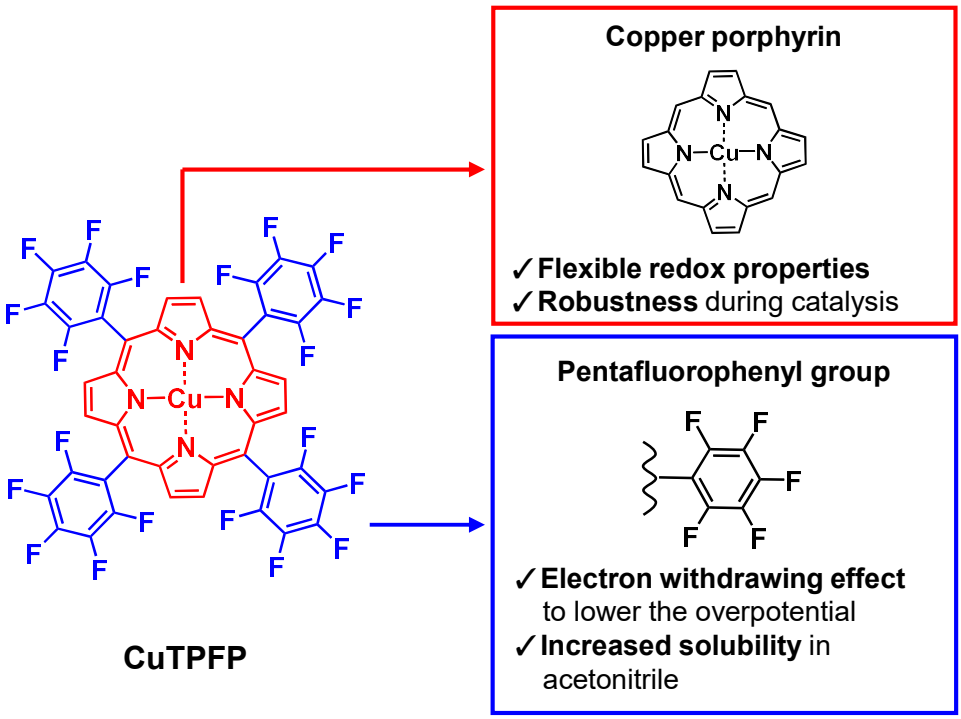

Scheme 1. Chemical structure and characteristics of **CuTPFP**.

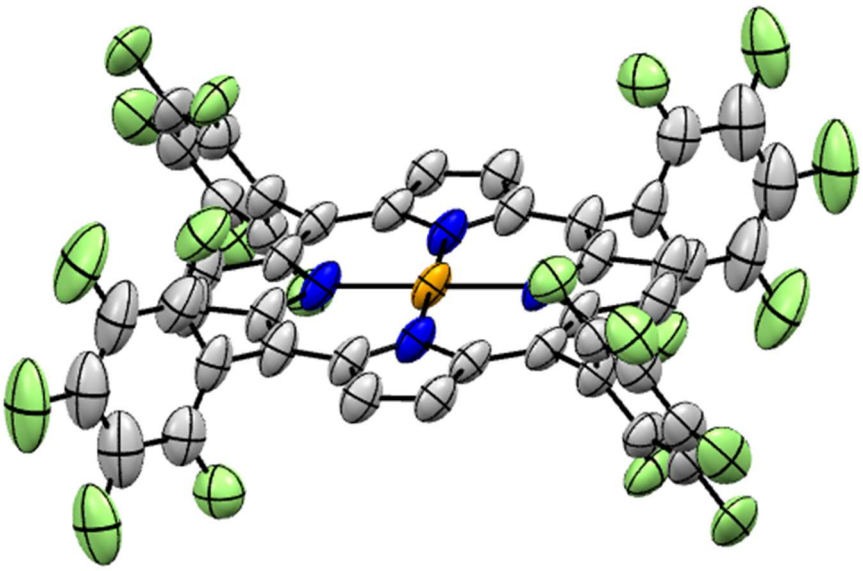

Figure 1. ORTEP drawings of the structure of **CuTPFP**. Non-coordinated solvent molecules and hydrogen atoms have been omitted for clarity. Thermal ellipsoids are shown at the 50% level. C = grey, N = blue, F = light green and Cu = orange.

Table 1. Summary of crystallographic data for **CuTPFP**.

	CuTPFP
Formula	$C_{44}H_8CuF_{20}N_4 \cdot 2.0\ C_2H_3N$
Fw	1182.0
Crystal color, habit	Red, plate
Crystal size / nm^3	0.105 × 0.308 × 1.043
Crystal system	Monoclinic
Space group	$P\ 2_1/n$
a / Å	13.9205(7)
b / Å	11.2461(5)
c / Å	15.0429(6)
α / °	90
β / °	115.758(5)
γ / °	90
V / $Å^3$	2120.99(18)
Z	2
F(000)	1106.0
d_{calc} / g cm^{-3}	1.751
μ(MoKa) / mm^{-1}	0.605
T / K	123(2)
R_1	0.0954
wR_2	0.2428
GooF	1.160

Cyclic voltammetry measurements

Initially, the cyclic voltammetry of **CuTPFP** was measured in a 0.1 M tetra-*n*-butylammonium perchlorate (TBAP)/MeCN solution. Under Ar atmosphere, **CuTPFP** exhibited two redox waves at –1.32 V and –1.77 V [vs. ferrocene/ferrocenium (Fc/Fc^+)] (Figure. 2a and Table 2). Due to the electron-withdrawing effect of the pentafluorophenyl group, the redox potentials of **CuTPFP** shifted to more positive potential than those of copper(II) tetraphenyl porphyrin, **CuTPP** (–1.64 and –2.16 V, Figure 2a and Table 2). Here, redox potentials were compared in a 0.1 M TBAP/*N*, *N*-dimethylfolmamide (DMF) solution because **CuTPP** does not dissolve in MeCN. The peak currents corresponding to these redox potentials of **CuTPFP** have a linear relationship with the square root of the scan rate and follow the Randles–Sevcik equation,

$$I_{\mathrm{P}} = 0.4463nFAC^{*}_{\mathrm{cat}}\sqrt{\frac{nFv}{RT}}\sqrt{D_{\mathrm{cat}}}, \qquad (1)$$

indicating that **CuTPFP** can facilitate rapid electron transfer reactions (Figure 2b and 2c). Here, n is the number of electrons (n = 1), F is the Faradaic constant (96485 C mol^{-1}), A is the electrode surface area (0.071 cm^2), C_{cat}^{*} is the concentration of the catalyst (mol cm^{-3}), R is the gas constant (8.31 J K^{-1} mol^{-1}), v is the scan rate (V s^{-1}), D_{cat} is the diffusion coefficient of the catalyst (cm^2 s^{-1}) and T is the temperature (298.15 K). Under CO_2 atmosphere in the presence of 1.0 M trifluoroethanol (TFE) as a proton source, **CuTPFP** exhibited a large irreversible current at –1.67 V, suggesting the electrocatalytic activity of the complex for CO_2 reduction (Figure 2d, blue line).

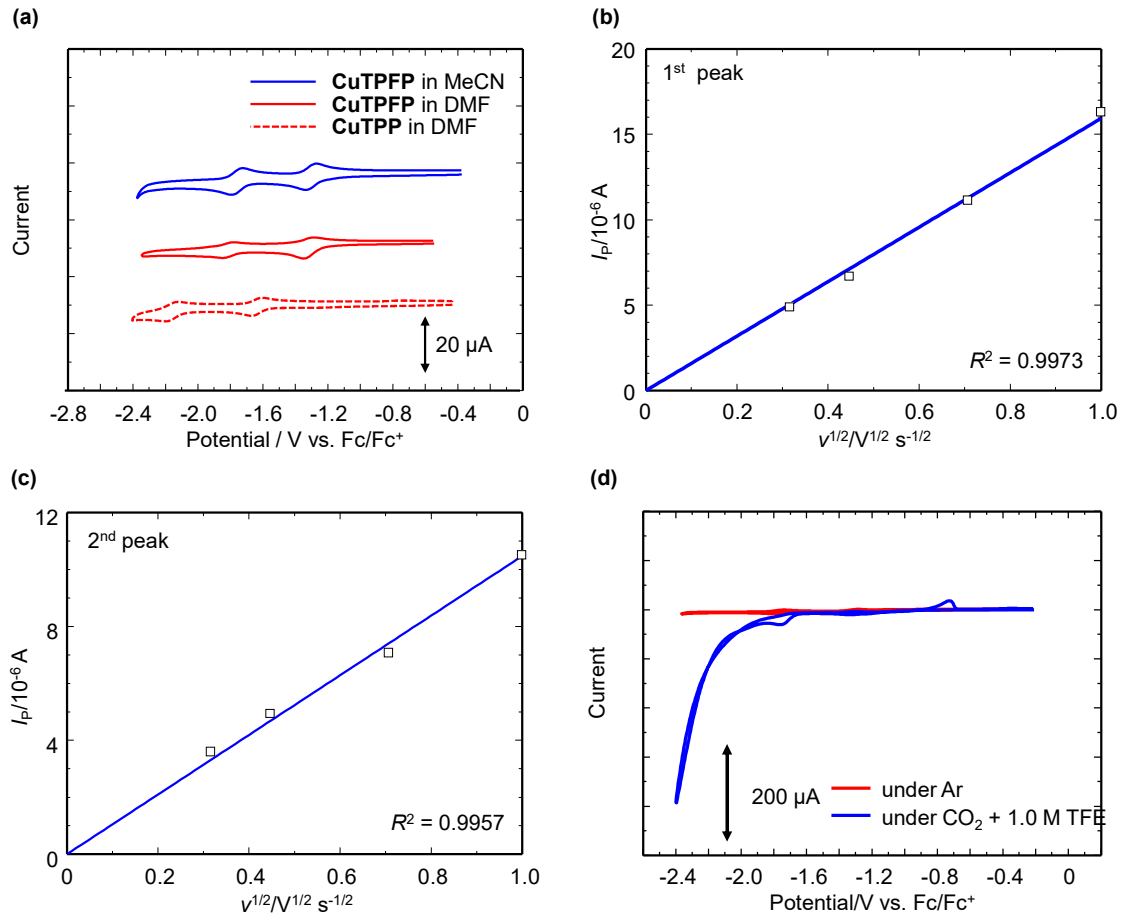

Figure 2. (a) Cyclic voltammograms of **CuTPFP** (0.20 mM) in MeCN (blue line) and DMF (red line) and of **CuTPP** in DMF (dashed line) with TBAP (0.1 M) under Ar (scan rate: 100 mV s^{-1}). (b) Variation of peak current of **CuTPFP** (0.20 mM) in 0.1 M TBAP/MeCN at the first redox wave. (c) Variation of peak current of **CuTPFP** (0.20 mM) in 0.1 M TBAP/MeCN at the second redox wave. (d) Cyclic voltammograms of **CuTPFP** (0.20 mM) in MeCN with TBAP (0.1 M) in the presence of TFE (1.0 M) under CO_2 (scan rate: 100 mV s^{-1}).

Table 2. Redox potentials ($E_{1/2}$/V vs. Fc/Fc^+) of **CuTPFP** in 0.1 M TBAP/MeCN, **CuTPFP** in 0.1 M TBAP/DMF and **CuTPP** in 0.1 M TBAP/DMF.

Catalyst	Solvent	$E_{1/2}(1)$	$E_{1/2}(2)$
CuTPFP	MeCN	–1.32	–1.77
CuTPFP	DMF	–1.32	–1.82
CuTPP	DMF	–1.64	–2.16

Controlled potential electrolysis experiments

To quantify the catalytic product, a controlled potential electrolysis (CPE) experiment of **CuTPFP** was performed in MeCN with 0.1 M TBAP, in the presence of 1.0 M TFE, under CO_2 at –2.39 V vs. Fc/Fc^+. In the CPE experiment, tetra-*n*-butyl ammonium acetate (TBAA) was added to the anodic chamber (Figure 3) to promote the oxidation process on the Pt counter electrode. TBAA reacts at the anode to consume the holes and produce CO_2 and ethane via the Kolbe reaction.[10] As a result, the total amount of charge passed over a period of 60 min was 72.4 C (Figure 4). The products of the reaction were also quantified by gas chromatography and high-performance liquid chromatography, and the formation of CO, HCOOH, and H_2 was confirmed with a Faradaic efficiency (FE) of 76.6% (287.4 μmol), 19.6% (73.5 μmol) and 1.7% (6.4 μmol), respectively. I also note the almost linear evolution of the charge during electrolysis, indicating no noticeable sign of catalyst degradation.

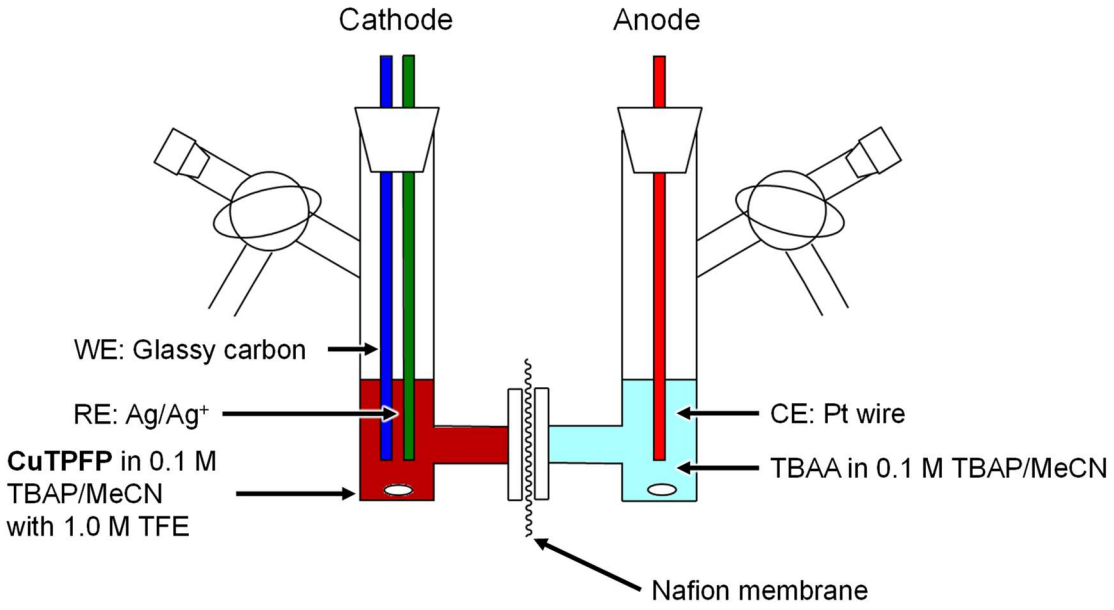

Figure 3. Schematic representation of the custom-designed two compartment cell used in the controlled potential electrolysis experiments.

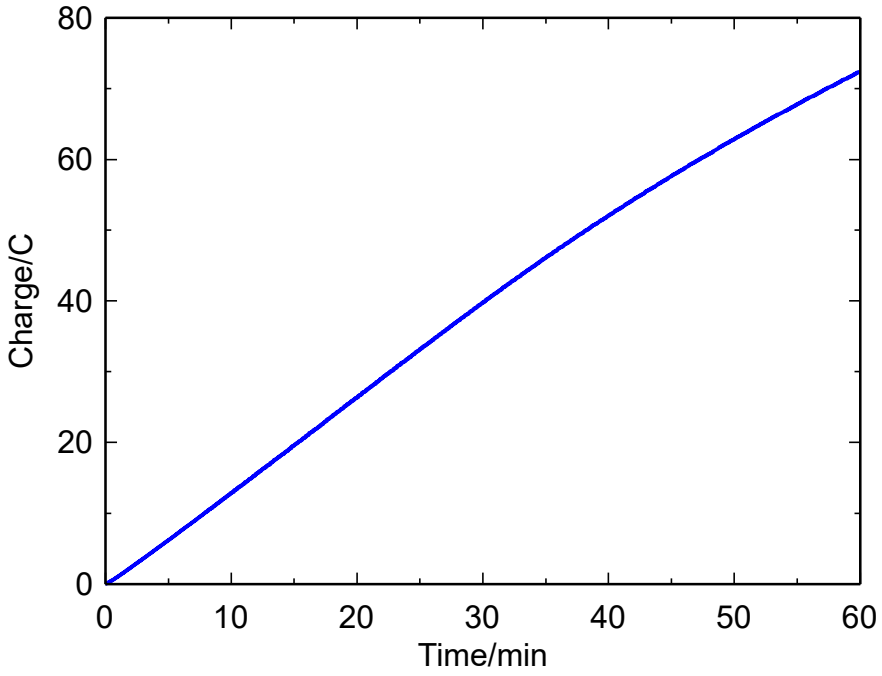

Figure 4. Electrolysis data of **CuTPFP** (20 μM) in MeCN with TBAP (0.1 M) in the presence of TFE (1.0 M) under CO_2 at a potential of −2.39 V vs. Fc/Fc^+. Working electrode: glassy carbon, counter electrode: Pt wire, reference electrode: Ag/Ag^+.

After the CPE experiment, I confirmed the structure of molecular catalyst by the following several analyzes. First, I performed a dynamic light scattering measurement of the solution after the CPE experiment and confirmed that there was no particle formation in the solution, which is evidence of the homogeneous nature of **CuTPFP** (Figure 5). Second, the UV-absorption spectra of **CuTPFP** measured before and after the CPE experiment. As shown in Figure 6, both spectra are almost identical, which indicate that the electronic structure of **CuTPFP** was maintained after the electrolysis for 1h. Finally, I examined the catalytic ability of the electrode after the CPE experiment. The glassy carbon working electrode used in the electrolysis with catalyst (Figure 7, blue line) was gently rinsed with small amount of MeCN, and then, a second round of electrolysis was performed using the solution without the catalyst (Figure 7, black line). A small current was observed in the second electrolysis compared to the first electrolysis, and CO_2 reduction products were not observed (Table 3), which indicate that the homogeneous species dissolved in the solution is a catalytic active species. These results clearly demonstrate that **CuTPFP** can function as a robust homogeneous CO_2 reduction catalyst.

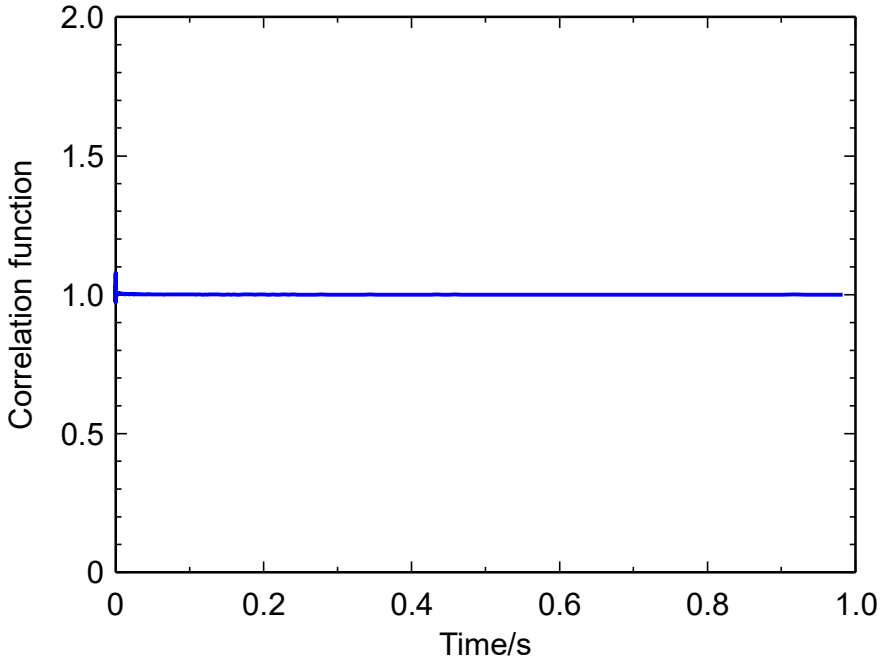

Figure 5. Dynamic light scattering measurement of **CuTPFP** (20 μM) after CPE experiment.

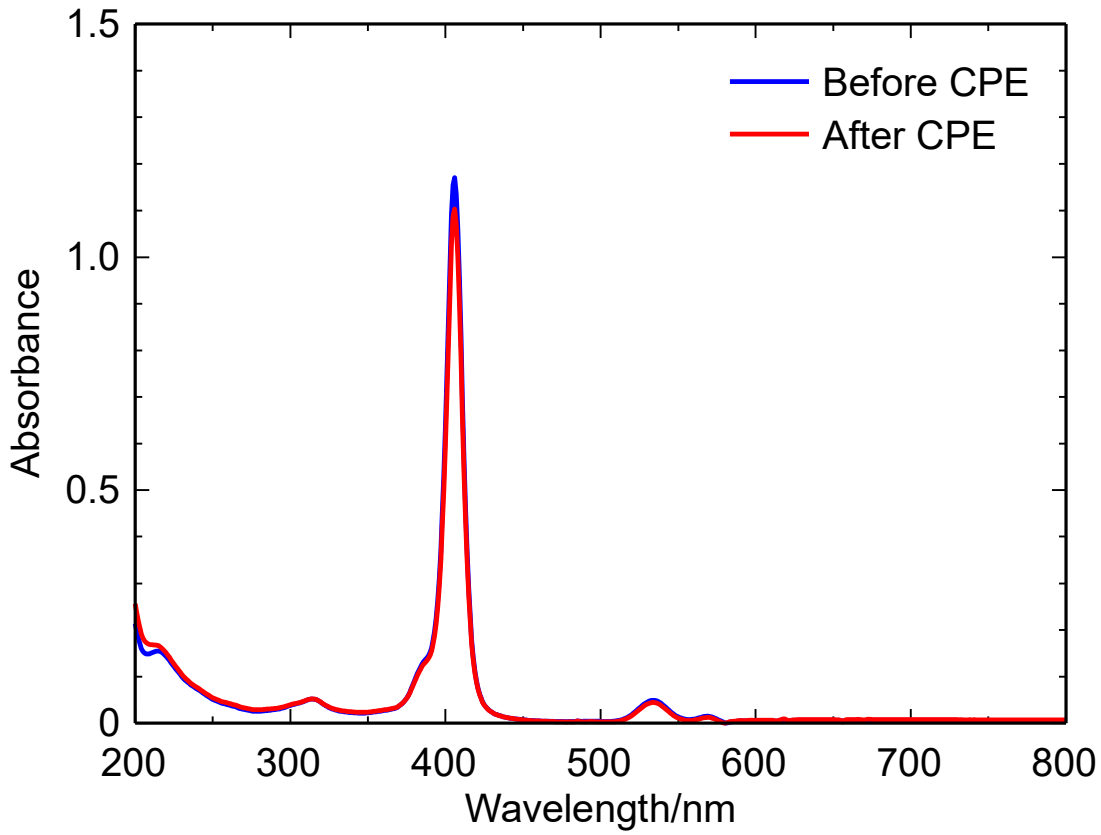

Figure 6. UV-visible absorption spectra of **CuTPFP** in MeCN with 0.1 M TBAP in the presence of 1.0 M TFE under CO_2 before (blue line) and after (red line) the controlled potential electrolysis at –2.40 V vs. Fc/Fc^+ for 1h.

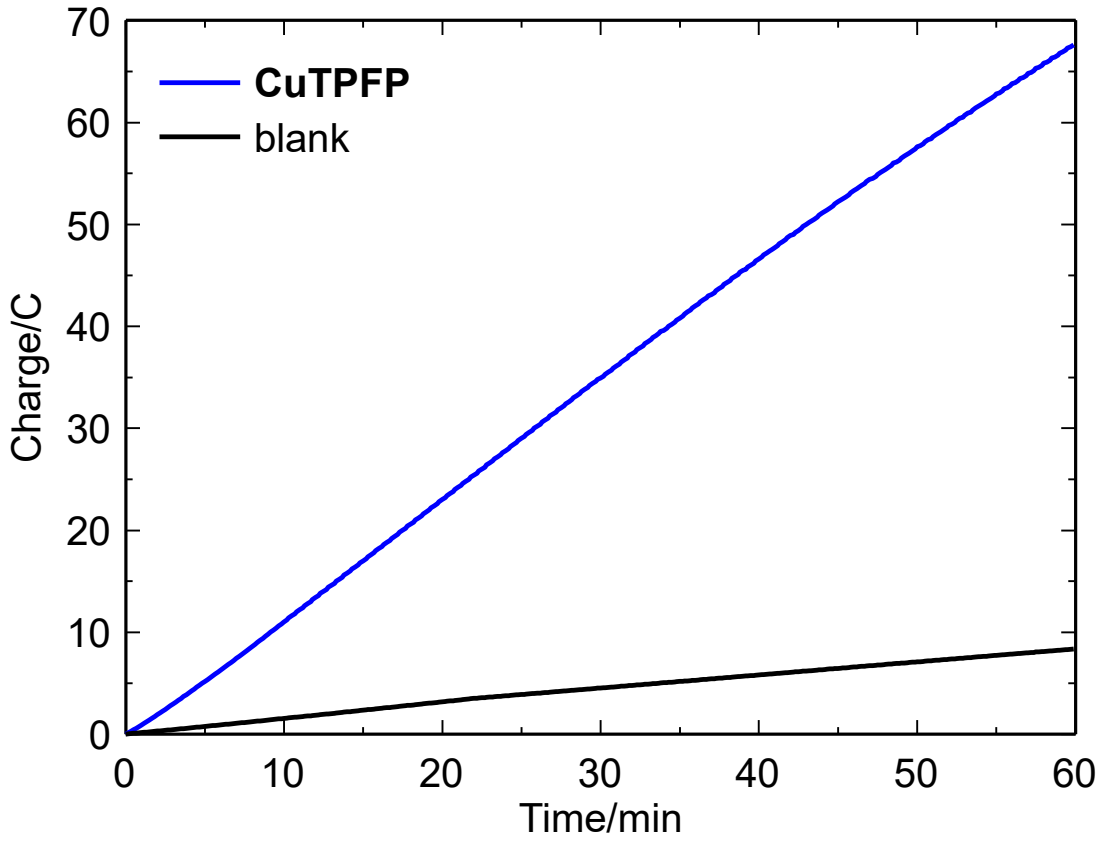

Figure 7. The result of the first electrolysis using fresh glassy carbon electrode in 0.20 mM of **CuTPFP** (blue line) and that of second round of electrolysis using grassy carbon electrode after first electrolysis in electrolyte solution without **CuTPFP** (black line). Condition: MeCN solution with TBAP (0.1 M) under CO_2 in the presence of 1.0 M TFE at a potential of –2.40 V vs. Fc/Fc^+.

Table 3. Summary of the CPE experiments in Figure 7.

Media	Catalyst/mM	Potential/ V vs. Fc/Fc^+	Total charge/C	Faradaic efficiency/%			
				CO	HCOOH	H_2	Total
0.1 M TBAP/MeCN, 1.0 M TFE	0.20	–2.40	67.7	72.6	24.7	2.6	99.9
0.1 M TBAP/MeCN, 1.0 M TFE	blank	–2.40	8.3	n.d.	trace	0.7	0.7

Turnover frequency calculation

To evaluate the catalytic activity of **CuTPFP**, a catalytic Tafel plot for CO production was then constructed.[31,32] In the electrochemical condition, only small quantity of the catalyst close to the surface of the working electrode is catalytically active. Therefore, the TOF value of the electrochemical CO_2 reduction is defined as

$$\mathrm{TOF} = \frac{k_{\mathrm{cat}}}{1 + \exp[f(E - E^0_{\mathrm{cat}})]}, \tag{2}$$

where k_{cat} is the observed rate constant, $f = F/RT$, E is the applied potential, and E^0_{cat} is the redox potential of the catalyst. Here, k_{cat} values were extracted directly from the results of CPE experiments at varying applied potentials (Figure 8 and Table 4) using

$$I_{\mathrm{cat}} = \frac{nFAC^*_{\mathrm{cat}}\sqrt{k_{\mathrm{cat}}D_{\mathrm{cat}}}}{1 + \exp[f(E - E^0_{\mathrm{cat}})]}, \tag{3}$$

where I_{cat} is the average catalytic current during electrolysis, n is the number of electrons ($n = 2$), A is the electrode area (1.2 cm^2), F is the Faradaic constant (96485 C mol^{-1}), C_{cat}^* is the concentration of the catalyst (mol cm^{-3}), and D_{cat} is the diffusion coefficient of the catalyst (cm^2 s^{-1}). E^0_{cat} and C_{cat}^* are –1.77 V vs. Fc/Fc^+ and 2.00×10^{-8} mol cm^{-3}, respectively (Table 2). $D_{cat} = 7.58 \times 10^{-6}$ cm^2 s^{-1} is determined using Eq.(1) and the slope of Figure 1c. It is useful to benchmark the performance of a catalyst as a function of the overpotential (η); therefore, I converted the applied potentials into overpotentials ($\eta = E - E_{CO2/CO}$, $E_{CO2/CO}$ = –1.54 V vs. Fc/Fc^+[11,35]) and TOF is given by

$$\mathrm{TOF} = \frac{k_{\mathrm{cat}}}{1 + \exp[f(E_{\mathrm{CO_2/CO}} - E^0_{\mathrm{cat}})]\exp(-f\eta)}. \tag{4}$$

As shown in Figure 9, TOF increased as the overpotential increased and reached a plateau at $\eta = 0.66$ V. Detailes are summarized in Table 5 and the maximum TOF value (TOF_{max}) was 1,460,000 s^{-1} at $\eta = 0.85$ V. Surprisingly, this value is more than 1,000,000 times greater than those of other reported copper-based catalysts (Figure 10 and Table 6). I also calculated the turnover number (TON) of the catalytic reaction, and the value was reached

to 5.26×10^9 (for the details of the determination of the TON, see the footnote of the Table 8).

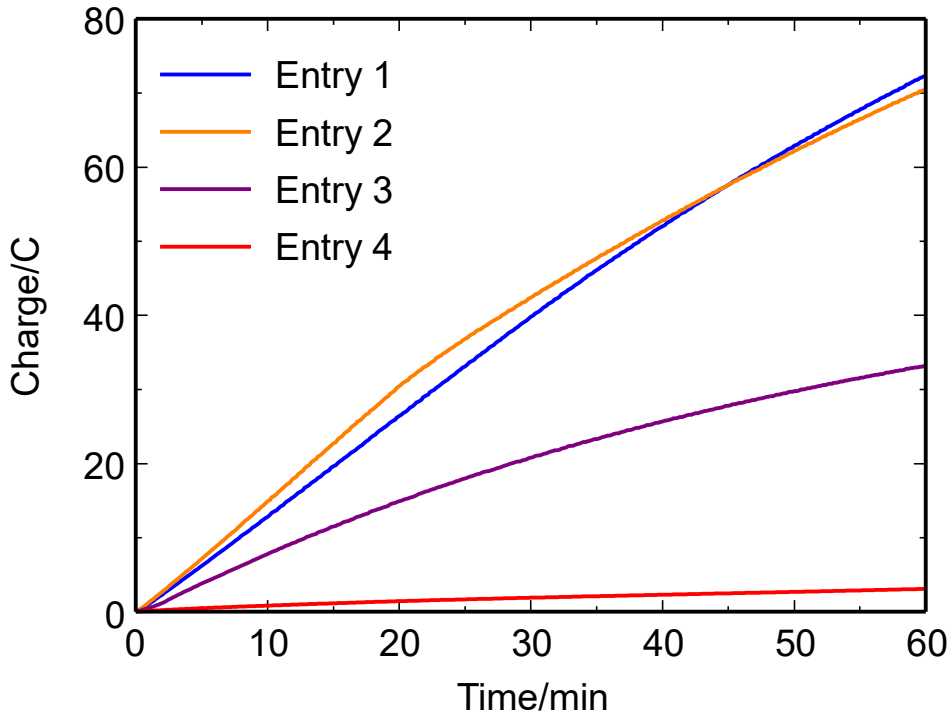

Figure 8. The results of CPE experiments of **CuTPFP** (20 μM) at various applied potential (vs. Fc/Fc^+) for 1 h. Details of the experimental condition are summarized in Table 4. Working electrode: glassy carbon (1.2 cm^2), counter electrode: Pt wire, reference electrode: Ag/Ag^+.

Table 4. Summary of the CPE experiments of **CuTPFP** (20 μM).

Entry	Media	Potential/ V vs. Fc/Fc^+	Total charge/C	Faradaic efficiency/%			
				CO	HCOOH	H_2	Total
1	0.1 M TBAP/MeCN, 1.0 M TFE	−2.39	72.4	76.6	19.6	1.7	98.2
2	0.1 M TBAP/MeCN, 1.0 M TFE	−2.20	70.5	75.9	16.6	4.1	95.8
3	0.1 M TBAP/MeCN, 1.0 M TFE	−2.03	33.2	56.3	22.1	7.6	90.2
4	0.1 M TBAP/MeCN, 1.0 M TFE	−1.71	3.1	18.7	4.3	13.5	63.0

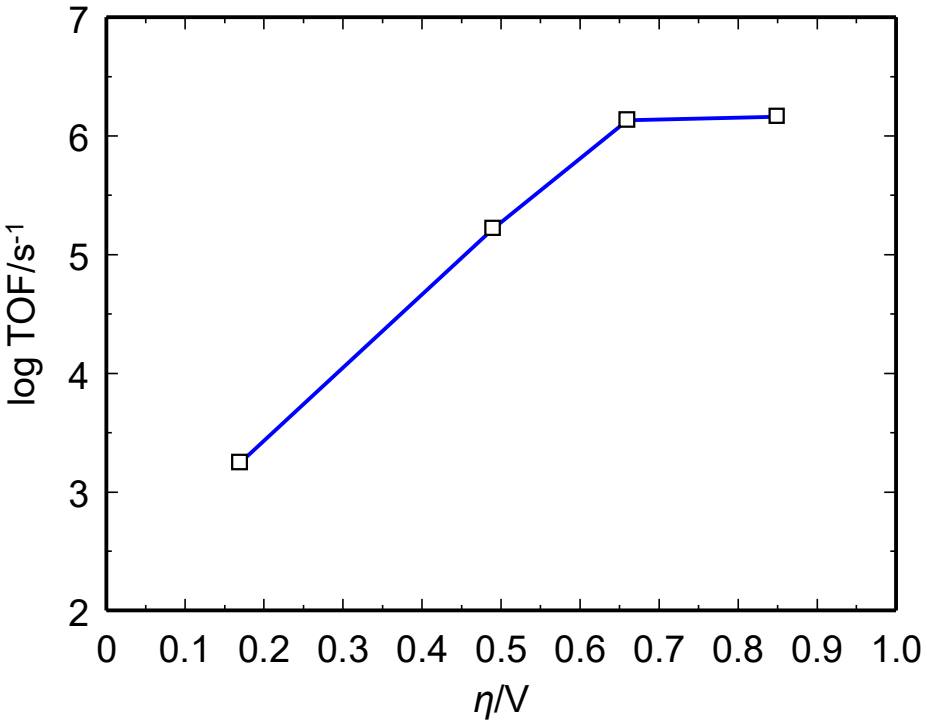

Figure 9. Catalytic Tafel plot of **CuTPFP** in MeCN with TBAP (0.1 M) for CO_2 to CO conversion obtained from CPE experiments at varying overpotentials. Working electrode: glassy carbon, counter electrode: Pt wire, reference electrode: Ag/Ag^+.

Table 5. TOF values of **CuTPFP** for electrochemical CO_2 reduction. The kinetic data was determined from the average of 1 h variable potential CPE experiments with direct product detections.

Entry	Media	Potential/V vs. Fc/Fc^+	η/V	TOF/s^{-1}	log TOF/s^{-1}
1	0.1 M TBAP/MeCN, 1.0 M TFE	–2.39	0.85	1.46×10^6	6.16
2	0.1 M TBAP/MeCN, 1.0 M TFE	–2.20	0.66	1.36×10^6	6.13
3	0.1 M TBAP/MeCN, 1.0 M TFE	–2.03	0.49	1.66×10^5	5.22
4	0.1 M TBAP/MeCN, 1.0 M TFE	–1.71	0.17	1.77×10^3	3.25

Table 6. TOFs of the copper-based molecular catalyst for CO_2 reduction.

Catalyst[a]	Media	Reductant	TOF/s^{-1}[b]	Reference
CuTPFP	0.1 M TBAP/MeCN, 1.0 M TFE	Electrochemical	1.46×10^{6}[c] (–2.39 V vs. Fc/Fc^{+})	This work
Cu1	THF[d]	pinB[e]	1.39×10^{-2}[f]	20
Cu2	THF	pinB	2.78×10^{-2}[f]	20
Cu3	0.1 M TBAP/MeCN	Electrochemical	5.56×10^{-4}[c],[f] (–1.7 V vs. Ag/AgCl)	21
Cu4	$MeCN/H_2O$ (v/v = 97:3), 0.1 M BIH[g]/TEOA[h] (15% v/v)	Photochemical (λ > 420 nm)	1.15	24
Cu5	$MeCN/H_2O$ (v/v = 4:1), 0.3 M TEOA	Photochemical (λ = 450 nm)	2.75×10^{-1}[f]	25
Cu6	$MeCN/H_2O$ (v/v = 4:1), 0.3 M TEOA	Photochemical (λ = 400 nm)	8.40×10^{-1}[f]	26

[a] The chemical structures of **Cu1**–**Cu6** are shown in Figure 10. [b] The TOF value cannot be directly compared without recognizing that reaction conditions such as solvent, reductant, and applied potential differ. [c] Calculated from CPE data. [d] THF = tetrahydrofuran [e] pinB = 4,4,5,5-Tetramethyl-1,3,2-dioxaborolane. [f] TOF was calculated by dividing the turnover number by the time during catalysis. [g] BIH = 1,3-dimethyl-2-phenyl-2,3-dihydro-1H-benzo[d]imidazole. [h] TEOA = triethanolamine.

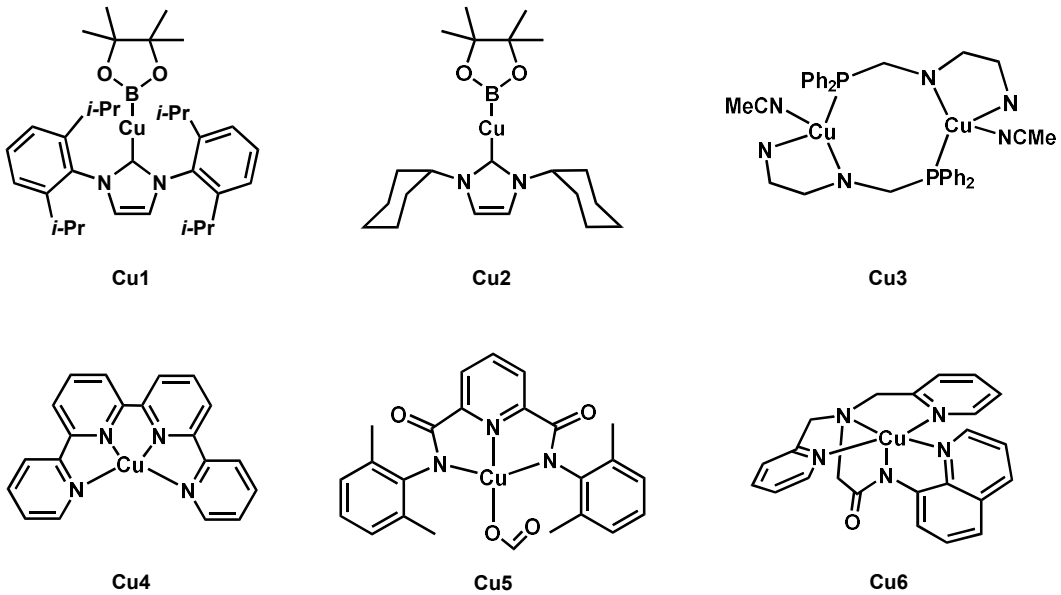

Figure 10. Chemical structure of copper-based molecular catalysts for CO_2 reduction.

It should be noted that the TOF values of **CuTPFP** are significantly larger than that of a copper porphyrin without pentafluorophenyl functional groups, **CuTPP** (18,200 s^{-1}). The TOF value of **CuTPP** was determined as follows. First, I performed cyclic voltammetry measurement of **CuTPP**. As **CuTPP** did not dissolve in pure MeCN, the CPE was performed in MeCN-DMF [1:1 (v/v)] mixed solvent system. Under Ar, **CuTPP** exhibited two redox potentials at –1.65 and –2.13 V (Figure 11a, red line). The peak currents corresponding to these redox potentials of **CuTPP** have a linear relationship with the square root of the scan rate and follow the Randles–Sevcik equation, indicating that **CuTPP** can facilitate rapid electron transfer reactions (Figure 11b). Using Eq.(1) and the slope of Figure 11b, D_{cat} of **CuTPP** was 9.24×10^{-6} cm^2 s^{-1}. Under CO_2 in the presence of TFE, **CuTPP** exhibited an irreversible current, suggesting the electrocatalytic activity of the complex for CO_2 reduction (Figure 11a, blue line). Subsequently. I performed CPE experiment of **CuTPP** at –2.39 V. As a result, the total amount of charge passed over a period of 60 min was 8.4 C (Figure 12 and Table 7). The products of the reaction were quantified and the formation of CO, HCOOH, and H_2 was confirmed with a Faradaic efficiency of 81.5%, 17.1% and 1.0%, respectively. Based on the result of CPE experiment and Eq.(2), I evaluated TOF of **CuTPP** (vide supra).

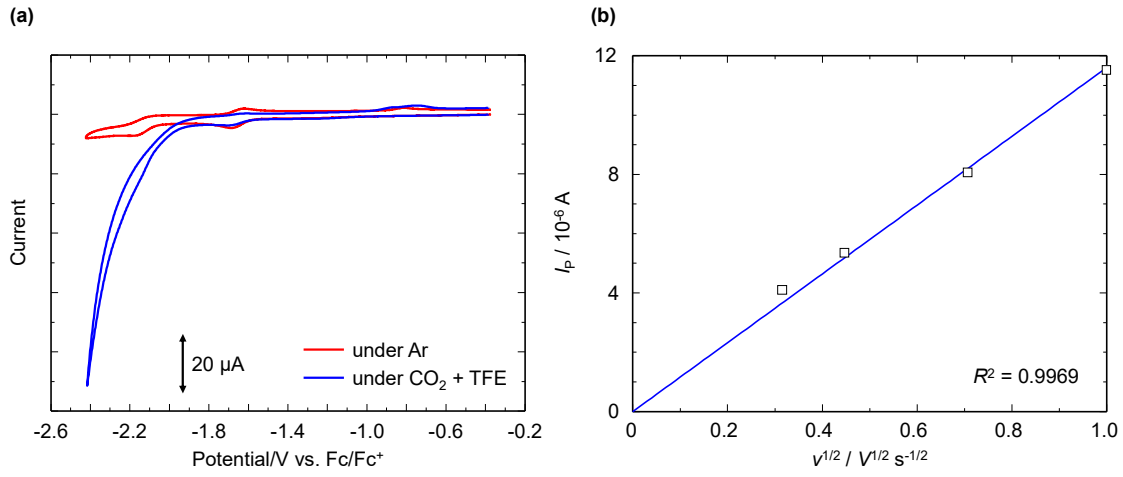

Figure 11. (a) Cyclic voltammograms of **CuTPP** (0.2 mM) in DMF/MeCN [1:1 (v/v)] mixed solvent with TBAP (0.1 M) under Ar (red line) and under CO_2 in the presence of 0.5 M TFE (blue line). Scan rate: 100 mV s^{-1}. (b) Variation of peak current of **CuTPP** (0.2 mM) in DMF/MeCN [1:1 (v/v)] mixed solvent with TBAP (0.1 M) under Ar at the second redox wave.

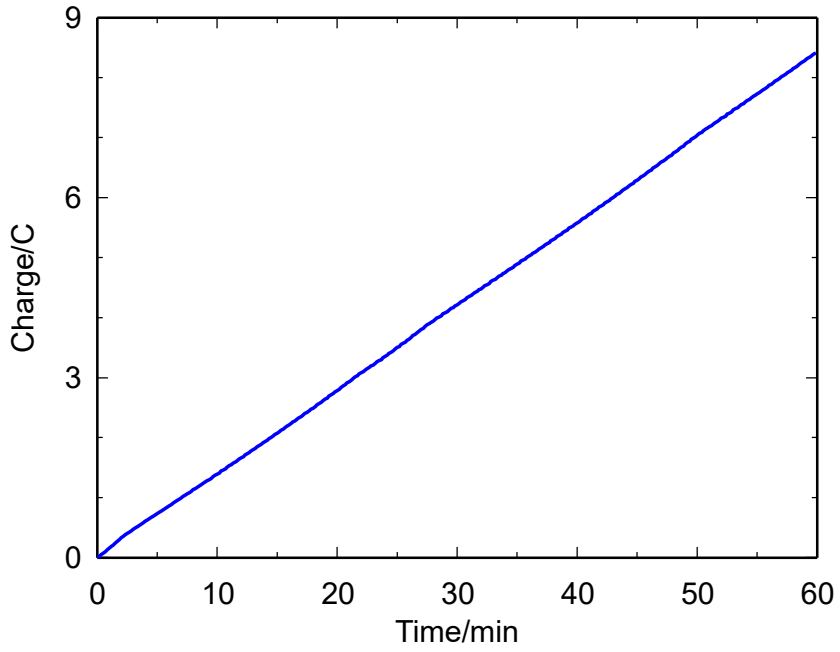

Figure 12. The result of CPE experiment of **CuTPP** (0.02 mM) at –2.39 V for 1h. Working electrode, glassy carbon (1.2 cm^2); counter electrode, Pt wire; reference electrode, Ag/Ag^+.

Table 7. Summary of the CPE experiment of **CuTPP**.

Media	Catalyst/mM	Potential/ V vs. Fc/Fc^+	Total charge/C	Faradaic efficiency/%			
				CO	HCOOH	H_2	Total
DMF/MeCN [1:1 (v/v)], 0.1 M TBAP, 1.0 M TFE	0.02	–2.39	8.4	81.5	17.1	1.0	99.6

I also compared the catalytic activity of **CuTPFP** with that of other metal-complex-based molecular catalysts. Table 8 shows that the TOF_{max} value of **CuTPFP** is comparable to that of current, high-performing metal-complex-based molecular catalysts for electrochemical CO_2 reduction (Figure 13). The catalytic Tafel plots of several metal-complex-based molecular catalysts also enabled the comparison of their TOFs, in terms of overpotential. As shown in Figure 14, the TOF value of **CuTPFP** was 1,770 s^{-1} at η = 0.17 V. This performance is superior to those of most metal-complex-based molecular catalysts, indicating that **CuTPFP** is an excellent catalyst, even at very low overpotentials. In other words, **CuTPFP** is a highly active electrocatalyst for CO_2 reduction from low to high overpotentials.

Table 8. TOFs of the recent efficient molecular catalysts for electrochemical CO_2 reduction.

Catalyst	Solvent	TOF_{max} (CV)/s^{-1} [a]	TOF (CPE)/s^{-1} [b]	Ref.
CuTPFP	0.1 M TBAP/MeCN,	-	1,460,000[c]	This work
	1.0 M TFE		(–2.39 V *vs*. Fc/Fc^+)	
Fe1	0.1 M TBAP/MeCN,	650,000[d]	7,300,000	12
	1.0 M TFE		(–2.35 V *vs*. Fc/Fc^+)	(Chapter 2)
Fe1	0.1 M $TBAPF_6$/DMF,	31,600	-	4
	3.0 M PhOH			
Fe2	0.1 M $TBAPF_6$/DMF,	5,500,000	-	6
	0.5 M PhOH			
Fe3	0.1 M $TBAPF_6$/DMF,	1,000,000	-	7
	0.1 M H_2O + 3.0 M PhOH			
Fe4	0.1 M $TBAPF_6$/DMF,	15,800	-	7
	0.1 M H_2O + 3.0 M PhOH			
Fe5	0.1 M $TBAPF_6$/DMF,	10,000	240	10
	3.0 M PhOH		(–1.10 V *vs*. NHE)	
Fe6	0.1 M $TBAPF_6$/DMF,	6,300	170	10
	3.0 M PhOH		(–1.16 V *vs*. NHE)	
Fe7	0.1 M $TBAPF_6$/MeCN,	-	900,000	15
	3.5 M PhOH		(–1.98 V *vs*. Fc/Fc^+)	
Co1	0.1 M $TBAPF_6$/MeCN,	33,000	533	14
	3.0 M PhOH		(–1.25 V *vs*. SCE)	
Mn1	0.1 M $TBAPF_6$/MeCN,	5,011	-	16
	0.3 M TFE			
Ni1	0.1 M $TBAPF_6$/MeCN,	-	190	17
	25% H_2O		(–1.16 V *vs*. NHE)	

[a] calculated from CV data. [b] calculated from CPE data. [c] TON (TOF × time, 1h) = 5.26 × 10^9, TON (mol(CO)/mol(catalyst), 1h) = 2.87 × 10^3. [d] TOF_{max} is calculated using the data where $I_{cat}/I_p < 1$.

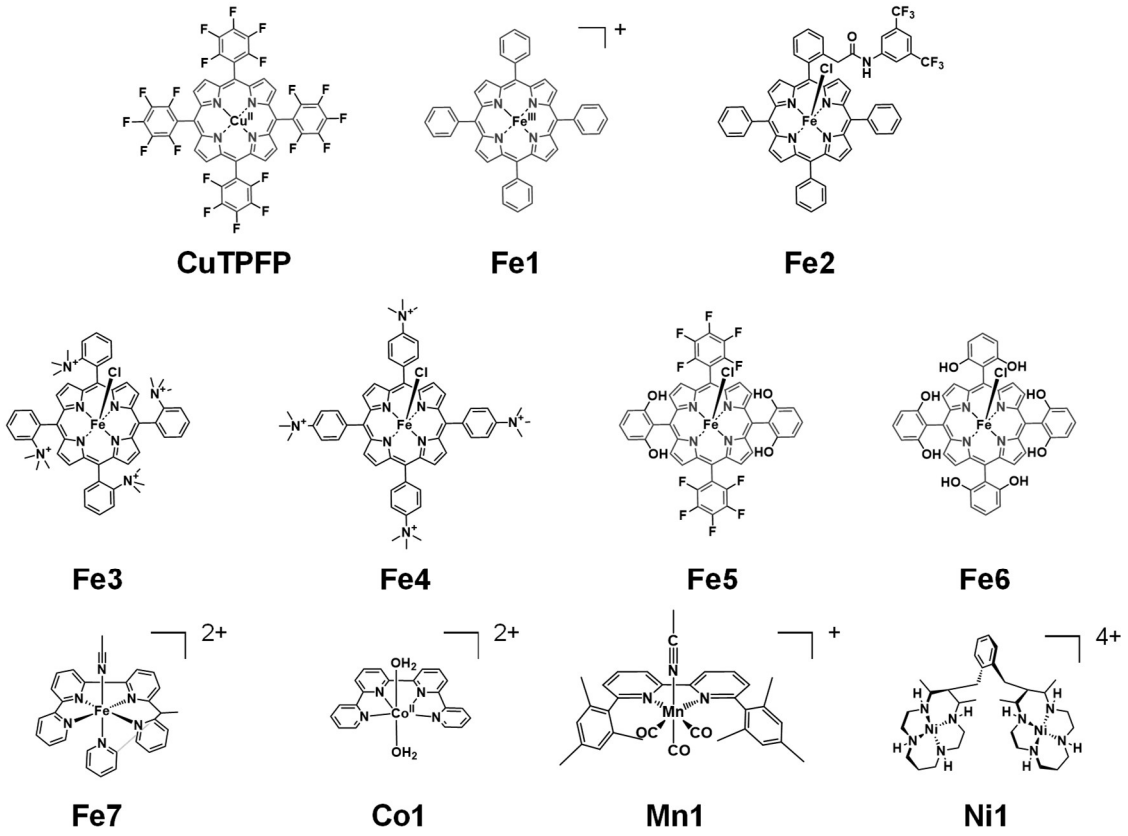

Figure 13. Chemical structures of the recent efficient molecular catalysts for electrochemical CO_2 reduction.

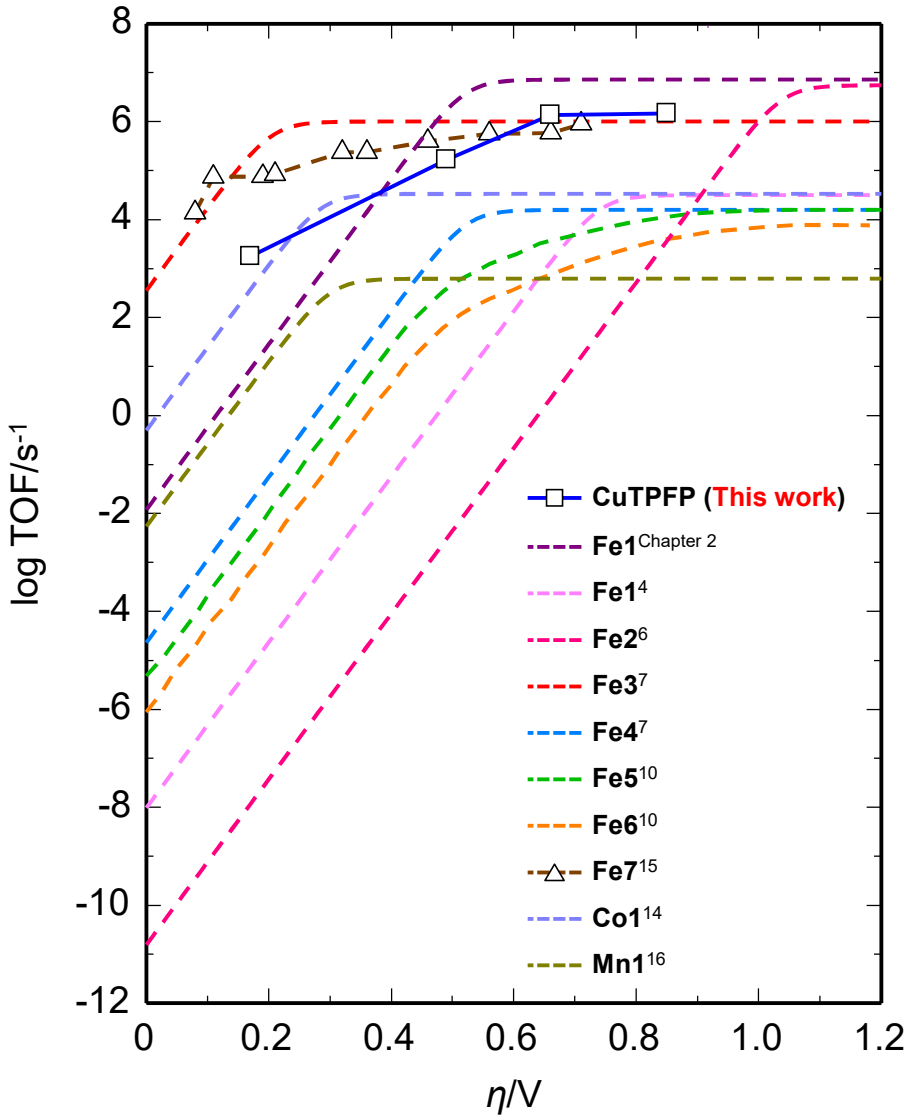

Figure 14. Benchimarking of the metal-complex-based molecular catalysts of the CO_2 to CO electrochemical conversion by means of their catalytic Tafel plots.

Conclusion

In conclusion, I have shown a copper-based homogeneous catalyst that exhibits highly active electrochemical CO_2 reduction. Herein, I selected **CuTPFP** as a copper-based molecular catalyst that satisfied the following three elements: (i) copper porphyrin as a scaffold, (ii) introduction of strong electron-withdrawing substituents, and (iii) soluble in MeCN as a reaction medium. CPE experiments indicated that **CuTPFP** functioned as a robust homogeneous CO_2 reduction catalyst. Furthermore, it exhibited a TOF value for CO production of 1,460,000 s^{-1}, which is more than 1,000,000 times higher than those of other reported copper-based catalysts. The catalytic Tafel plot for CO production revealed that the activity of **CuTPFP** was comparable to that of current best-in-class molecular catalysts across a wide range of overpotentials. The TOF value of **CuTPFP** at a low overpotential (1,770 s^{-1} at η = 0.17 V) was superior than those of most catalysts, demonstrating the advantages of **CuTPFP**.

Experimental section

General procedures

Pyrrole was purchased from Sigma-Aldrich Co., LLC. Benzaldehyde and ferrocene were purchased from Wako Pure Chemical Industries, Ltd. Propanoic acid was purchased from Kishida Chemical Co., LLC. Methanol, chloroform ($CHCl_3$), *N*, *N*-dimethylformamide (DMF), hexane, acetonitrile (MeCN), and copper(II) acetate monohydrate ($Cu(OAc)_2 \cdot H_2O$) were purchased from Kanto Chemical Co., Inc. 5,10,15,20-Tetrakis(pentafluorophenyl)porphyrin (**H_2TPFP**), tetra-*n*-butylammonium perchlorate (TBAP), tetra-*n*-butylammonium acetate (TBAA), and 2,2,2-trifluoroethanol were purchased from Tokyo Chemical Industry Co., Ltd. Chloroform-d_1 was purchased from Cambridge Isotopes, Inc. All solvents and reagents are of the highest quality available and used as received except for TBAP. TBAP was recrystallized from absolute ethanol. ^{1}H-NMR spectra were collected at room temperature on a JEOL JNM-ECS400 spectrometer. Elemental analysis was performed on a J-SCIENCE LAB MICRO CORDER JM10 elemental analyzer.

Synthesis

Synthesis of meso-tetraphenylporphyrin (H_2TPP)

H_2TPP was prepared as previously described.[36] Pyrrole (1.7 mL, 25 mmol) and benzaldehyde (2.6 mL, 25 mmol) were dissolved in propanoic acid (50 mL), then refluxed for 45 minutes and cooled to room temperature. The resulting mixture was filtered and washed with methanol. Recrystallization from $CHCl_3$/methanol gave a purple solid (785 mg, yield 20%). ^{1}H-NMR (400 MHz, $CDCl_3$): d = 8.82 (s, 8H), 8.19-8.21 (m, 8H), 7.71-7.78 (m, 12H), −2.80 (s, 2H) ppm. Elemental analysis Calcd. for $C_{44}H_{30.5}N_4O_{0.25}$ ($H_2TPP \cdot H_2O$): C, 85.34%; H, 4.96%; N, 9.05%. Found: C, 85.24%, H, 4.68%; N, 9.08%.

Synthesis of copper(II) tetraphenylporphyrin (CuTPP)

CuTPP was prepared by the modification of the previous report.[34] To a solution of **H_2TPP** (50 mg, 0.08 mmol) in DMF (5 mL), a 5 mL DMF solution of $Cu(OAc)_2 \cdot H_2O$ (80.9 mg, 0.41 mmol) was added at room temperature. The mixture was heated at 200 ˚C for 10 minutes by a microwave reactor. Water (50 mL) was added to the resulting solution.

Precipitate was collected by filtration and washed with water. Recrystallization from $CHCl_3$/hexane gave a red solid (37.5 mg, yield 68%). Elemental analysis Calcd. for $C_{44}H_{30}CuN_4O$ (**CuTPP**·1.0 H_2O): C, 76.12%; H, 4.36%; N, 8.07%. Found: C, 75.98%; H, 4.14%; N, 8.19%.

Synthesis of copper(II) tetrakis(pentafluorophenyl)porphyrin (CuTPFP)

CuTPFP was prepared by the modification of the previous report.[34] To a solution of **H_2TPFP** (50 mg, 0.08 mmol) in DMF (5 mL), a 5 mL DMF solution of $Cu(OAc)_2·H_2O$ (30.5 mg, 0.153 mmol) was added at room temperature. The mixture was heated at 200 ˚C for 10 minutes by microwave reactor. Water (50 mL) was added to the resulting solution. Precipitate was collected by filtration and washed with water. Recrystallization from $CHCl_3$/hexane gave a red solid (37.5 mg, yield 71%). Since this crystal was not suitable for single crystal X-ray structure analysis, **CuTPFP** was also recrystallized from MeCN/H_2O to give a large red plate. Elemental analysis Calcd. for $C_{47}H_{14}F_{20}CuN_4$ (**CuTPFP**·0.5 hexane): C, 52.36%; H, 1.31%; N, 5.20%. Found: C, 52.51%; H, 1.54%; N, 5.51%.

Electrochemistry

Electrochemical experiments were performed at room temperature on a BAS ALS Model 650DKMP electrochemical analyzer or Bio-Logic-Science Instruments potentiostat. Cyclic voltammetry (CV) measurements were performed by using a one-compartment cell with a three-electrode configuration, which consisted of a glassy carbon disk (diameter 3 mm, from BAS Inc.), platinum wire, and Ag/Ag^+ electrode (Ag/0.01 M $AgNO_3$) as the working, auxiliary, and reference electrodes, respectively. The glassy carbon disc working electrode was polished using 0.05 μm alumina paste (from BAS Inc.) and washing with purified H_2O prior to each measurement. Ferrocene was used as an internal standard and all potentials are referenced to the ferrocenium/ferrocene (Fc/Fc^+) couple at 0 V.

Controlled potential electrolysis (CPE)

CPE was performed in a gas-tight two-compartment electrochemical cell, where the first

compartment held the carbon plate working electrode (1.2 cm^2 surface area) and Ag/Ag^+ reference electrode (Ag/0.01 M $AgNO_3$) in 5 ml of 0.1 M TBAP/MeCN with catalyst and proton source, while the second compartment held the Pt auxiliary electrode in 5 ml of 0.1 M TBAP/MeCN containing TBAA (0.2 M) as sacrificial oxidant. The two compartments were separated by a Nafion® membrane. The solution was purged vigorously with CO_2 for 30 mins prior to electrolysis. The electrolysis experiment was performed for 1 h under constant stirring. The amount of CO and H_2 produced was quantified from an analysis of the headspace with a Shimadzu GC-8A with TCD detector equipped with a capillary column with Molecular Sieve 13X-S 60/80. Calibration curves were made by sampling known amounts of H_2 and CO.

X-ray crystallography

Single crystal X-ray diffraction data were collected on a Synergy Custom system CCD Plate equipped with confocal monochromated Mo-Kα radiation (λ = 0.71069 Å) coated with Paratone-N (Hampton Research Corp., Aliso Viejo, CA, USA). Data was processed using CrysAlisPro system software.[37] The structure was solved by dual-space algorithm using SHELXT program[38] through the Olex2 interface.[39] All non-hydrogen atoms were refined anisotropically using a least-squares method, and hydrogen atoms were fixed at calculated positions and refined using a riding model. SHELXL−2014/7 was used for structure refinement.[40] Full-matrix least-squares refinements on F^2 based on unique reflections with unweighted and weighted agreement factors of $R = \Sigma||F_o| - |F_c||/\Sigma|F_o|$ ($I > 2.00\ \sigma(I)$) and $wR = [\Sigma w(F_o^2 - F_c^2)^2/\Sigma w(F_o^2)^2]^{1/2}$ were performed. Mercury 4.0.0 was used for visualization and analysis of the structure. Crystallographic data have been deposited with Cambridge Crystallographic Data Centre: Deposition numbers CCDC 2110898 for **CuTPFP**. Copies of the data can be obtained free of charge via www.ccdc.cam.ac.uk/data_request/cif.

References

[1] A. M. Appel, J. E. Bercaw, A. B. Bocarsly, H. Dobbek, D. L. DuBois, M. Dupuis, J. G. Ferry, E. Fujita, R. Hille, P. J. A. Kenis, C. A. Kerfeld, R. H. Morris, C. H. F. Peden, A. R. Portis, S. W. Ragsdale, T. B. Rauchfuss, J. N. H. Reek, L. C. Seefeldt, R. K. Thauer, G. L. Waldrop, *Chem*. *Rev*. **2013**, *113*, 6621.

[2] R. Francke, B. Schille, M. Roemelt, *Chem*. *Rev*. **2018**, *118*, 4631.

[3] E. Boutin, L. Merakeb, B. Ma, B. Boudy, M. Wang, J. Bonin, E. Anxolabéhère-Mallart, M. Robert, *Chem*. *Soc*. *Rev*. **2020**, *49*, 5772.

[4] C. Costentin, S. Drouet, G. Passard, M. Robert, J. M. Savéant, *J. Am*. *Chem*. *Soc*. **2013**, *135*, 9023.

[5] C. Costentin, G. Passard, M. Robert, J. M. Savéant, *J. Am. Chem. Soc*. **2014**, *136*, 11821.

[6] E. M. Nichols, J. S. Derrick, S. K. Nistanaki, P. T. Smith, C. J. Chang, *Chem. Sci*. **2018**, *9*, 2952.

[7] I. Azcarate, C. Costentin, M. Robert, J. M. Savéant, *J. Am. Chem. Soc*. **2016**, *138*, 16639.

[8] E. A. Mohamed, Z. N. Zahran, Y. Naruta, *Chem. Commun*. **2015**, *51*, 16900.

[9] Y. Okabe, S. K. Lee, M. Kondo, S. Masaoka, *J. Biol. Inorg. Chem*. **2017**, *22*, 713.

[10] C. Costentin, G. Passard, M. Robert, J. M. Savéant, *Proc. Natl. Acad. Sci. U. S. A*. **2014**, *111*, 14990.

[11] S. Sinha, J. J. Warren, *Inorg. Chem*. **2018**, *57*, 12650.

[12] K. Kosugi, M. Kondo, S. Masaoka, *Angew. Chem. Int. Ed*. **2021**, *60*, 22070.

[13] W. Nie, D. E. Tarnopol, C. C. L. McCrory, *J. Am. Chem. Soc*. **2021**, *143*, 3764.

[14] C. Cometto, L. Chen, P. K. Lo, Z. Guo, K. C. Lau, E. Anxolabéhère-Mallart, C. Fave, T. C. Lau, M. Robert, *ACS Catal*. **2018**, *8*, 3411.

[15] J. S. Derrick, M. Loipersberger, R. Chatterjee, D. A. Iovan, P. T. Smith, K. Chakarawet, J. Yano, J. R. Long, M. Head-Gordon, C. J. Chang, *J. Am. Chem. Soc*. **2020**, *142*, 20489.

[16] M. D. Sampson, C. P. Kubiak, *J. Am. Chem. Soc*. **2016**, *138*, 1386.

[17] L. M. Cao, H. H. Huang, J. W. Wang, D. C. Zhong, T. B. Lu, *Green Chem*. **2018**, *20*, 798.

[18] S. K. Lee, M. Kondo, G. Nakamura, M. Okamura, S. Masaoka, *Chem. Commun*. **2018**, *54*, 6915.

[19] K. Y. Wong, W. H. Chung, C. P. Lau, *J. Electroanal. Chem*. **1998**, *453*, 161.

[20] D. S. Laitar, P. Müller, J. P. Sadighi, *J. Am. Chem. Soc*. **2005**, *127*, 17196.

[21] R. J. Haines, R. E. Wittrig, C. P. Kubiak, *Inorg. Chem*. **1994**, *33*, 4723.

[22] R. Angamuthu, P. Byers, M. Lutz, A. L. Spek, E. Bouwman, *Science* **2010**, *327*, 313.

[23] Y. Zhou, Y. Xiao, J. Zhao, *New J. Chem*. **2020**, *44*, 16062.

[24] Z. Guo, F. Yu, Y. Yang, C. F. Leung, S. M. Ng, C. C. Ko, C. Cometto, T. C. Lau, M. Robert, *ChemSusChem* **2017**, *10*, 4009.

[25] W. J. Liu, H. H. Huang, T. Ouyang, L. Jiang, D. C. Zhong, W. Zhang, T. B. Lu, *Chem. Eur. J*. **2018**, *24*, 4503.

[26] X. Chai, H. H. Huang, H. Liu, Z. Ke, W. W. Yong, M. T. Zhang, Y. S. Cheng, X. W. Wei, L. Zhang, G. Yuan, *Chem. Commun*. **2020**, *56*, 3851.

[27] Y. Hori, H. Wakebe, T. Tsukamoto, O. Koga, *Electrochim. Acta* **1994**, *39*, 1833.

[28] L. Liu, C. Zhao, Y. Li, *J. Phys. Chem. C* **2012**, *116*, 7904.

[29] H. Yang, X. W. He, F. Wang, Y. Kang, J. Zhang, *J. Mater. Chem*. **2012**, *22*, 21849.

[30] S. Nitopi, E. Bertheussen, S. B. Scott, X. Liu, A. K. Engstfeld, S. Horch, B. Seger, I. E. L. Stephens, K. Chan, C. Hahn, J. K. Norskøv, T. F. Jaramillo, I. Chorkendorff, *Chem. Rev*. **2019**, *119*, 7610.

[30] C. Costentin, S. Drouet, M. Robert, J. M. Savéant, *J. Am. Chem. Soc*. **2012**, *134*, 11235.

[31] C. Costentin, J. M. Savéant, *ChemElectroChem* **2014**, *1*, 1226.

[32] W. Zhang, W. Z. Lai, R. Cao, *Chem. Rev*. **2017**, *117*, 3717.

[33] S. L. Rebelo, A. M. N. Silva, C. J. Medforth, C. Freire, *Molecules* **2016**, *21*, 481.

[34] M. L. Pegis, J. A. S. Roberts, D. J. Wasylenko, E. A. Mader, A. M. Appel, J. M. Mayer, *Inorg. Chem*. **2015**, *54*, 11883.

[35] A. D. Alder, F. R. Long, W. Shergalis, *J. Am. Chem. Soc*. **1964**, *86*, 3145.

[36] CrysAlisPro, Oxford Diffraction Ltd., Version 1.171.39.46.

[37] G. M. Sheldrick, *Acta Cryst*. **2015**, A71, 3.

[38] O. V. Dolomanov, L. J. Bourhis, R. J. Gildea, J. A. K. Howard, H. Puschmann, *J. Appl. Crystallogr.* **2009**, *42*, 339.

[39] G. M. Sheldrick, *Acta Cryst.* **2015**, A71, 3.

Concluding Remarks

The research described in this thesis has investigated the effect of the reaction field on the electrochemical CO_2 reduction activity catalyzed by metal porphyrin complexes.

In chapter 1, I focused on the modification of the second coordination sphere of the iron porphyrin complex to control the reaction field. I have successfully synthesized and characterized a new iron porphyrin complex which bears a hydroquinone moiety at the meso position. Electrochemical analysis of the iron porphyrin complex under CO_2 indicated that the catalytic activity is improved by introducing a hydroquinone moiety. This study clarifies that modification of the secondary coordination sphere with hydroquinone is an effective strategy for improving the catalytic activity of an iron porphyrin complex for CO_2 reduction.

In chapter 2, I investigated the effect of the reaction medium on the electrochemical CO_2 reduction activity catalyzed by iron porphyrin complex. Although reaction medium is important reaction field that influences the selectivity and reactivity, so far, there has been no example that investigates the effect of the reaction medium on the electrochemical CO_2 reduction reaction in detail. In this chapter, I have shown a dramatic improvement in the electrochemical CO_2 reduction activity of iron(III) tetraphenylporphyrin complex simply by changing the reaction medium. Importantly, the use of MeCN as the solvent significantly enhanced the catalytic activity. Under the optimized conditions, iron(III) tetraphenylporphyrin complex exhibited the highest TOF (7,300,000 s^{-1}) among the current best-in-class molecular catalysts. The "quick and easy" method presented in this thesis is a new approach for improving the electrochemical CO_2 reduction activity of iron porphyrin complexes.

In chapter 3, I have shown a copper-based homogeneous catalyst that exhibits highly active electrochemical CO_2 reduction. I selected copper porphyrin complex bearing strong electron withdrawing substituent at the meso positions as a copper-based molecular catalyst that satisfied the following three elements: (i) copper porphyrin as a scaffold, (ii) introduction of strong electron-withdrawing substituents, and (iii) soluble in MeCN as a reaction medium. The complex exhibited a TOF value for CO production of 1,460,000 s^{-1} at $\eta = 0.85$ V, which is more than 1,000,000 times higher than those of other reported copper-based catalysts. Furthermore, the TOF value of the copper catalyst at a

low overpotential (1,770 s^{-1} at η = 0.17 V) was superior than those of most catalysts, demonstrating the advantages of my strategy. I believe that the present study will open a new avenue for the development of efficient copper-based homogeneous catalysts for CO_2 reduction.

Collectively, the results in this thesis have shown that the catalytic activity of electrochemical CO_2 reduction system is improved dramatically by the effect of reaction field. Modification of the second coordination sphere is an attractive way to control the reaction field because this strategy provides a virtually infinite number of molecular designs. The method to control the reaction field focusing on the reaction medium may be widely used because of its convenience. I believe that the appropriate combination of the modification of the second coordination sphere and reaction medium may provide a much more excellent electrochemical CO_2 reduction system in the future.

Acknowledgements

The studies presented in this thesis were carried out at Division of Applied Chemistry, Graduate School of Engineering, Osaka University from October 2019 to January 2022 under the supervision of Professor Shigeyuki Masaoka.

First of all, I would like to express my deepest appreciation to Professor Shigeyuki Masaoka for his helpful discussions, useful suggestions, and encouragement. Various comments based on electrochemistry and coordination chemistry were invaluable for this study. I wish to express my sincere gratitude to Associate Professor Mio Kondo for valuable suggestions, fruitful discussions and heartwarming advices. Thanks to her advice, the quality of my papers has improved dramatically. The author also expresses gratitude to Assistant Professor Yutaka Saga for his technical advice and valuable comments.

I would like to express my gratitude to Assistant Professor Yuma Morimoto, Dr. Hitoshi Izu, and Dr. Hikaru Iwami. Scientific talks with them on various occasions were very enjoyable and fruitful.

Acknowledgement is also made to current and alumni of Masaoka group, Mr. Takuya Akai, Ms. Misa Tomoda, Ms. Mei Ishihara, Mr. Soshi Kato, Ms. Mayu Fujisawa, Mr. Hayato Tatewaki, Mr. Ryo Tomiyasu, Mr. Yusuke Nakayama, Mr. Hirotaka Hamaguchi, Mr. Shinki Fujisawa, Mr. Li Shang Xing, Ms. Kanako Okuda, Ms. Hina Kashima, Mr. Toshimichi Kobayashi, Mr. Nozomi Yamaguchi, Mr. Taito Watanabe, Mr. Maho Imai, Ms. Yumi Iwamura, Ms. Yuka Kiyokawa, Mr. Takumi Matsuzaki, and Mr. Yuma Mori. The discussion with them were exciting and generated my motivation of this study. I also appreciate the secretaries, Ms. Kyoko Kawashima, and Ms. Kiyomi Lee for administration supports. My special thanks are due to Ms. Chiharu Akatsuka, Ms. Hina Kashima, and Mr. Maho Imai who advance the research with me.

I would like to acknowledge Professor Hirofumi Sato in Kyoto university for suggesting me a roadmap in the world of chemistry. I am deeply grateful to Assistant Professor Hiroshi Nakano for teaching me theoretical chemistry, which is one of my

greatest strengths. I would also like to thank members of Sato group for their discussions and friendships even after I left the group.

I would like to thank Professor Akihisa Shioi, Professor Kenichi Yoshikawa, and Associate Professor Daigo Yamamoto in Doshisha university for teaching me the joy of research. The research life under them has greatly contributed to the formation of my personality as a chemist.

I would like to thank Japan Society for the Promotion of Science (JSPS) for financial support (Fellowship for Japanese Junior Scientists).

Finally, I sincerely thank my family, Akira Kosugi, Naomi Kosugi, Hiroyasu Kosugi, Junya Kosugi, Shinya Kosugi, Yuka Kosugi, Saburo Kuga, and Miwako Kuga for their understanding, encouragement, and continuous support.

List of Publications

Chapter 1

"Synthesis and Electrocatalytic CO_2 Reduction Activity of an Iron Porphyrin Complex Bearing a Hydroquinone Moiety"

Kento Kosugi, Maho Imai, Mio Kondo, Shigeyuki Masaoka

Chem. Lett. **2022**. (DOI:10.1246/cl.210734).

Chapter 2

"Quick and Easy Method to Dramatically Improve the Electrochemical CO_2 Reduction Activity of an Iron Porphyrin Complex"

Kento Kosugi, Mio Kondo, Shigeyuki Masaoka

Angew. Chem. Int. Ed. **2021**, *60*, 22070.

Chapter 3

"Copper(II) tetrakis(pentafluorophenyl)porphyrin: Highly Active Copper-based Molecular Catalyst for Electrochemical CO_2 Reduction"

Kento Kosugi, Hina Kashima, Mio Kondo, Shigeyuki Masaoka

Chem. *Commun*. **2022**. (DOI: 10.1039/d1cc05880k).

Other Publications

[1] "Helical Micromotor Operating under Stationary DC Electrostatic Field"
Daigo Yamamoto, **Kento Kosugi**, Kazuya Hiramatsu, Wenyu Zhang, Akihisa Shioi, Kaori Kamata, Tomokazu Iyoda, Kenichi Yoshikawa, *J. Chem. Phys.* **2019**, *150*, 014901.

[2] "SCC-DFTB-PIMD Method to Evaluate a Multidimensional Quantum Free-Energy Surface for a Proton-Transfer Reaction"
Kento Kosugi, Hiroshi Nakano, Hirofumi Sato, *J. Chem. Theory Comput.* **2019**, *15*, 4965.

[3] "Modulation of Self-Assembly Enhances the Catalytic Activity of Iron Porphyrin for CO_2 Reduction"
Masahiro Tasaki, Yuki Okabe, Hikaru Iwami, Chiharu Akatsuka, **Kento Kosugi**, Kohei Negita, Sinpei Kusaka, Ryotaro Matsuda, Mio Kondo, Shigeyuki Masaoka, *Small*, **2021**, 2006150.